

Evolution of Karst Aquifers in Natural and Man Made Environments: A Modeling Approach

Douchko Romanov

Universität Bremen 2003

Evolution of Karst Aquifers in Natural and Man Made Environments: A modeling approach

**Vom Fachbereich für Physik und Elektrotechnik
der Univerität Bremen**

**zur Erlangung des akademischen Grades eines
Doktor der Naturwissenschaften (Dr. rer. nat.)
genehmigte Dissertation**

**von
Dipl. Phys. Douchko Romanov
aus Sofia, Bulgarien**

**1. Gutachter:
2. Gutachter:**

**Prof. Dr. W. Dreybrodt
Dr. R. Liedl**

**Eingereicht am:
Tag des Promotionskolloquiums:**

**19. 03. 2003
23. 04. 2003**

Acknowledgments

To go and start to work in a foreign country is never easy. Three years ago I had the chance to join the workgroup of Prof. Dreybrodt. It is also not easy to express feelings. Therefore I will make it short. Thank you:

To Prof. Wolfgang Dreybrodt – he was always at the right place at the right time.

To Dr. Franci Gabrovsek. – he was the peace of BALKAN in the FAR NORTH of Bremen.

To Katrin Vosbeck – a real german friend.

To Dr. Alexander Jeschke – always ready for loooooong and interesting discussions.

I would also like to thank to the Tuebingen group. The seminars, perfectly organized by Dr. Liedl were a place for sharing the newest ideas in the area of karst modeling.

I am really grateful to “Stiftung Constantia v. 1823, Bremen” for their financial support.

Contents

Introduction	1
Goal and structure of this thesis	4
1. Basic principles of 2D modeling of karst aquifers	8
1.1. Single fracture	8
1.1.1. Hydrological part	10
1.1.2. Chemical part	10
1.1.3. Evolution of a single fracture	12
1.2. 2D networks	14
2. Influence of exchange flow on the early evolution of karst aquifers	17
2.1. Interaction of fracture and conduit flow in the early evolution of karst aquifers	18
2.1.1. Basic settings	18
2.1.2. Numerical results	21
2.1.2.1. Influence of the exchange flow on the breakthrough times	21
2.1.2.2. Evolution of the fracture aperture widths (standard scenarios A and B)	23
2.1.2.3. Numerical results for the central channel (standard scenario A)	32
2.1.2.4. Numerical results for extended scenarios	37
2.1.3. Conclusion	41
2.2. The influence of the exchange flow on the evolution of a single conduit	43
2.2.1. Basic setup	43
2.2.2. Numerical results	50
2.2.3. Discussion	57
2.2.4. Analytical approximation	58
2.2.5. Conclusion	60
3. Karstification below dam sites	61
3.1. Basic settings	63
3.1.1. Geological settings	63
3.1.2. Modeling domain	64
3.1.3. Numerical results for standard scenarios	67
3.1.3.1. Standard scenario A – uniform case	68
3.1.3.2. Standard scenario B – uniform case	73
3.1.3.3. Standard scenario A – statistical case	75

3.1.3.4. Standard scenario B – statistical case	78
3.1.4. Evolution of the leakage rates for the standard scenarios	80
3.1.5. Standard scenario A – statistical case – gypsum	82
3.1.6. Influence on the basic hydrological and geochemical parameters on the breakthrough time	85
3.1.7. Examples of different geological settings	88
3.1.8. Effect of mixing corrosion on the evolution of a dam site	91
3.1.9. Conclusion	92
3.2. Modeling of a catastrophic failure of the San Juan reservoir (NE Spain).	94
3.2.1. Modeling domain	94
3.2.2. Numerical results	95
3.2.3. Conclusion	101
4. The influence of the chemical boundary conditions on the evolution of karst aquifers	102
4.1. Basic settings	102
4.2. Numerical results	106
4.2.1. Evolution dominated by BT	106
4.2.2. Evolution dominated by MC	108
4.2.3. Intermediate cases (both MC and BT active)	114
4.2.4. Discussion	120
4.2.5. Conclusion	124
5. Conclusion	125
Bibliography	129

Introduction

Sedimentary rocks cover approximately 75 % of the continents (Hamblin, 1992). Their formation involves weathering of preexisting rock, transportation of the material away from the original site, and deposition of the eroded material. Weathering is the mechanical and chemical breakdown of rocks and minerals. Based on the way they are formed, the sedimentary rocks can be divided into the following categories:

- a) Clastic sedimentary rocks – broken rock fragments that have been lithified. They are subdivided according to the grain size of the component materials. From the largest grain size to the smallest, the types of the clastic rocks are: conglomerate, sandstone, siltstone, and shale;
- b) Chemical and organic sedimentary rocks – they are formed by chemical precipitation or by biological processes. The most important are: limestone, dolostone, rock salt, and gypsum.

This thesis will deal mainly with limestone, but in some cases also with gypsum ($\text{CaSO}_4 \cdot 2\text{H}_2\text{O}$).

Limestone originates by both chemical and organic processes. It is composed principally of calcium carbonate (CaCO_3). The major types are: skeletal limestone, oolitic limestone, and microcrystalline limestone. Limestones have great variety of rock textures. The limestone deposits can be several hundreds of meters thick and extend over thousands of square kilometers.

An important property of the limestone rock is, that it is dissolved by water containing CO_2 .

The unique landscape formed by the chemical action of water on these rocks is called **karst**. The origin of the term is related to the region Kras in Slovenia. 10% to 20% of the Earth's land surface is covered by karst (Ford and Williams, 1989). The evolution of the karst terrains is governed by many factors. The most important are:

- a) The climate of the region - determines the amount of water entering the karst system. It also determines the type of the vegetation and the soil cover in the region, which is related to the amount of CO_2 contained by the water. Swinnerton (1932) was the first who stressed the importance of the soil CO_2 for the karst evolution.
- b) The geological settings;
- c) The location and the geometry of the inflow and the outflow areas;
- d) The type of the soluble rock;

- e) The distribution of the primary fractures in the rock.

Karst has been subject of extensive research since centuries. The articles of Shaw (2000), Lowe (2000) and White (2000) are interesting reviews about the development of the speleogenetic studies from ancient time to the present days. People are interested in the karst evolution not only because of the beauty of the karst landforms, but also because of their practical importance. Karst aquifers (rock bodies sufficiently permeable to transmit groundwater (Bear and Veruijt, 1987)) are the main source of drinking water for about 25% of the world population (Ford and Williams, 1989).

Sinkholes, sinking streams, closed depressions, and caves characterize the topography of the karst terrains. All these different landforms have a common element. It is the well-developed subsurface drainage system. Initially, when the hydraulic conductivity of the rock is low, most of the water is flowing on its surface. Only a relatively small amount is entering the primary fractures of the soluble rock. As already discussed CO_2 containing water is an aggressive solution and is capable to dissolve a certain amount of the rock. If there is no way for the water to leave the aquifer, it becomes saturated and is not able to change the primary conduits further. Therefore a necessary condition for the initiating of karstification is the existence of places where the water can leave the block and allow further inflow of aggressive solution. The flow through the initial fractures is laminar, because their aperture widths are in the range of several 100 μm . Some of the fissures widen faster than others. Therefore the flow through them increases and consequently the rate of their widening is increased also. This positive feedback loop is the reason for the development of secondary porosity and consequently for the development of a complex, extremely heterogeneous aquifer. Flow through some of the widened fractures finally becomes turbulent. The hydraulic conductivity of the karst aquifer is increased by orders of magnitude. Most of the remaining initially small fissures are also widened. Therefore the storage capacity of the aquifer is increased. At the same time some surface karst landforms develop. The positions of the sinkholes for example are related to the evolution of the subsurface drainage.

Because of the increased permeability, most of the water on the surface is entering the drainage system after very short travel distances. It reappears in karst springs at the base level of the aquifer. Consequently most of the initially active surface fluvial systems are no longer present in the later phases of the karst evolution. But a complicated fluvial system, recharged from the karst springs, is created at the base level.

This is only an example of a simplified scenario for the evolution of the secondary porosity, where all of the pores and fractures are filled with water (confined aquifer).

But another scenario is also possible. Together with the increasing permeability, the level of the groundwater table is lowered. It continues to drop until base level is reached. The dissolution rates are maximal at the water table and a complex system of channels starts to develop there. This zone is moving downwards in the direction of the base level.

We can also assume that the soluble rock is not initially homogeneous, or that some of the primary fractures are blocked by insoluble material. Another possible complication comes from the chemical composition of the inflowing water. These simple examples show how sensitive the evolution is to changes in initial or the boundary conditions.

There are several ways to study the karstification process. The most natural one is to observe the present state of the karst aquifer and relate it to the local climate and geological settings and their changes in the past (descriptive approach). Then, this knowledge can be applied to other regions with similar evolution of the boundary conditions. The first step for this type of study is to try to describe the differences between the various karst landforms. There are several attempts for a classification (Cvijic, 1924, 1926), (Milanovic, 1981). The descriptive approach requires an enormous number of field observations and a detailed knowledge of the geological settings of the studied region. The process of collecting this information is long and sometimes the results can be related only to a small number of karst aquifers.

Another option is the analytical approach. It is based on the knowledge about the basic chemical and physical mechanisms governing the evolution. Thrailkill (1968) studied the flow patterns in pipe networks, simulating by this way the laminar and the turbulent flow in karst aquifers. At the same time he investigated the chemical evolution of the water percolating through the rock in its way to the water table. He tried to find reasons for the renewed undersaturation of this water, deep inside the aquifer. One possible reason is the effect of Mixing Corrosion, proposed by Laptev (1939) and Bögli (1964, 1980).

Nowadays, we have the basic knowledge about the properties of karst aquifers, about the hydrodynamics of the flow through it, and about the dissolution kinetics of the soluble rocks. Together with the computational power, this enables us to build numerical models of karst aquifers and study them. Dreybrodt (1988, 1990, 1996) and Palmer (1988, 1991) present the first numerical models of karst evolution. They are constructed on the basic principles of groundwater chemistry and hydrology, and study the evolution of an isolated one-dimensional conduit under various boundary conditions. By this way, they describe the evolution of the basic element, from which more complex models can be investigated, and they explain the timescales for karstification.

Using the information about the evolution of the single fracture, we are able to build and understand more complex two-dimensional models. Lauritzen (1992), Groves and Howard (1994), and Howard and Groves (1995) presented models for the evolution of two dimensional networks. Siemers and Dreybrodt (1998), Siemers (1998), and Dreybrodt and Siemers (2000) present the evolution of two dimensional percolation networks under various lithological and hydraulic conditions. They extended their studies for cases of practical interest, namely the karstification in the vicinity of large hydraulic structures.

Clemens et al (1997a; 1997b; 1996), and Bauer (2002) present a double permeability model. They couple the large conduit flow with the flow in the surrounding continuum of narrow fissures and calculate the evolution of the conduits. Kaufmann and Brown (1999, 2000) report a similar approach. Their model, however, incorporates prominent conduits directly into the continuum.

Gabrovsek (2000), Gabrovsek and Dreybrodt (2000a, 2000b) study the evolution of a single fracture and two dimensional percolation networks under various chemical and hydrological boundary conditions. Together with the numerical results, several analytical estimations for the breakthrough time are presented. Gabrovsek and Dreybrodt (2001) present also a model for the evolution of an unconfined aquifer.

Any of these different modeling approaches has its advantages and disadvantages. An important result is that all of them give similar results for basic scenarios, specially designed for comparison.

Goal and structure of this thesis

The topic of the present work is the evolution of the subsurface secondary porosity in the karst aquifers. Most of the early theories about this evolution were rather conflicting, because they were valid for a specific location. Three hypotheses were accepted between 1900 and 1950 (Ford and Williams, 1989).

- a) Vadose hypotheses – large cave conduits are excavated by open channel streams in the vadose zone;
- b) Deep phreatic hypotheses – caves develop deep below the water table;
- c) Water table hypotheses (Swinnerton, 1932; Rhoades and Sinacori, 1941) – caves are created at the water table, because most of the water is flowing through this region.

Each of these hypotheses was partially correct for specific cases, but none of them was able to explain the general case. Ford and Ewers (1978) combine them and propose a common genetic theory.

We will not discuss the consequences of the cave channel evolution to the surface. Our goal is to extend the two dimensional percolation network models, to a two dimensional network with a statistical distribution of the fracture initial aperture width. This enables us to fully study the effect of the flow exchanged between the large conduits and the fine fractures on the evolution. We will study the reaction of the model aquifers to the changes of various hydrological and chemical boundary conditions.

This thesis has four chapters. The first one gives a brief description of the basic physical and chemical laws implemented in the model. We also provide references to literature sources for more detailed discussions.

The topic of the second chapter is the influence of the flow exchanged between the hydraulic systems of the large conduits and the fine fractures, on the evolution of the aquifer (exchange flow). A systematic study for a wide range of hydrological boundary conditions is presented.

Furthermore we attempt to generalize the effect of the exchange flow for the case of a simple system of three single fractures.

The results of the second chapter are applied to a specific case of large hydraulic structures. This is the topic of the third chapter. It presents the evolution of a karst aquifer under man made hydrological and chemical boundary conditions. The effect of different dam sites on this evolution is systematically studied. A comprehensive sensitivity analysis is presented in order to give an idea of the possible ways to increase the safety of the structures.

The topic of the fourth chapter is the evolution of a simple karst aquifer under various chemical boundary conditions. The effect of Mixing Corrosion, and the Ca concentration of the inflowing water, is studied systematically.

These results are discussed from the point of view of the mechanisms and processes active in the karst aquifer during its evolution. For the case of the dam sites we only put attention on the risks connected with these structures. It is clear that because of the complexity of the realistic environments, our results cannot be applied directly to real karst aquifers. But the studies presented here are systematical. Therefore, the results can be used as a reference point and a building block of a description of real karst systems.

There are some dangers when numerical models are used to describe certain scenarios. The problem is that it is relatively easy to select certain boundary conditions, apply them to the

modeled aquifer, and then simply press “Enter”, and run the program. In any case there will be some results. One of the most difficult parts of the numerical modeling is to understand the obtained results. The more complex the models are the more difficult is the interpretation. Therefore one has to be careful and cautious to the obtained results. Also the selection of the initial and boundary conditions, their understanding, and the understanding of their relation to the obtained results is a crucial part of the numerical modeling. Before the beginning of the “serious” part of this work, here is an example about the discussed problems for the interpretation of the numerical models.

It is a small story from a classical book called “The Hitchhikers Guide to the Galaxy” by Douglas Adams. The story took place “many, many years ago”, of course. It is about a “race of hyperintelligent pan-dimensional beings”. They were tired always to search for an answer to the questions about the meaning of “Life, the Universe, and Everything” and “decided to sit down and solve their problems once and for all”. They built a super computer called - Deep Thought. Its purpose was to calculate the Answer. After 7.5 million years of calculations the computer was ready and here is what happened on “The Day of the Answer”.

"Good morning," said Deep Thought at last.

"Er ... Good morning, O Deep Thought," said Loonquawl nervously,

"do you have ... er, that is ..."

"An answer for you?" interrupted Deep Thought majestically. "Yes. I have."

The two men shivered with expectancy. Their waiting had not been in vain.

"There really is one?" breathed Phouchg.

"There really is one," confirmed Deep Thought.

"To Everything? To the great Question of Life, the Universe and Everything?"

"Yes."

Both of the men had been trained for this moment, their lives had been a preparation for it, they had been selected at birth as those who would witness the answer, but even so they found themselves gasping and squirming like excited children.

"And you're ready to give it to us?" urged Loonquawl.

"I am."

"Now?"

"Now," said Deep Thought.

They both licked their dry lips.

"Though I don't think," added Deep Thought, "that you're going to like it."

"Doesn't matter!" said Phouchg. "We must know it! Now!"

"Now?" inquired Deep Thought.

"Yes! Now ..."

"Alright," said the computer and settled into silence again. The two men fidgeted. The tension was unbearable.

"You're really not going to like it," observed Deep Thought.

"Tell us!"

"Alright," said Deep Thought. "The Answer to the Great Question..."

"Yes ...!"

"Of Life, the Universe and Everything ..." said Deep Thought.

"Yes ...!"

"Is ..." said Deep Thought, and paused.

"Yes ...!"

"Is ..."

"Yes ...!!!...?"

"Forty-two," said Deep Thought, with infinite majesty and calm.

.....

"Forty-two!" yelled Loonquawl. "Is that all you've got to show for seven and a half million years' work?"

"I checked it very thoroughly," said the computer, "and that quite definitely is the answer. I think the problem, to be quite honest with you, is that you've never actually known what the question is."

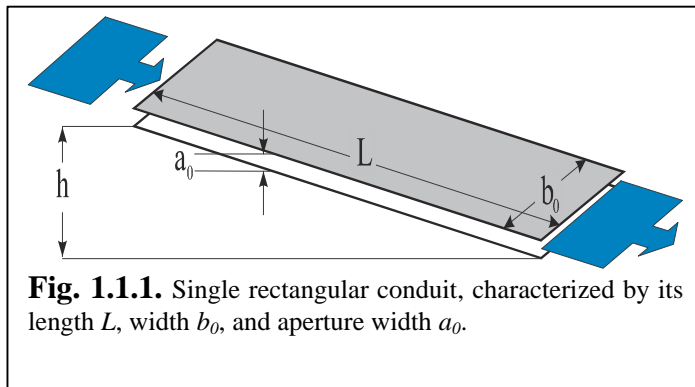
I hope to ask the correct questions for the answers discussed through the rest of this work.

1. Basic principles of 2D modeling of karst aquifers

We present only the basic relations used to create our models. Details are reported in the literature (Dreybrodt, 1988; Dreybrodt, 1996; Siemers and Dreybrodt, 1998; Gabrovsek, 2000).

1.1 Single fracture

The basic element of our models is the single conduit. We use this block to create complex systems and model the processes, which govern the evolution of natural karst aquifers.



A single conduit is presented in Fig. 1.1.1. In this case it has a rectangular shape, but it can be a cylindrical tube or can have any kind of characteristic geometry. The aperture width a_0 , the width b_0 , and the length L , characterize the rectangular fractures.

We are able to model also the evolution of cylindrical conduits (tubes), but for the rest of this work we will deal only with rectangular fractures.

To model the evolution of the fracture in time, we need to know:

- a) The hydrological laws – governing the flow through the fracture;
- b) The chemical laws – governing the change in the profile, because of dissolution, along the fracture.

1.1.1. Hydrological part

Initially when the fracture aperture widths a_0 are small, the flow through the fissures is laminar. In this case the flow rate Q [cm^3/s] is related to the hydraulic head difference h [cm] by:

$$Q = \frac{h}{R^{lam}} \quad (1.1),$$

where R is the hydraulic resistance [$cm^{-2}s$] given by the Hagen-Poiseuille's law (Beek and Muttzall, 1975).

$$R^{lam} = \frac{12\mathbf{h}}{\mathbf{r}g} \cdot \frac{L}{a_0^3 b_0 \cdot M} \quad (1.2),$$

where a_0 [cm] is the aperture width, b_0 [cm] is the width, and L [cm] is the length of the fracture, \mathbf{h} [$g \cdot cm^{-1} \cdot s^{-1}$] is the dynamic viscosity of water, \mathbf{r} [$g \cdot cm^{-3}$] its density, g [$cm \cdot s^{-2}$] is the Earth's acceleration. M is a geometrical factor, which depends on the ratio a_0/b_0 . M is:

$M = 0.6 - 0.3a_0 / b_0$ - ellipsoidal shape and

$M = 1 - 0.6a_0 / b_0$ - rectangular shape.

For wide fractures ($a_0 \ll b_0$), $M \rightarrow 1$.

Eq. 1.2 gives the hydraulic resistance in the initial moment, when the walls of the fracture are still parallel (see Fig. 1.1.1). But because of the dissolution active along the fracture, its profile changes and obtains a funnel like shape. The hydraulic resistance is given by integration of small segments of the conduit.

If flow is turbulent, for a fracture with parallel walls we use the Darcy-Weissbach equation (Dreybrodt, 1988; Clemens et al, 1996):

$$Q = \sqrt{\frac{2gA^2 d}{f}} \cdot \sqrt{\frac{h}{L}} \cdot \frac{h}{|h|} = \frac{h}{R^{turb}} \quad (1.3),$$

where A [cm^2] is the cross-sectional area, d [cm] is the wetted hydraulic diameter ($d = \frac{2ab}{a+b}$, for $b \gg a$, $d=2a$, a [cm] is the aperture width, and b [cm] is the width) of the

conduit, and f is the friction factor given by the Colebrook-White equation:

$$\frac{1}{\sqrt{f}} = 1.14 - 2 \log_{10} \left[\frac{r}{3.71 \cdot d} + \frac{2.51 \cdot \mathbf{h}}{Re \sqrt{f}} \right] \quad (1.4).$$

Here r [cm] is the roughness of the wall, and Re is the Reynolds number:

$$Re = \frac{a \cdot v \cdot \mathbf{r}}{\mathbf{h}} = \frac{Q\mathbf{r}}{\mathbf{h}b} \quad (1.5),$$

where v is the flow velocity in the conduit.

For smooth fractures flow becomes turbulent for $Re > 2000$. In all calculations in this work we use $r=0$.

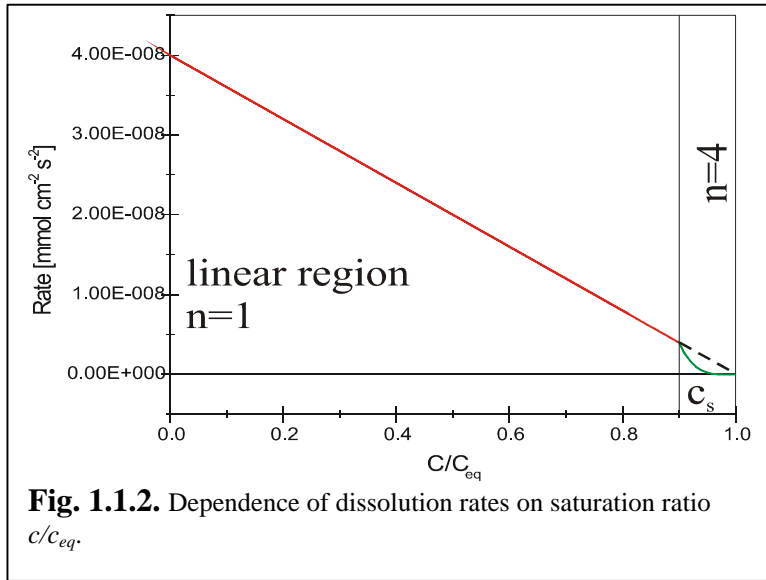
1.1.2. Chemical part

After the flow through the fracture is known we calculate the dissolutional widening along it. The dissolution rates $F[\text{mol}\cdot\text{cm}^{-2}\cdot\text{s}^{-1}]$ of limestone have been intensively investigated. For the system closed with respect to CO_2 they are described (Eisenlohr et al., 1999) by the rate law:

$$F_1 = k_1 \left(1 - \frac{c}{c_{eq}} \right), c \leq c_s$$

$$F_n = k_n \left(1 - \frac{c}{c_{eq}} \right)^n, c \geq c_s$$
(1.6),

where c is the actual calcium concentration, $c_{eq} [\text{mol}\cdot\text{cm}^{-3}]$ is the equilibrium concentration



with respect to calcite, $c_s [\text{mol}\cdot\text{cm}^{-3}]$ is the concentration where the dissolution rates switch from a linear rate law to a non linear one with order n . The values of c_s , k_1 and n are characteristic for the mineral. Fig. 1.1.2 depicts the dependence of dissolution rates on the saturation ratio c/c_{eq} . Gypsum follows similar rate laws

(Jeschke et al, 2001).

For limestone, k_1 is controlled by surface reactions, conversion of CO_2 , and diffusive mass transport. Therefore this value depends on the aperture width of the fracture, and on the conditions of flow. In laminar flow the ratio $V/A = d [\text{cm}]$ (V is the volume of water, dissolving limestone from surface A) controls the dissolution rates. The value of k_1 used in this study is $k_1 = 4 \cdot 10^{-11} [\text{mol}\cdot\text{cm}^{-2}\cdot\text{s}^{-1}]$. It is constant for aperture widths in the range $5 \cdot 10^{-3}$ cm to 0.1 cm. With the increase of the aperture width of the fracture, the influence of the diffusive mass transport becomes rate limiting. In this case a modified value k_D , of k_1 under laminar flow conditions, is used:

$$k_D = k_1 \left(1 + \frac{k_1 \cdot a}{3 \cdot D \cdot c_{eq}} \right)^{-1}$$
(1.7),

where $D [cm^2s^{-1}]$ is the constant of diffusion for Ca^{2+} (in water $\approx 10^{-5} cm^2s^{-1}$). Details are given by Buhmann and Dreybrodt (1985a, b) and Dreybrodt (1988).

If flow is turbulent the bulk of the solution is mixed by eddies. The completely mixed bulk is separated from the surface by a diffusion boundary layer (DBL). The thickness of this layer is e and depends on the hydrodynamic conditions of flow. Mass transport from the mineral's surface into the bulk and vice versa is affected by molecular diffusion through this layer:

$$e = \frac{a}{Sh} \quad (1.8).$$

Sh is the dimensionless Sherwood number given by (Incropera and Dewitt, 1996):

$$Sh = \frac{(f/8) \cdot (Re - 1000) \cdot Sc}{1 + 12.7 \sqrt{\frac{f}{8}} \left(Sc^{\frac{2}{3}} - 1 \right)} \quad (1.9).$$

Sc is the Schmidt number:

$$Sc = \frac{h}{rD} \quad (1.10).$$

For water $Sc \gg 1000$.

The dependence of the dissolution rates F for limestone on the thickness of e has been investigated by Dreybrodt and Buhmann (1991) (theoretically) and by Liu and Dreybrodt (1997) (experimentally). For $e > 0.01 cm$ the rates become independent on e with $k_l = 4 \times 10^{-11} mol \cdot cm^{-2} \cdot s^{-1}$. The thickness of the boundary layer in our calculations is in the order of several tenth of a mm. Therefore, we use the value of $k_l = 4 \times 10^{-11} mol \cdot cm^{-2} \cdot s^{-1}$ for the rate constant of the linear rate law in the case of turbulent flow.

In the early stages, when the flow is laminar, after short distances away from the entrance the solution comes close to equilibrium. Natural calcite carbonates exhibit inhibition of dissolution rates due to impurities in the limestone (Svensson and Dreybrodt, 1992; Eisenlohr et al, 1997; Dreybrodt and Eisenlohr, 2000). Then the dissolution rates drop by orders of magnitude and follow a non-linear rate law (see Eq. 1.6). The value of c_s is between $0.7 \cdot c_{eq}$ and $0.9 \cdot c_{eq}$ for different limestone species. We use the value $c_s = 0.9 \cdot c_{eq}$ for our calculations. n also varies and has typical values between 3 and 6. The value used for our calculations is 4. The value of k_n (see Eq. 1.6) used here is $4 \cdot 10^{-8} mol \cdot cm^{-2} \cdot s^{-1}$.

If flow is laminar then the rates calculated by Eq 1.6 are compared with the diffusional rates:

$$F_D = \frac{D}{a} c_{eq} \left(1 - \frac{c}{c_{eq}} \right) \quad (1.11),$$

and the smaller ones are used.

An important result (Jeschke et al. 2001) is that the dissolution rates for gypsum follow similar rate laws as for the limestone (see Eq. 1.6). This enables us to model gypsum karst in a similar way as limestone karst. The rate laws for gypsum are:

$$F_1 = k_{gyp} \left(1 - \frac{c}{c_{eq}} \right) \quad c \leq c_s \quad (1.12),$$

$$F_n = k_n \left(1 - \frac{c}{c_{eq}} \right)^n, \quad c \geq c_s$$

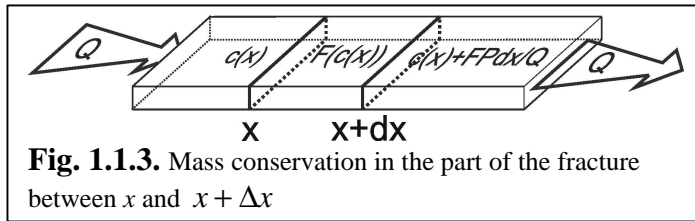
where k_{gyp} is:

$$k_{gyp} = \frac{k_1 \frac{D \cdot c_{eq}}{e}}{k_1 + \frac{D \cdot c_{eq}}{e}} \quad (1.13).$$

Details on the dissolution rates of gypsum are given by Jeschke et al. (2001). The values of the constants used for gypsum are as follows:

$$k_n = 3 \times 10^{-3} \text{ mol} \cdot \text{cm}^{-2} \cdot \text{s}^{-1}; \quad n = 4.5; \quad c_{eq} = 15.4 \times 10^{-6} \text{ mol} \cdot \text{cm}^{-3}; \quad c_s = 0.95 \cdot c_{eq}.$$

1.1.3. Evolution of a single fracture



To calculate the widening rate $F(x)$ we need to know the concentration $c(x)$ along the fracture. Fig. 1.1.3 represents part of a fracture between x and $x + \Delta x$, where x is the

distance from the entrance. We use the mass balance and obtain the following equation:

$$F(c(x))P(x)dx = v(x) \cdot A(x)dc = Q \cdot dc \quad (1.14),$$

where $A(x)$ is the cross-sectional area at x , $P(x)$ the perimeter there, and v is the velocity of the fluid. The solution of this equation for plane parallel walls is given by (Dreybrodt, 1996; Dreybrodt and Gabrovsek, 2000; Gabrovsek, 2000):

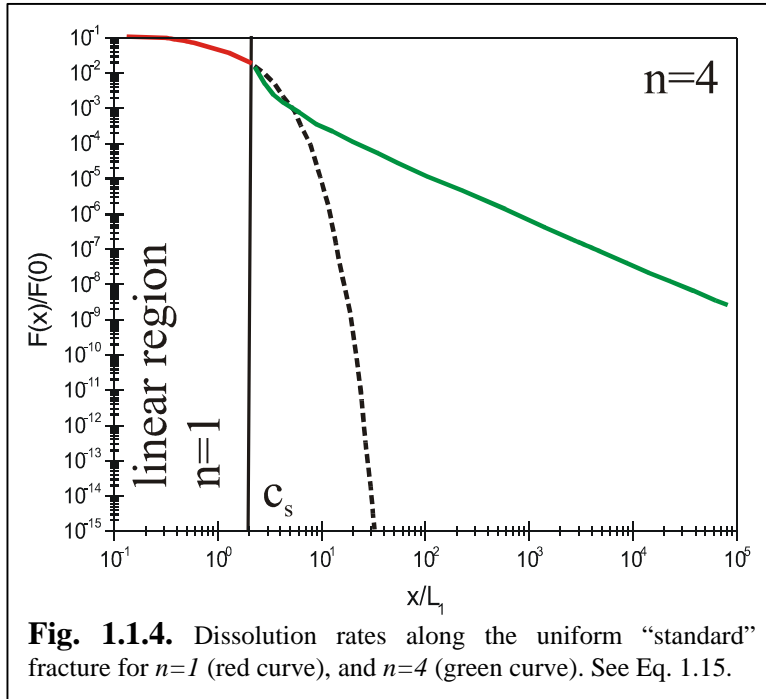
$$F(x) = \begin{cases} F_1(x) = k_1 \left(1 - \frac{c_{in}}{c_{eq}} \right) \exp\left(-\frac{x}{I_1} \right); & x < x_s \\ F_n(x) = k_n \left(1 - \frac{c_s}{c_{eq}} \right)^n \left(1 + \frac{x - x_s}{I_n} \right)^{\frac{n}{1-n}}; & x \geq x_s \end{cases} \quad (1.15),$$

where c_{in} is the concentration at the input of the fracture and:

$$I_1 = \frac{Q \cdot c_{eq}}{P \cdot k_1}$$

$$I_n = \frac{Q \cdot c_{eq} \cdot \left(1 - \frac{c_s}{c_{eq}}\right)^{1-n}}{P \cdot k_n \cdot (n-1)} \quad (1.16),$$

P is the perimeter, and x_s is the position of the switch between the linear and the non-linear rate law.



law. Fig. 1.1.4 depicts the dependence of the dissolution rate on the position along the fracture, for the linear and the non-linear rate law. One can clearly see the importance of the non-linear part for the karstification. If the rates are fully linear then they decrease from the entrance exponentially. By this way the exit of the fracture remains practically unaffected. On the other hand,

because of the non-linear rate law, dissolution is active along the whole length of the fracture. By this way the exit part is widened, and this increases the flow through. Consequently the dissolution rates are increased, the exit is widened faster, and the flow is increased faster in time. This positive feedback loop leads to the breakthrough event. The flow increases by several orders of magnitude at this moment, and the concentration at the exit becomes practically equal to c_{in} . After the breakthrough the fracture continues to widen evenly along its entire length.

It is not possible to give an analytical expression for the evolution of the fracture width with time. But if we assume that the walls of the fracture remain parallel during the entire evolution, a reasonable approximation by an analytical solution can be obtained. In other words this means to assume that the dissolution rates remain constant along the entire length of the channel. The rate at the exit $F(L,t)$ is used for this approximation. In this case the widening is even along the conduit and is given by the equation:

$$\frac{da}{dt} = 2g \cdot F(L,t) \quad (1.17),$$

where

$$F(L,t) = k_n \left(1 - \frac{c_s}{c_{eq}} \right)^n \left\{ \frac{L \cdot a_0^3}{I_{n,t=0} \cdot a^3(t)} + 1 \right\}^{\frac{n}{1-n}} \quad (1.18).$$

γ converts the dissolution rates from $\text{mol} \cdot \text{cm}^{-2} \cdot \text{s}^{-1}$ to retreat of bedrock in $\text{cm} \cdot \text{year}^{-1}$. γ is $1.17 \cdot 10^9$ for limestone, and $1.72 \cdot 10^9$ for gypsum, $a(t)$ is the aperture width at $x=L$.

Eq. 1.17 can be integrated if we assume that the inflowing solution has concentration below c_s . In this case the 1 in the second term of Eq. 1.18 can be neglected and the result is (Gabrovsek, 2000):

$$a(t) = a_0 \left(1 - \frac{t}{T_B} \right)^{\frac{1-n}{2n+1}} \quad (1.19).$$

The breakthrough time T_B is:

$$T_B = \frac{1}{2g} \cdot \frac{n-1}{2n+1} \cdot \frac{a_0}{F(L,0)} \quad (1.20).$$

If we insert Eq. 1.18, we obtain an upper limit of the breakthrough time T_B , and also its dependence on the basic parameters determining karstification (Dreybrodt and Gabrovsek, 2000; Gabrovsek, 2000):

$$T_B = \frac{1}{2g} \cdot \frac{n-1}{2n+1} \cdot \left(\frac{1}{a_0} \right)^{\frac{2n+1}{n-1}} \left(\frac{24hL^2(n-1)}{rghc_{eq}} \right)^{\frac{n}{n-1}} (k_n)^{\frac{1}{n-1}} \quad (1.21).$$

See Gabrovsek (2000) for more details on the evolution of a single fracture under various boundary conditions.

To obtain exact results one must take into account that the shape of the fractures shows a funnel like profile. Details on this numerical procedure are given by Gabrovsek (2000), Dreybrodt (1996).

Our next step is to use the single conduit and to build a 2D network.

1.2. 2D networks

We will model only confined karst aquifers. Therefore all fractures comprising the 2D network are assumed to be full of water during the entire evolution. Fig. 1.2.1 depicts an example of a rectangular two-dimensional fracture network. We are able to apply different hydrological and chemical parameters to every single fracture. Varying the spacing between the fractures and their initial aperture widths we are able to model different hydraulic conductivities in the domain. The relation between the hydraulic conductivity and the parameters of the fractures is (Lee and Farmer, 1993):

$$K = \frac{rg}{12h} \frac{a_0^3}{s} \quad (1.22),$$

where s is the spacing between the fissures.

As a first step, we must calculate the flow through every fracture. The mass conservation at each node i yields the equation:

$$\sum_j Q_{ij} + Q_i = 0 \quad (1.23).$$

Q_{ij} is the flow between the node j connected with node i , and Q_i is the direct supply of water into node i .

In this case Eq. 1.1 becomes:

$$Q_{ij} = \frac{h_i - h_j}{R_{ij}^{lam}} \quad (1.24),$$

for laminar flow. Here h_i and h_j are the values of the pressure head at nodes i and j correspondingly. Note that the sign of $h_i - h_j$ gives the direction of the flow.

For the case of turbulent flow, Eq. 1.3 becomes:

$$Q_{ij} = \sqrt{\frac{2gA_{ij}^2 d_{ij}}{f_{ij}}} \cdot \sqrt{\frac{h_i - h_j}{L_{ij}}} \cdot \frac{h_i - h_j}{|h_i - h_j|} = \frac{h_i - h_j}{R_{ij}^{turb}} \quad (1.25).$$

For sufficiently short segments the aperture widths profile can be approximated by plane parallel walls. Eq. 1.23, together with Eq. 1.24, or Eq. 1.25. gives a set for each node of the network. In the case of laminar flow the equations are linear, and the system is solved by a numerical method. In our case we use the preconditioned CG iteration method (Press et al., 1992, Stewart and Leyk, 1994).

The equations of the system are nonlinear in the case of turbulent flow. Then we use the Newton-Raphson iterative scheme. The initial guess for the solution is obtained either from assumption of laminar flow, or from the previous time step.

After solving the system, we know the flow conditions through every fracture of the network.

The next step is to find the dissolutional widening along each fracture.

- a) We start with the fractures connected to the nodes on the inflow boundary. All parameters at these nodes are determined by the boundary conditions;
- b) We calculate the new profile of these fractures and the concentration of the water at their output nodes;

- c) A complete mixing of the solutions inflowing to the nodes is assumed. Siemers and Dreybrodt (1998), and Siemers (1998) discuss the dependence of the network evolution on the mixing model. The concentration of the solution at each node i is:

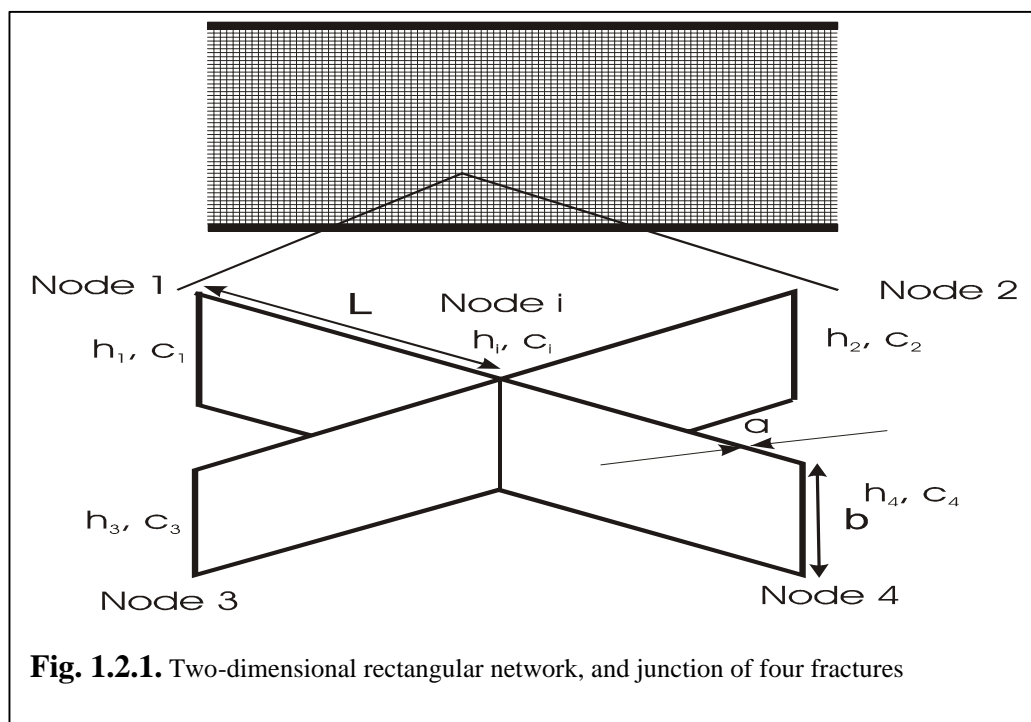
$$c_i = \frac{\sum_j Q_j c_j^{exit}}{\sum_j Q_j},$$

Where Q_j is the flow through the fracture carrying the water to the node i , and c_j^{exit} is their exit concentration.

- d) We select the nodes where the concentration is known and calculate the profiles of the fractures draining water from them;
 e) This procedure is repeated until the profiles of all conduits are known;
 f) We calculate the new head distribution according to the new fracture resistances;
 g) Calculate the new flow rates through every conduit of the network;
 h) Repeat steps a) – g) until some exit condition is fulfilled.

This was a short description of the basic laws and algorithms we use to build the 2D models.

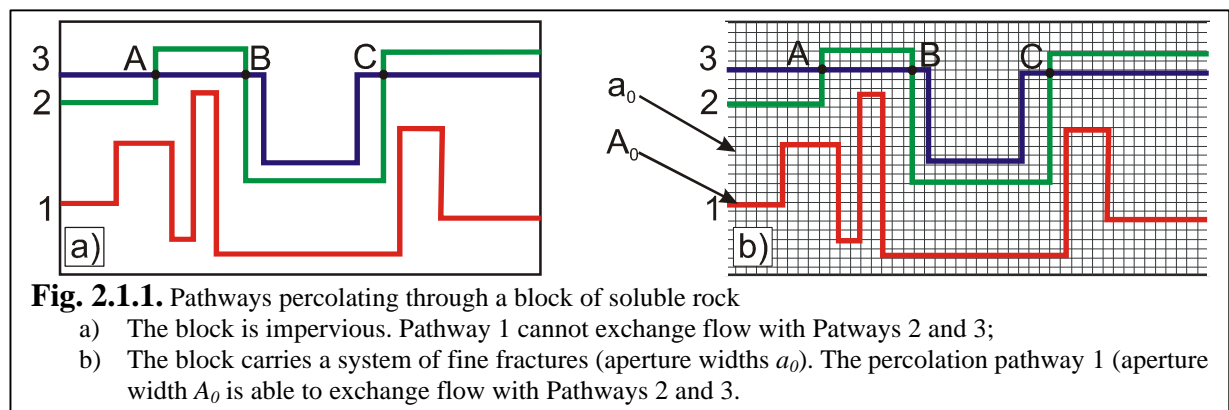
Our model is capable to solve various problems including ones with complex geological settings. We are able to apply different values to the parameters of every single fracture from the modeling domain.



2. Influence of exchange flow on the early evolution of karst aquifers

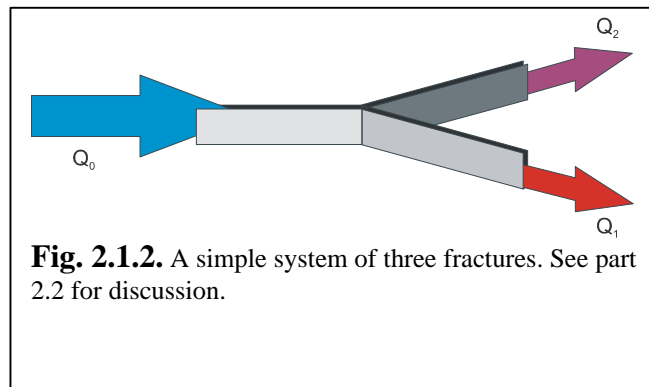
Although it sounds trivial, the term **single conduit** sometimes is used in a context, which can lead to wrong conclusions. It is important to notice that the only way for this conduit to exchange fluid is through its entrance and its exit. There is no exchange of flow along its entire length. This is the type of fracture termed single or isolated throughout this work.

Fig. 2.1.1a depicts percolating pathways embedded into a continuous and impervious block of soluble rock. It is obvious, that every straight part of any of the pathways can be defined as a single conduit with an entrance, which is the exit of the preceding fracture. But in the context of the definition above, the whole pathway 1 can be defined as a single conduit. Its length is equal to the sum of the lengths of all straight fractures, which form it. For the pathways 2 and 3 this is not true. They are connected at the points A, B and C, and therefore they can exchange flow. This can have a significant influence on their evolution.



Imagine now, that the block is not impervious, but has a structure of fine fractures - Fig. 2.1.1b. Of course any of them has its own width and length, but in the beginning for simplicity we assume that they are equal. Now the percolating pathways are part of a network. What makes them different from the surrounding fine fractures is their initial aperture width. The question is whether the percolating pathway 1 still can be accepted as an isolated conduit, in this new situation, or not? Another question is: How can the fine network influence the evolution of the percolating pathways? These questions will be answered in the following chapter.

2.1. Interaction of fracture and conduit flow in the early evolution of karst aquifers



This chapter has two parts. The first part deals with the evolution of a wide fracture (initial aperture width A_0) embedded into a continuum of narrow fractures (initial aperture width a_0) – Fig. 2.1.1b. The goal of the second part is to give better and deeper explanation of the processes and results discussed in the first

part, using a simple system of three fractures – Fig. 2.1.2.

2.1.1. Basic settings

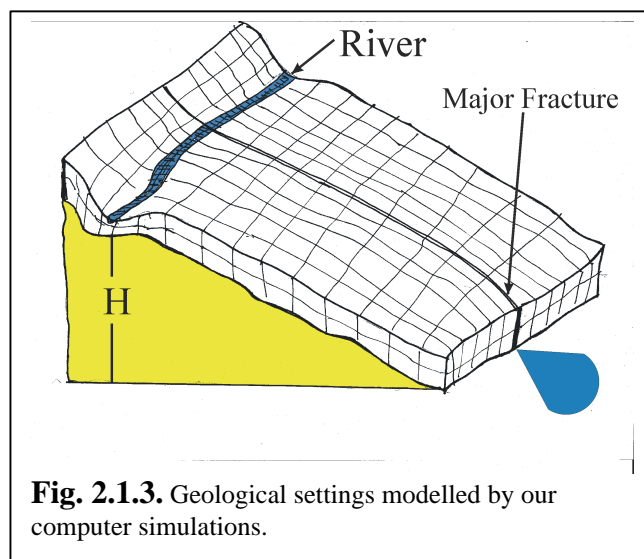
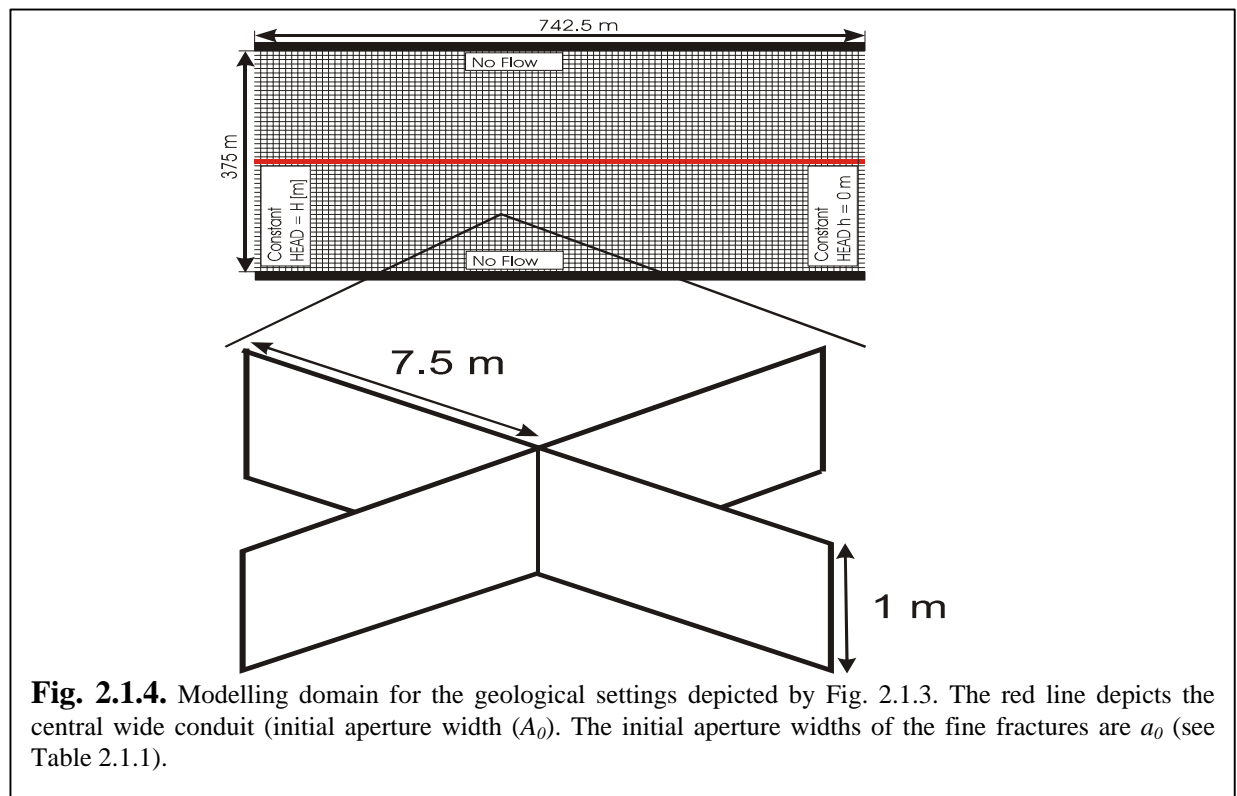


Fig. 2.1.3 shows the geological setting used as a model for the computer simulations. It depicts a limestone terrain, which has a system of small fractures. There is a central fracture with significantly larger initial aperture width than the surrounding fissures. The river on the top of the limestone bed supports a constant head boundary condition at H [m]. The right edge of the block is open. This gives us the right hand side boundary

condition – constant head at $h=0$ meters.

To model this geological setting, we create the following idealized structure – Fig. 2.1.4. The fine fissure system is represented by a two dimensional network of fractures. All geometrical parameters and the values for the boundary conditions are shown in Table. 2.1.1.



The constant head H [m] boundary condition applied on the input site is typical for the early stages of the karst evolution. During this time, the fractures have relatively small aperture widths. A small amount of flow is carried through. Dissolution is active along them and they are widened continuously. This lowers their resistance, and the flow increases. The consequence is faster widening, further increase of flow, and this positive feedback loop causes the breakthrough event (Dreybrodt 1996, Dreybrodt and Gabrovsek 2000). After breakthrough the flow continues to increase, until there is not enough water on the input site to support the constant head boundary condition. At this moment the computer runs for this study were terminated. They could be continued further, but then a constant recharge boundary condition should be used. This is not in the scope of our interest for the selected scenario.

Parameter	Value	Unit
Length of the limestone bed	742.5	Meters
Width of the limestone bed	375	Meters
Distance between the horizontal fractures	7.5	Meters
Distance between the vertical fractures	7.5	Meters
Number of horizontal fractures	99	-
Number of vertical fractures	50	-
Head on the input side of the domain - H	100, 10, 3	Meters
Head on the output side of the domain - h	0	Meters
Initial aperture width of the central fracture A_0	0.03	Centimeters
Initial aperture width of the narrow fractures for scenario A - a_0	10^{-5} -0.03	Centimeters
Mean of the log – normal distribution of the aperture widths of narrow fractures for scenario B - a_0	10^{-5} -0.03	Centimeters

Table 2.1.1. Basic hydrological parameters

On the right hand side a constant head boundary condition $h=0$ m is applied, to simulate the open flow out of the network (see Fig. 2.1.3). The upper and the lower part of the domain are considered as impervious.

The central fracture is constructed by a sequence of 99 horizontal fractures with initial aperture widths A_0 , and is depicted by the thick red line on the figure.

In this model we deal with limestone. Therefore the dissolution kinetics used here is typical for limestone. It follows a linear rate law until a concentration of c_s (see Table 2.1.2) and then switches to a fourth order rate law. For details see (Dreybrodt and Eisenlohr 2000). All the chemical parameters are shown in Table. 2.1.2

Parameter	Value	Unit
Temperature of the water	10	°C
Calcium concentration of the input water - c_{in}	0	mol/cm ³
Switch concentration - c_s	$1.8 \cdot 10^{-6}$	mol/cm ³
Equilibrium calcium concentration - c_{eq}	$2 \cdot 10^{-6}$	mol/cm ³
Diffusion constant - D	10^{-5}	cm ² /s
First order kinetics rate constant - k_1	$4 \cdot 10^{-11}$	mol cm ⁻² s ⁻¹
Fourth order kinetics rate constant - k_4	$4 \cdot 10^{-8}$	mol cm ⁻² s ⁻¹

Table 2.1.2. Basic chemical parameters

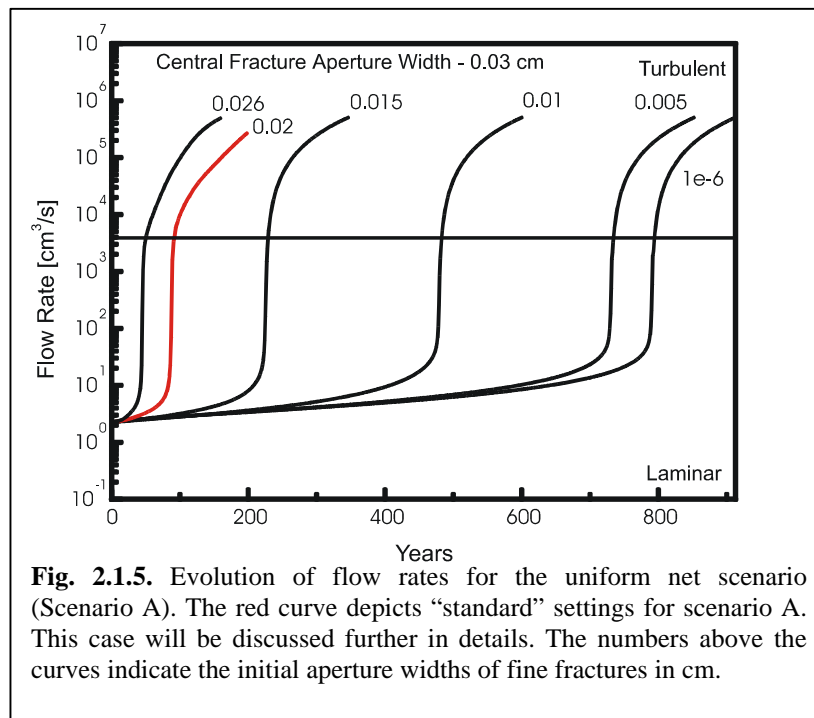
Two basic scenarios (A and B) are discussed. The initial aperture width of the central fracture ($A_0=0.03$ cm) is the same for both of them. The initial aperture widths of the fine fractures network are all equal for scenario A. This produces a uniform, rectangular net with the parameters shown in Table.2.1.1. For scenario B the initial aperture widths of the fine

fractures are log-normally distributed. This is an attempt to create a setup, closer to reality. On the other hand the uniform network is easier to interpret.

The goal is to investigate the influence of the fine fracture network on the evolution of the central fracture. Therefore we vary the properties of the surrounding network and observe the reaction of the central conduit.

2.1.2. Numerical results

2.1.2.1. Influence of the exchange flow on the breakthrough times

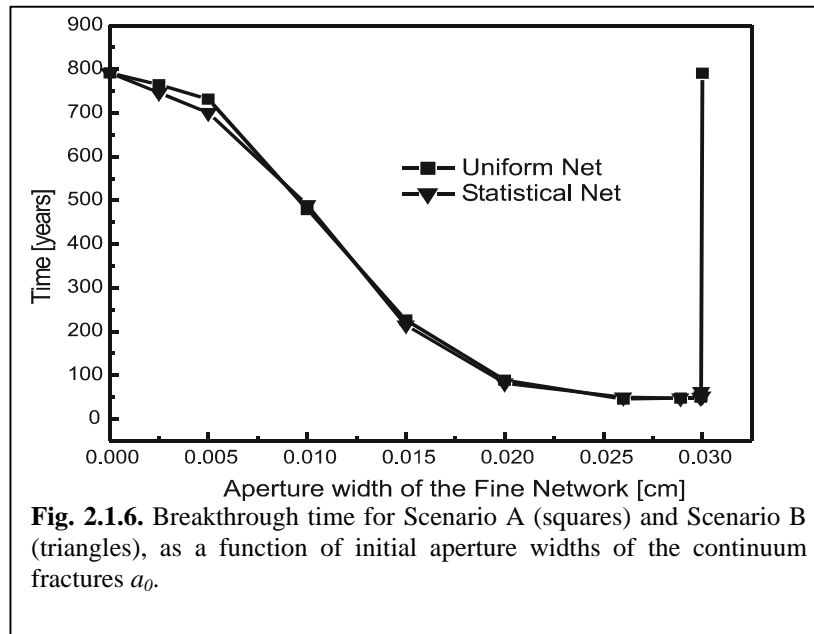


We start with the first set of simulations. The head on the left hand side boundary is fixed at 100 m. This head is extremely high and is related to man made situations, as for example the situation below a dam site in a karst region. The initial aperture widths a_0 of the fine fractures are varied from 10^{-5} to 0.03 cm and A_0 is fixed at 0.03 cm for the central conduit (see Table 2.1.1). The evolution

of the amount of flow through the domain for various values of a_0 (scenario A) is depicted on Fig. 2.1.5. The first impression is that all curves look similar, but are shifted in time. They have three main parts. The initial part shows a slow increase of the flow for a certain time period, the almost vertical second part depicts the breakthrough time and the fast increase at this moment, and the third part illustrates the continuous increase after the breakthrough event under turbulent flow conditions. Fig. 2.1.6 shows the dependence of breakthrough time on the initial aperture width a_0 for both scenarios A and B. The curves look almost identical, which means that for the period until breakthrough, the evolution of the two systems (uniform and statistical), at least as a basic behavior, is similar. The breakthrough time is maximal when:

- The aperture widths of the fractures of the surrounding network are negligibly small ($A_0 \gg a_0$);

- b) The aperture widths of the fine fractures are the same as the aperture width of the central fracture ($A_0 = a_0$). This is possible only for the uniform scenario A.



In the first case the resistances of the surrounding fractures are so high, that the flow they can carry is close to zero. Consequently the exchange between the central fracture and the surrounding network is also close to zero and the central fracture can be regarded as an isolated one. In the other extreme case, the

head distribution is uniform along the whole network (only for the uniform networks). Practically there is no pressure difference between the central fracture and the surrounding network. The flow lines are parallel to the upper and to the lower boundaries and there is no exchange of water. In both cases, there is no flow out from the central fracture into the continuum and the breakthrough times should be equal to that of an isolated fracture. This is exactly what can be seen on the picture.

If the aperture widths of the fine network are increased, then the flow out from the central fracture into the network is also increased. As a consequence, more aggressive water penetrates deeper into the central conduit. This accelerates its evolution and the breakthrough time becomes shorter. Details about this behavior will be presented in the second part of this chapter.

A reasonable question is: What would happen if the initial widths of the surrounding fractures were increased even further, beyond the size of the central one. Then their breakthrough times would be shorter in comparison to the breakthrough time of the central fracture, and the breakthrough event will happen in the surrounding network. Our goal, however, is to show the evolution of the central conduit. Therefore we will not continue the curve in Fig. 2.1.6 further.

2.1.2.2. Evolution of the fracture aperture widths (standard scenarios A and B)

The red curve on Fig. 2.1.5 shows the evolution of the flow for the setup with initial aperture widths of the fine net, $a_0=0.02$ cm. This is the basic (standard) setup for our simulations. For the case of scenario B, the standard setup has log normally distributed initial aperture widths of the fine fractures with average $a_0=0.02$ cm and $s=0.01$.

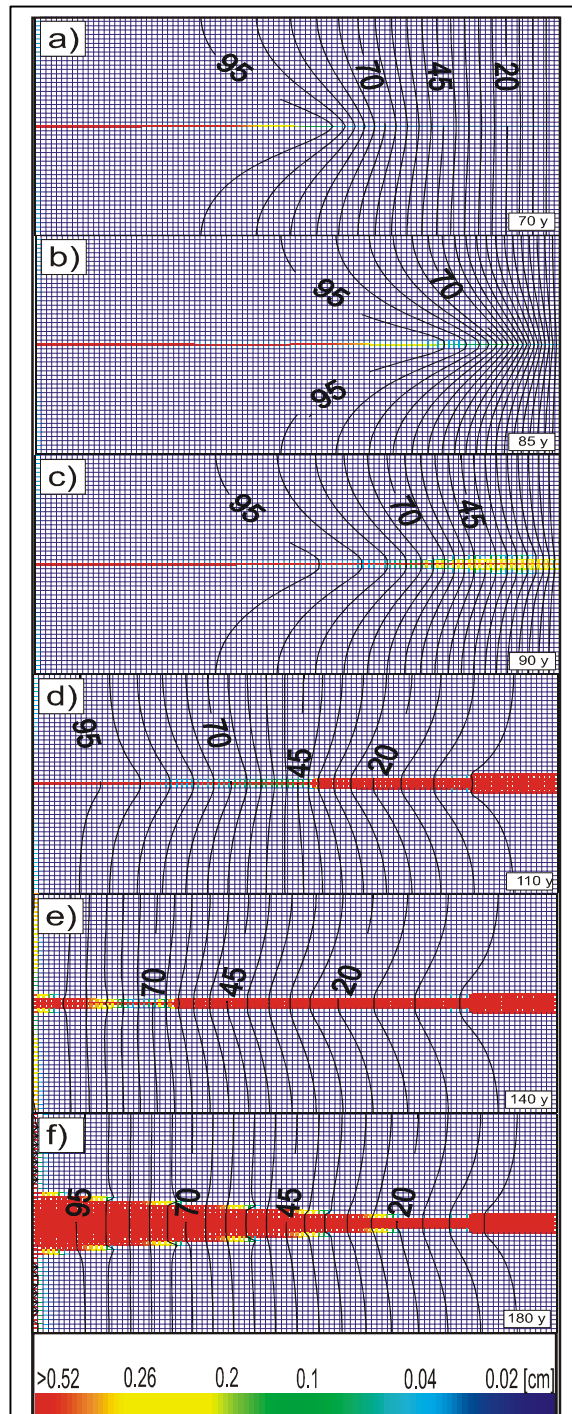


Fig. 2.1.7. Evolution of fracture aperture widths for the standard scenario A. The color code depicts the fracture aperture widths in centimetres. The head distribution is illustrated by the black lines of constant head in steps of 5m. The numbers in the lower right corner depict the time.

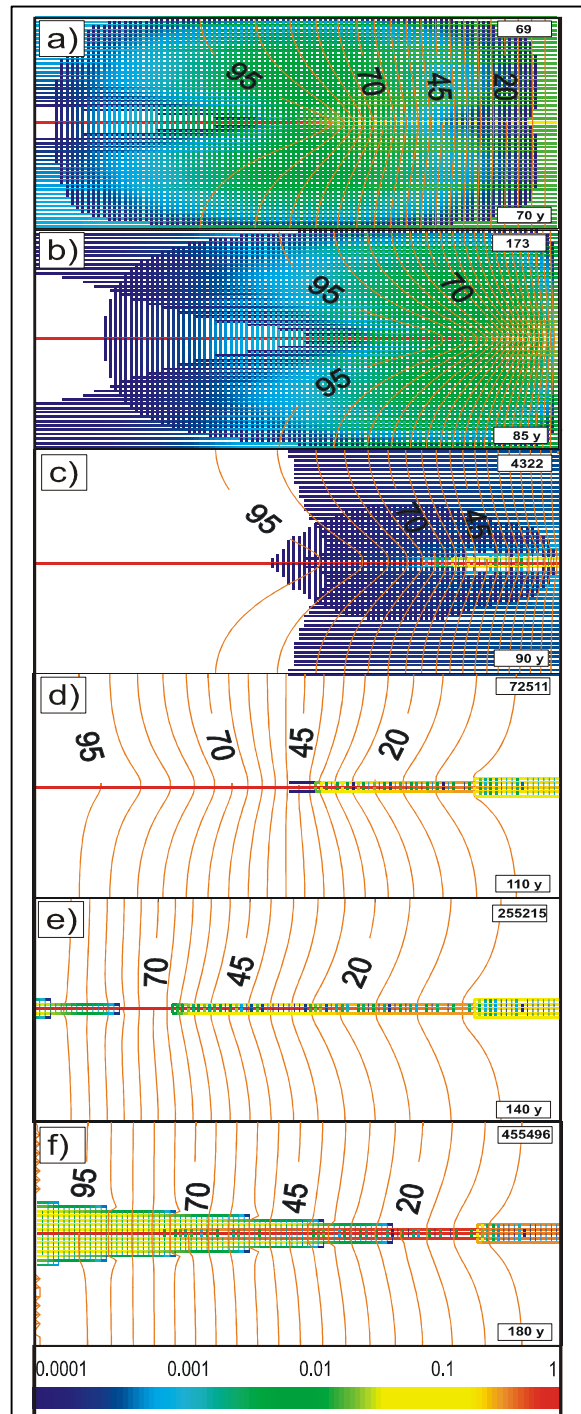
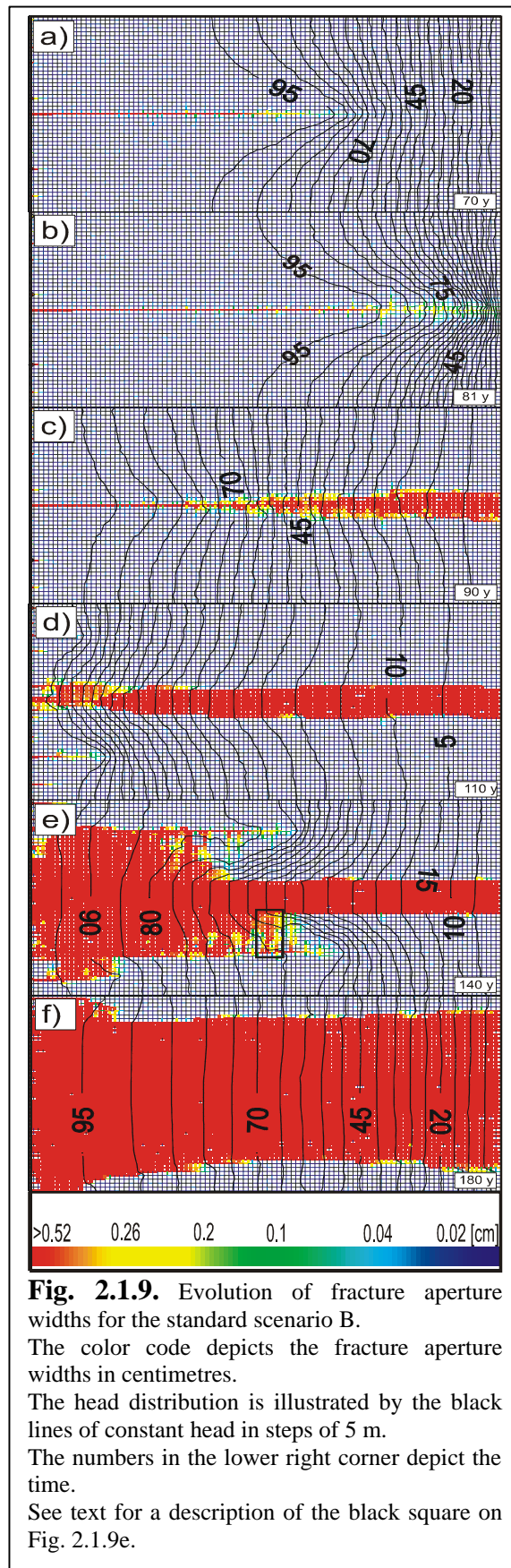


Fig. 2.1.8. Evolution of flow rates for standard scenario A. The color code depicts the ratio between the flow rate through the current fracture and the maximal flow rate, which occurs at that time in the net. The value of the maximal flow rate in cm^3/s is depicted at the upper right corner. The head distribution is illustrated by the orange lines of constant head in steps of 5m. The numbers in the lower right corner depict the time. Note that all fractures carrying flow 10000 times smaller than the maximal are not displayed.



The evolution of the aperture widths for both scenarios A and B is presented in Fig. 2.1.7 and Fig. 2.1.9. Note that these are presented enlarged during the discussion. The color code depicts the fracture widths in centimeters, and the black lines show the head distribution inside the domain. As already discussed, both curves in Fig. 2.1.6 are similar for the statistical and the uniform cases. Therefore, we expect similar evolution during the period before the breakthrough. This is clearly visible in Fig. 2.1.7a and Fig. 2.1.9a. In both cases a conduit propagates downstream along the central channel. From the pressure head distribution the outflow into the surrounding environment can be visualized. Of course, there are differences in the details. Some fissures are initially wider than 0.02 cm in the statistical case. They open relatively fast if the conditions at their entrances and exits are suitable (high pressure gradient, and low calcium concentration for example). This is the case for the widened fractures on the left hand side boundary and for the ones around the tip of the central conduit (see Fig. 2.1.9).

To make the things easier to understand, the flow distribution for the uniform case over the whole network is illustrated by Fig. 2.1.8. The color code depicts the ratio between the flow rate through the current fracture and the maximal flow rate, which occurs in some fracture of the network. The value of this maximal flow rate is depicted at the upper right

corner of every figure. All fractures carrying flow 10000 times smaller than the maximal one are omitted from the figure. The orange lines depict the pressure head distribution as in Fig.

2.1.7. Fig. 2.1.8a depicts the situation at 70 years. The flow out from the central fracture to the surrounding environment starts close to the left hand side boundary. It increases with the distance from the entrance and becomes maximal at the tip of the opened central conduit. After that it decreases. Close to the exit there is no exchange between the central conduit and the surrounding network. After the tip in the direction of the right hand side border, there is a zone, where the pressure lines are perpendicular to the central fracture. This means that the flow, which comes out at the tip is diffused into a large area of fractures. Consequently the aggressive water widens the fractures closest to the central one. The more distant fractures remain largely unaffected because of the large area and the relatively high calcium concentration. The flow distribution on the right hand side boundary is even and still unaffected by the penetrating channel (see Fig. 2.1.8a).

Fig. 2.1.7b and Fig. 2.1.9b depict the situation after 85 years for the uniform case and after 81 years for the statistical one. This is shortly before breakthrough. The significantly widened part of the central conduit is already close to the exit. The main outflow is at the tip of the widened part. This is also visible at Fig. 2.1.8b. There is an important difference compared to the situation at 70 years. The zone of the outflow is close to the right hand side boundary. The main consequence is that all the fluid coming out of the central fracture is not diffused anymore into a large area of unwidened fractures. It is directly connected to the open flow boundary and the water is channeled through the neighboring fractures parallel to the central conduit. This is the shortest path out of the domain (see Fig. 2.1.8b).

The central conduit carries the main outflow at the right hand boundary. The outflow decreases in the neighboring fractures and after some distance it becomes constant. The result is visible on Fig. 2.1.7b. Some fractures starting from the central conduit and perpendicular to it are wider than the rest of the fine network. In the statistical case (Fig. 2.1.9b) the number of the widened fractures is higher and their distribution is not symmetric. But the main result is similar: Fractures start to develop between the tip of the widened region of the central conduit, and the right hand side open flow boundary condition. They belong to the shortest pathway to the exit.

Figs. 2.1.7c and 2.1.9c depict the situation shortly after the breakthrough event – for both scenarios. The flow through the central conduit is already turbulent. The narrow part at the end of the central fracture is removed and the head distribution is changed. For the uniform net (Fig. 2.1.7c) the pressure lines move backward and exhibit even distribution after 110 years, Fig. 2.1.7d. There is a clearly visible fan at the downgradient end of the central fracture. The flow through it is laminar,

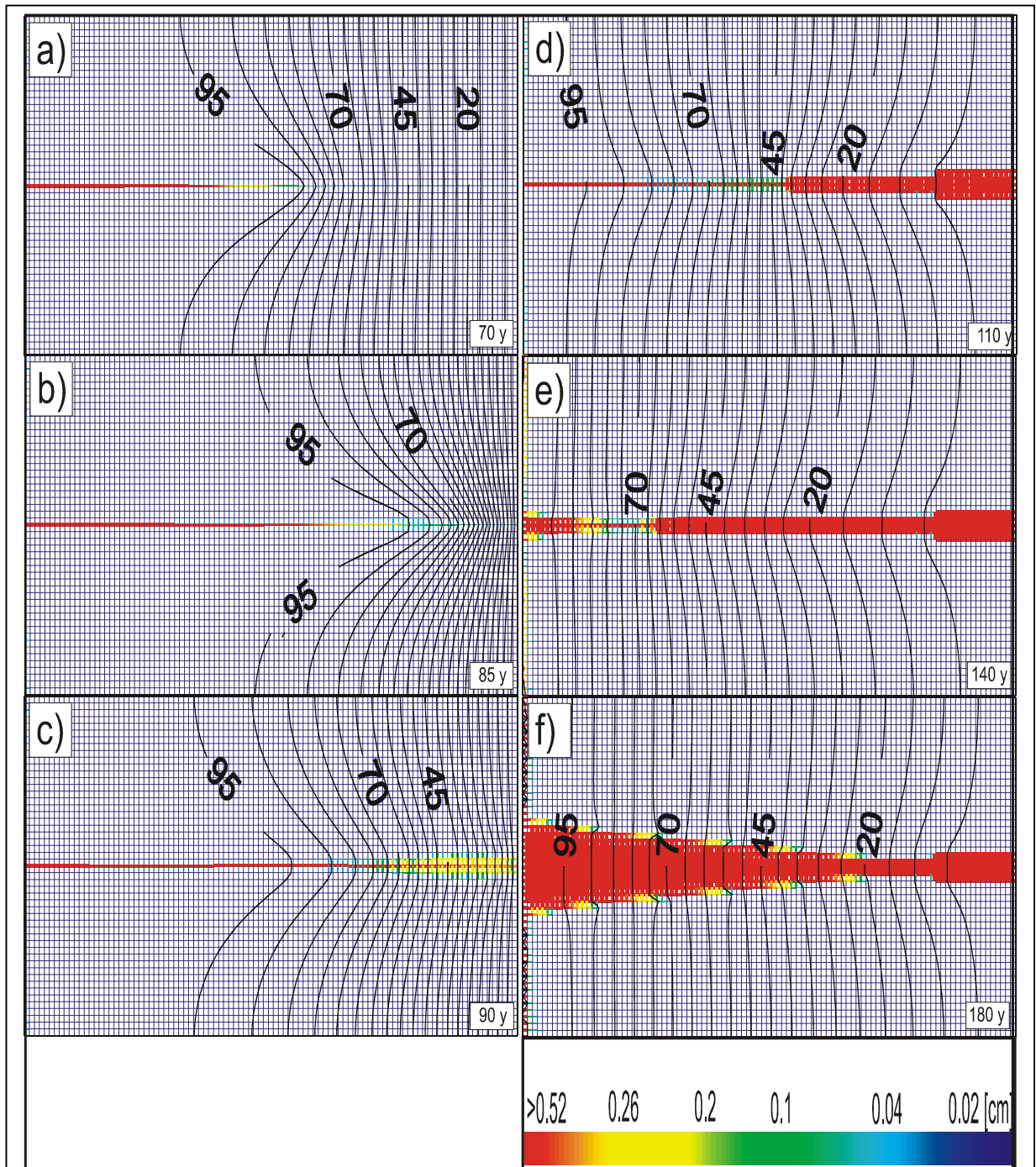


Fig. 2.1.7.(enlarged) Evolution of fracture aperture widths for the standard scenario A.

The color code depicts the fracture aperture widths in centimetres.

The head distribution is illustrated by the black lines of constant head in steps of 5 m.

The numbers in the lower right corner depict the time.

because the exits of the channels have still relatively small aperture widths. This is the reason for the head difference between the fractures belonging to the fan and the central conduit. A small amount of water is exchanged between them mainly in the direction of the central conduit (see Fig. 2.1.7c, Fig. 2.1.8c). The widening of the exit fractures of the fan shows that soon a breakthrough event will happen there and the flow through the whole fan will become turbulent. This is exactly what is observed in the statistical case (Fig. 2.1.9c). The flow through the fan is turbulent and the pressure difference between its fractures and the central conduit is close to zero. The main inflow to the fan region has moved backwards. Some perpendicular fractures start to develop on both sides of the central conduit. The water entering them is still sufficiently aggressive to initiate relatively fast widening. This increases inflow from the central conduit. The water is not diffused into the rest of the network, because of the fan developed at the exit. It propagates the influence of the right hand side boundary condition deeper inside the domain and the same mechanism, fast widening of the fractures comprising the shortest pathway to the developed part of the fan, is repeated. Consequently the fan is propagating in direction towards the entrance, on both sides of the central fracture.

This is observed in Figs 2.1.7d and 2.1.9d. They show the situation after 110 years. The flow through the fan is already turbulent as depicted by the red, thick fractures. The pressure is now evenly distributed through the whole domain. One can see two regions of the head distribution. The first region starts at the left hand side of the domain and continues to the region of the fan. The flow is mainly directed from the central region to the unwidened fractures surrounding it. The pressure lines are smoother at their tips than in the situation at 70 years (see Fig. 2.1.7a). This means that the outflow is from the central fracture and also from the closest ones parallel to it. The water entering the unwidened part of the domain has lost most of its dissolutional power in the area where the fan grows actively. Therefore it cannot significantly alter the net outside.

The second region of the pressure distribution starts at the beginning of the fan and propagates to the end of the network. Here the situation is exactly the opposite. The pressure lines are bended backwards, showing inflow from the outer unwidened part into the fan and into the central fracture. The concentration of the water coming from the fine fractures is close to saturation and cannot influence the evolution of the widened part. Consequently, the widening of the fan region is limited, and the only direction of growing is backwards towards the entrance of the domain. This is observed at the later stages of the evolution.

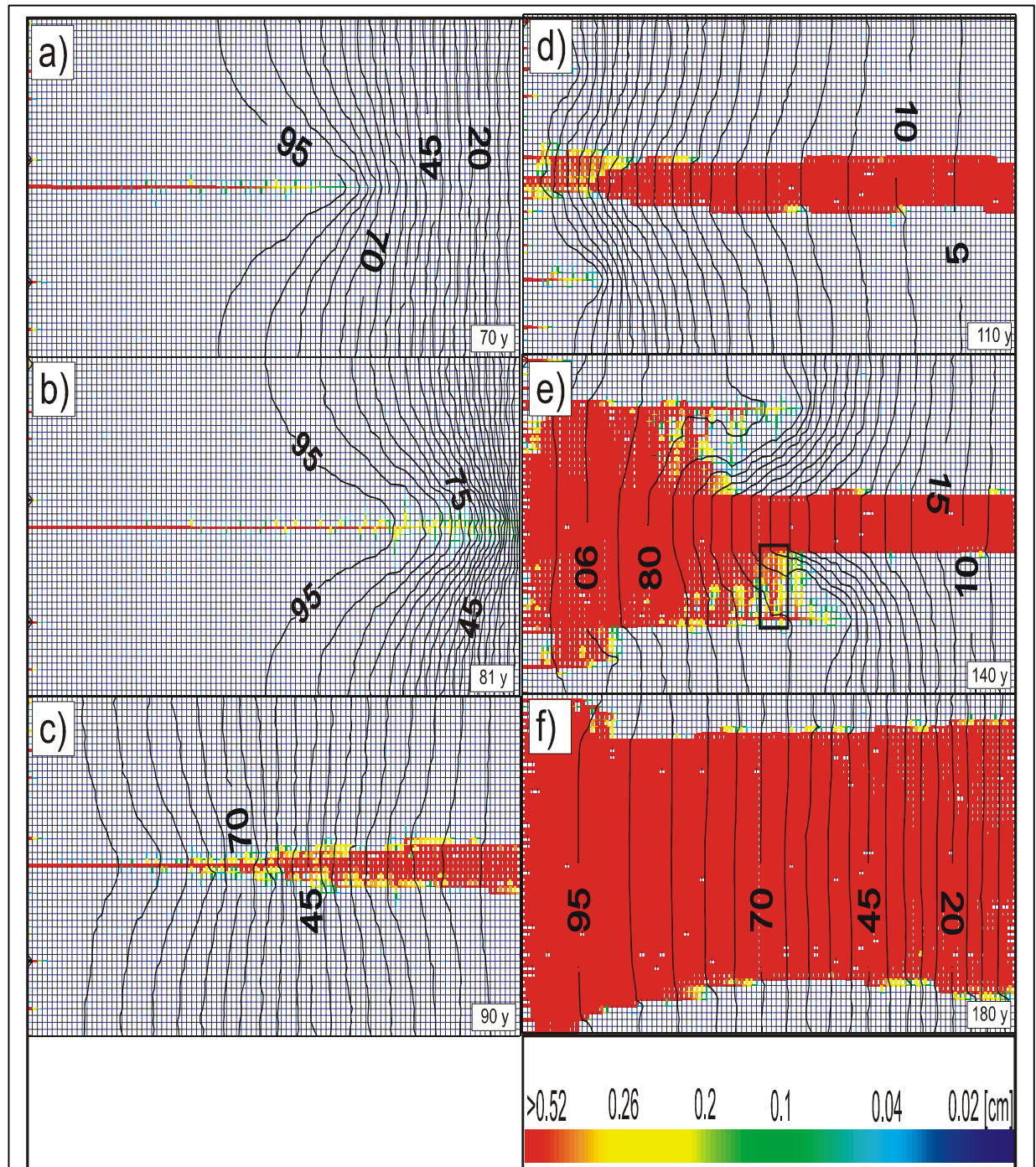


Fig. 2.1.9.(enlarged) Evolution of fracture aperture widths for the standard scenario B.

The color code depicts the fracture aperture widths in centimetres.

The head distribution is illustrated by the black lines of constant head in steps of 5 m.

The numbers in the lower right corner depict the time.

See text for a description of the black rectangle on Fig. 2.1.9e.

The situation for the statistical scenario is shown by Fig. 2.1.9d. The exit fan is wider and not symmetrical, but the same behavior is observed. It stops to grow in the direction perpendicular to the central conduit.

In the statistical case, due to more favorable pathways, some channels grow from the entrance (left hand side boundary) downstream towards the exit fan.

Let us have a look at the situation 30 years later. It is depicted on Fig. 2.1.7e for the uniform and on Fig. 2.1.9e for the statistical scenario. Fig. 2.1.9e looks already quite complicated. We start with a description of the uniform case. The fan is growing further upstream towards the entrance. At the same time there is no growth in the direction of the impervious boundaries, because of the saturated inflow coming from the fine network. The outflow is concentrated to the fan and the central fracture, (see Fig. 2.1.8e). In contrast to the right hand side, the changes in the left hand region are significant. There is a second fan, propagating down stream in the direction towards the exit. It is formed by the central fracture and the two parallel neighboring fractures. In contrast to the exit fan it is growing from the neighboring fractures in the direction of the central conduit (see Fig. 2.1.7e). The growth of the exit fan is supported by the relatively aggressive solution flowing out of the central fracture into the fine network. The situation for the fan at the entrance is different. The horizontal fractures forming the left hand side border of the domain are widened. The initial aperture width (a_0) of these fractures is 0.02 cm for this scenario. According to Dreybrodt (1996) and Dreybrodt and Gabrovsek (2000), the breakthrough time of the single fracture is proportional to the 3rd power of $(1/a_0)$, for $n=4$ (see Table 2.1.2). A fracture with 0.02 cm initial aperture width, will take almost 3.4 times longer time for breakthrough than a fracture with initial aperture width 0.03 cm. A period of 140 years is long enough to observe widening in the fractures forming the entry part of the fine network. In our case, the fractures away from the central conduit (in the direction of the impervious boundaries) had different pressure head at their exits than the fractures close to it during the whole evolution so far (see Figs. 2.8a-e). This explains the observed differences in the aperture widths of the entry fractures close to the central conduit and the ones away from it.

The entry fan starts to grow from the first pair of fractures neighboring the central conduit and parallel to it. All entry fractures (including the first pair) have enough time to widen considerably. This increases the pressure head at the nodes of their exits. Consequently the pressure distribution along the entire entrance part of the domain is changed (see Fig. 2.1.7e). There is a zone of inflow to the central conduit. It starts at the ends of the fractures forming the left boundary of the domain, and ends at the tip of the entry fan. Part of the water is diverted

directly to the central conduit, through the perpendicular connecting fractures, and the other part continues to flow parallel to it. This water is still aggressive, and causes fast widening. In this particular case the presence of the exit fan diverts a relatively high amount of water in the direction parallel to the central conduit, and consequently the growth of the entry fan is fast in both directions (forward – parallel to the flow) and in the direction perpendicular to the central channel. Actually there is no mechanism to stop growing of the entry fan. The water, entering the domain on the left hand side is aggressive, and if there is a wider central conduit, then sooner or later the evolution will come to a phase when the flow will be diverted towards this wider fracture. This is the moment when the entry fan starts to grow until the whole domain is conquered.

The pressure distribution, in the transition zone between the entry and the exit fans, matches the switch between the mechanisms governing their growth. Next to the end of the entrance fan, the flow is already parallel to the central fracture, and the exchange is close to zero. This depicts the beginning of the zone, where the exit fan is developing.

Fig. 2.1.9e depicts the situation for the statistical scenario at 140 years. The widened fractures on the left hand side are forming the entrance fan (see Fig. 2.1.9e). In Fig. 2.1.9e this fan is already connected with the exit fan and the whole central zone exhibiting widened aperture widths (red region) can be considered as one huge central fracture. As already discussed, there is no mechanism limiting the growth of the entry fan. It is extending further in horizontal and in vertical direction at both sides of the central zone. The area of the inflow to the central fractures is extending from the left hand side of the network to the right border. The zone, where the flow was in the direction from the central channel to the surrounding network does not exist anymore. The consequence is, that the necessary conditions for the exit fan to develop, are not fulfilled anymore and its evolution is stopped.

In contrast to the uniform case, only some of the horizontal fractures, forming the left hand side border are widened (see Fig. 2.1.9e). The rest remains unchanged. On the other hand, the ones, which are widened extend deeper, than the conduits in the uniform scenario. The reason is the statistical distribution of the initial aperture widths of the fractures. Any of the widened and deeper penetrating channels, can be considered as a central wider fracture for the region, where it grows. All the conclusions, so far, are true also for this small subdomain. The widened path will continue to grow in the direction of the highest head difference. These pathways can reach directly the right hand side boundary or can divert their growth in the direction of the widened area in the central part of the domain, and connect it at a certain point (see Fig. 2.1.9e). Entrance and exit fans develop on both sides of these pathways. An example for such a

place is depicted by the black rectangle on the figure. Actually, when these pathways connect either to the central widened zone or to the right hand side boundary they exhibit their local breakthrough event.

The situation after 180 years of evolution is depicted in Fig. 2.1.7f for the uniform scenario and in Fig. 2.1.9f for the statistical one. As expected, the entry and the exit fans are already connected in the uniform scenario. The entry fan continues to grow. The pressure distribution is similar to the one for the statistical case at 140 years. The flow is directed towards the huge widened zone around the central conduit (Fig. 2.1.8f) and there is no area of inflow from the central fracture to the fine network. As already discussed, the consequence of this is the end of the evolution of the exit fan. We expect continuous growth of the entry fan in both directions – horizontal, to the exit of the domain, and vertical, in the direction of the impervious borders. This is depicted in Fig. 2.1.9f – the statistical scenario, where almost the whole domain is widened and conquered by the entrance fan.

2.1.2.3. Numerical results for the central channel (standard scenario A)

The goal of the discussion so far was to describe the evolution of the modeled aquifer from, let us call it a macro - point of view. We were trying to find the reasons for the changes in the pressure head distribution, and in the flow rates, across the whole domain. But our initial question was: What is the influence of the surrounding environment to the evolution of the central channel? In a way it looks like that the whole discussion so far was to give an answer to the opposite question. What is the influence of the central channel on the evolution of the domain through which it grows? Actually this is not true. The idea is to show that these processes can be studied separately only in some special cases, namely when the initial aperture widths of the fractures consisting the surrounding network (a_0) are negligibly small, or when a_0 is equal to the initial aperture width of the central conduit A_0 .

We change the point of view and discuss the evolution of the central channel in details. We use our standard scenario A and study:

- a) the pressure head distribution – depicted on Fig. 2.1.10a;
- b) the flow through the central channel – depicted on Fig. 2.1.10b;
- c) the change of the aperture width along the channel – Fig. 2.1.10c;
- d) the change of the concentration along the central conduit, depicted as the ratio between the actual concentration at a certain point and the equilibrium concentration – Fig. 2.1.10d.

We want to understand the influence of the surrounding environment to the evolution of the central conduit. This is why it will be useful to compare it to the evolution of the same quantities (pressure head, flow rate, aperture width, and concentration), for the case of an isolated fracture, with length equal to that of our model aquifer (742.5 meters), the same initial aperture width $A_0=0.03$ cm, and the same boundary conditions (see Table 2.1.1) as for the central channel in scenario A. The evolution is depicted on Fig. 2.1.11 a-d. The colors of the curves on both figures (Fig. 2.1.10a-d and Fig. 2.1.11a-d) show the regime of the flow through the conduits. Red lines depict the evolution under laminar flow conditions. The green color is used to outline the transition between laminar and turbulent flow, and actually depicts the situation shortly before and shortly after the breakthrough event. The evolution under the turbulent flow regime is depicted by the blue curves. The timescales for the evolution for both cases (isolated central fracture, and the standard scenario – $A_0=0.03$ cm and $a_0=0.02$ cm) differ by almost one order of magnitude. This is visible on Fig. 2.1.6 and Fig. 2.1.5. The breakthrough time for an isolated conduit is about 800 years, while in our standard scenario it is 86 years (the red curve on Fig. 2.1.5). This is the reason for the different times between the profiles of Fig. 2.1.10 and Fig. 2.1.11. For the case depicted on Fig. 2.1.10 (this is the standard non isolated scenario) the time steps between the red curves are 10 years for the period between 0 and 80 years. The green curves are plotted with time difference of 2 years for the period between 82 and 90 years. The blue curves have a time difference of 10 years for the standard scenario. For the isolated conduit the time steps are as follows: 100 years for the red curves (0 to 700 years), 10 years for green (710 to 740 years), and again 10 years for the blue curves (750 to 850 years).

Before starting the discussion about the differences in the evolution between an isolated conduit and the same conduit embedded into a fine network, let us underline something, which

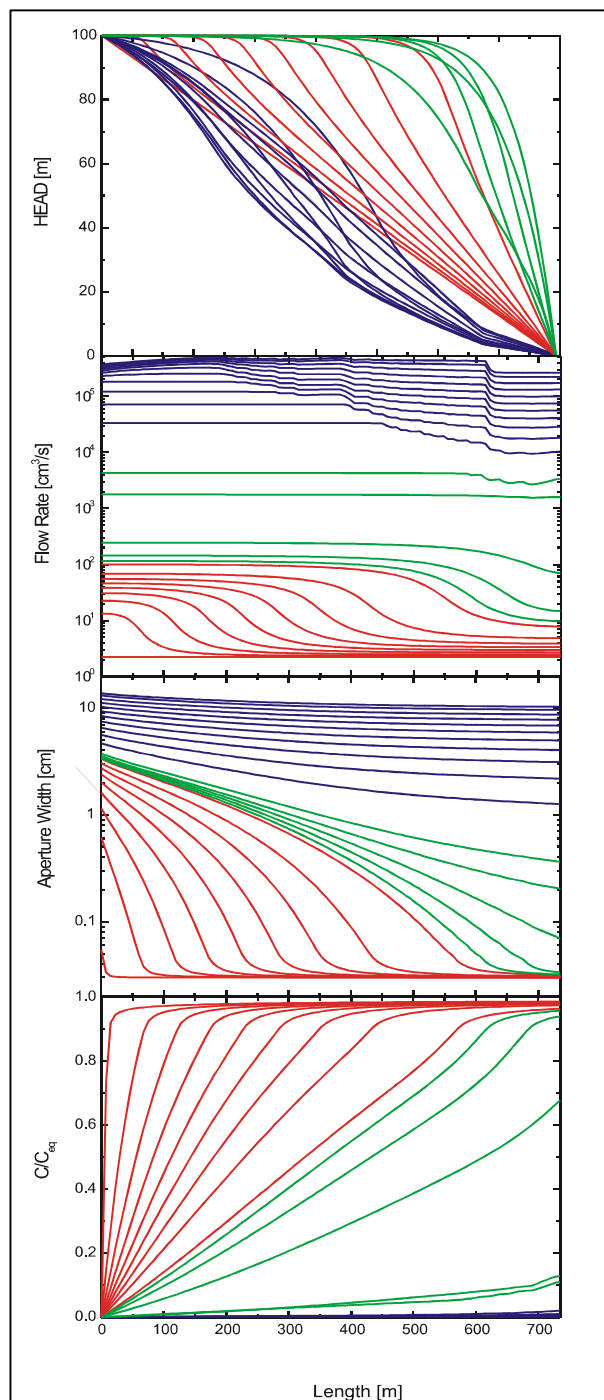


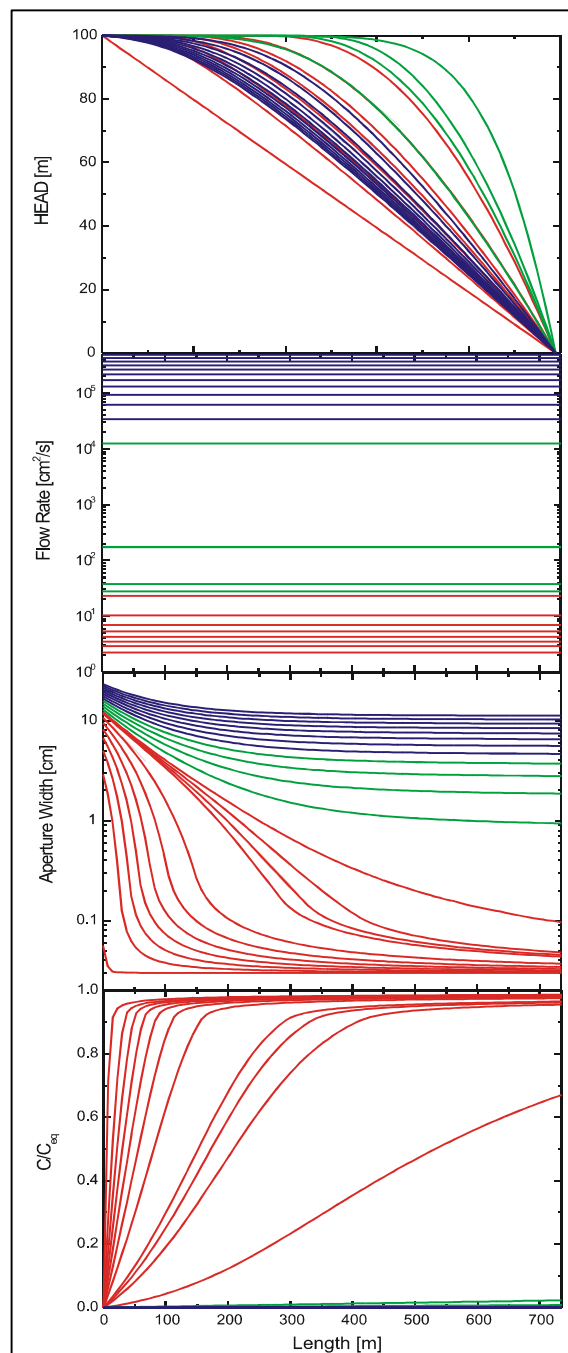
Fig. 2.1.10. Evolution of the profiles along a non isolated conduit for:

- pressure head;
- flow rate;
- aperture width;
- concentration relative to c_{eq} .

Red lines – 0 to 80 years at every 10 years;

Green lines – 82 to 90 years at every 2 years;

Blue lines – 90 to 185 years at every 10 years



2.1.11. Evolution of the profiles along an isolated conduit for:

- pressure head;
- flow rate;
- aperture width;
- concentration relative to c_{eq} .

Red lines – 0 to 700 years at every 100 years;

Green lines – 710 to 740 years at every 10 years;

Blue lines – 750 to 850 years at every 10 years

follows directly from the initial and the boundary conditions. Initially the pressure head is evenly distributed and linearly decreasing along the isolated and the non-isolated channel, as

well as along the whole fine network (Figs. 2.1.10a and 2.1.11a). The reason to select the scenario with the uniform initial distribution of the aperture widths of the fractures of the fine network is exactly this initial pressure head distribution. There is no head difference perpendicular to the impervious boundaries. Consequently there is no exchange of flow between the central conduit and the fine network. This means that the evolution of both fractures starts from exactly the same point, and all the differences developing in the later stages are because of the presence of the fine network connected to the conduit. These differences are clearly visible even in the earliest stages of the evolution of both channels.

We start with the period before the breakthrough event (0 years to 80 years) for the non-isolated case, and also for the isolated fracture scenario (0 to 700 years). Fig. 2.1.10c and Fig. 2.1.11c depict the propagation of the dissolutional widening downhead. Consequently the pressure distribution is changing also (Fig. 2.1.10a and Fig. 2.1.11a). For the non-isolated conduit the profiles of the pressure head show that there is almost no head difference along the widened zone of the channel. Close to the end of the widening, the head is practically equal to the head at the entrance. Because of the slower widening of the fractures in the fine network, the pressure difference in the direction to the network is high and the amount of flow leaving the central fracture is also high. The maximum is at the end of the widened zone. This is exactly what was observed on Fig. 2.1.7a. After the end of the widened part the loss of water into the continuum decreases and reaches zero at the exit of the fracture. This is depicted on Fig. 2.1.10b. In contrast to the described situation, the profiles of the pressure head for the isolated case (see Fig. 2.1.11a) are smoother and the decrease from the entrance to the end of the widened zone, and then from the end of this zone to the exit of the fracture, is slower. The curves of the flow rate along the isolated conduit are horizontal lines because no flow can be lost. The narrowest part of the fracture is acting like a bottleneck and is limiting the flow along the conduit (see Fig. 2.1.11b). As it opens flow increases in time.

The profiles of the concentration show a fast increase shortly after the entrance to a value close to equilibrium, for the isolated case (Fig. 2.1.11d). It remains almost constant to the exit of the fracture for the non-isolated case the profiles are not so steep. The concentration increases linearly along the fracture (Fig. 2.1.10d). At the beginning of the unwidened part it reaches a stable value, which remains practically unchanged along the channel, and is lower than the one for the single case. The reason for this difference is the higher inflow of aggressive solution coming from the entrance of the channel.

The transition period and the breakthrough event (the green profiles, 80-90 years for the non-isolated, and 710-740 years for the isolated conduit) start when the widened part reaches

the exit (see Figs. 2.1.10c and 2.1.11c). The pressure head has still the same shape but now the zone of the high head is almost at the end of the fracture for the non-isolated case (Fig. 2.1.10a). Actually, the green curves depict the period when the exit fan starts to develop. The profiles for the isolated case show that the zone of the high head is moved along the conduit closer to the exit, but again as in the early stages of the evolution, the profiles are not as steep as in the non-isolated case (Fig. 2.1.11a). The flow distribution depicts that the zone of the maximal outflow from the fracture to the surrounding environment is now close to the exit of the fracture, following the change in the pressure head distribution (Fig. 2.1.10b). This behavior was observed in Fig. 2.1.8b. In the case of the isolated fracture the profiles depict simply the increase of the flow rate through the fracture, because of the continuous widening along the conduit (Fig. 2.1.11b). Again the concentration profiles along the isolated channel are steeper than the ones along the non-isolated conduit, but in this case the concentration, which is reached at the end of this steep increase, is lower than before (Fig. 2.1.10d and Fig. 2.1.11d). The dissolution rates at the end of the isolated channel are considerably lower than those at the end of the non-isolated one. This is the reason for much faster widening of the exit zone, and earlier breakthrough event for the non-isolated case. The moment of breakthrough is clearly visible on all pictures (86 years for the non-isolated and 740 years for the isolated scenario). The pressure head distribution is changed and is more evenly distributed along the fractures. The zone of the high head has moved backwards along the conduits (Fig. 2.1.10a and Fig. 2.1.11a). At the same time the zone of considerable widening is already at the exit. A dramatic increase (by almost two orders of magnitude) of the flow rates is depicted in Fig. 2.1.10b and Fig. 2.1.11b. There is an interesting change, also in the concentration profiles. The increase of the concentration is almost linear along the conduits, for both cases, but the value, which is reached at their exits, is far away from the equilibrium, and is lower than the switch concentration (Fig. 2.1.10d and Fig. 2.1.11d). After the breakthrough event, the widening along the fracture will be even along its entire length. There is an interesting detail on the curve depicting the flow rate along the fracture in the non-isolated scenario at 88 and 90 years. Both curves are not smooth at the end. This is visible close to the exit for the curve depicting the situation at 88 years, and clearly visible further upstream for the curve depicting the flow rate at 90 years. The reason is the growth of the exit fan (see Fig. 2.1.7c). After the dramatic increase of the flow rates along the conduits, the flow regime is changed from laminar to turbulent. This part of the evolution is depicted by the blue profiles on Fig. 2.1.10 and Fig. 2.1.11 (100-197 years, for the non – isolated case, and 750 – 850 years, for the single conduit). The zone of the high head continues to move backwards, for the isolated fracture scenario, and

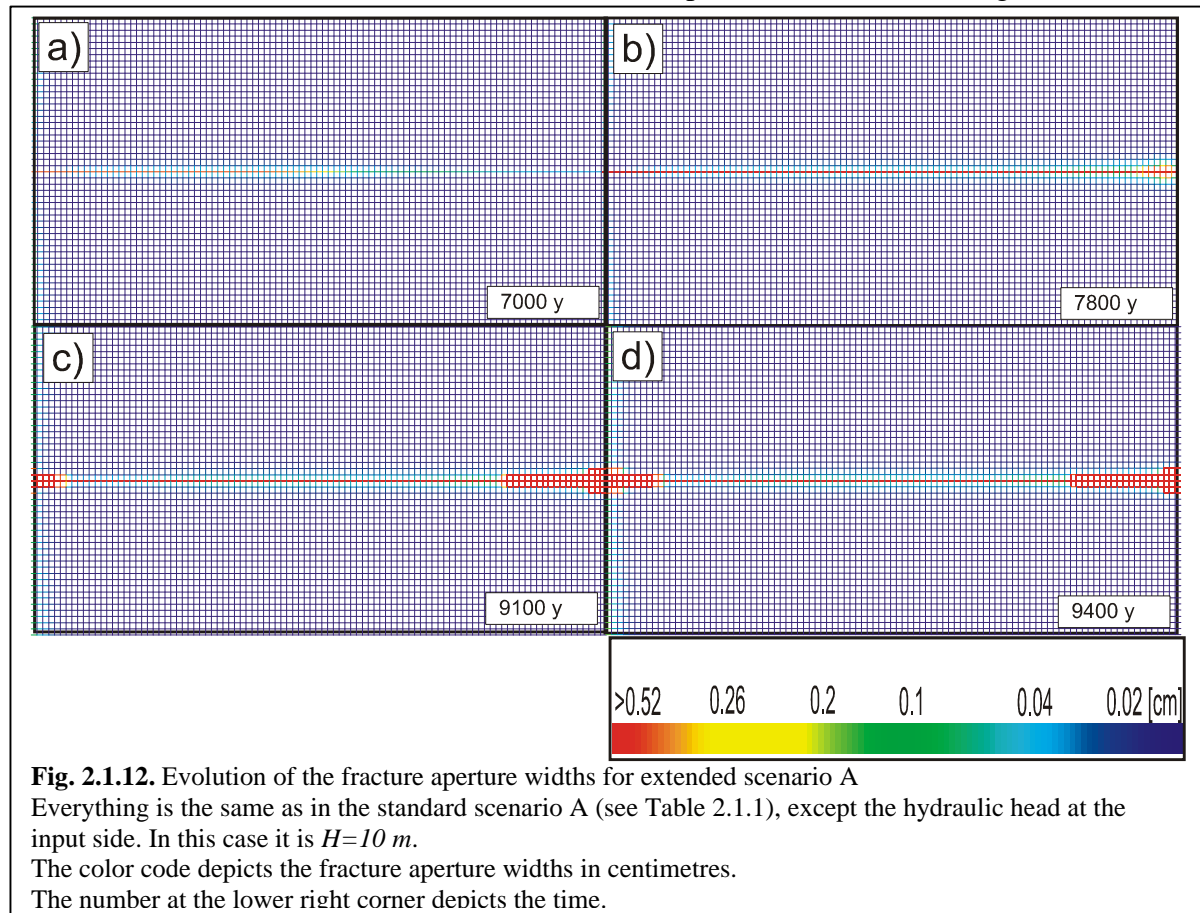
the distribution is becoming smoother (Fig. 2.1.11a). After a certain amount of time it will become even along the conduit, and will be a straight line like in the beginning of the calculations. The reason is the even widening with high linear dissolution rates along the entire profile. The case for the non-isolated conduit is more complex because of the entrance and the exit fans developing in the fine fractures network (Figs. 2.11a, 2.8d, e, f), and will be described in details in the second part of this chapter. Let us have a look at the flow rates along the conduits. For the isolated case it is clear. The flow rate increases continuously following the widening of the narrowest part of the fracture (Fig. 2.1.11b,c). For the non-isolated case, because of the strong influence of the fine fractures network, the picture is different. It is important to mention, that because of the widened zone around the central fracture, created by the fans, the profiles for this part of the evolution depict mainly the influence of the fans on the central fracture, and not of the remaining part of the network. The main interaction between the unwidened part of the fine fractured network and the central region is already with the fractures comprising these fans, and not with the central fracture. The flow rate profiles depict clearly the time and the region where the entry and the exit fans develop (Fig. 2.1.10b). As already discussed the exit fan grows backwards and its influence on the profiles is visible during the whole late stages of the evolution of the central fracture. One can easily see the place and the time where it stops to grow. The development of the entry fan is depicted by the zone of inflow close to the entrance of the conduit, on the profiles after 140 years.

As expected the concentration along the fractures, at this stages of the evolution, is close to zero and the widening is even along them. This is depicted by Figs. 2.11c, d and Figs. 2.12c, d.

2.1.2.4. Numerical results for extended scenarios

In all cases discussed so far, the pressure head on the input site of the domain is extremely high ($H=100\text{ m}$). At the same time the initial aperture widths of the fine fractures have values relatively close to the ones of the central conduit: $a_0=0.02\text{ cm}$ and $A_0=0.03\text{ cm}$, respectively.

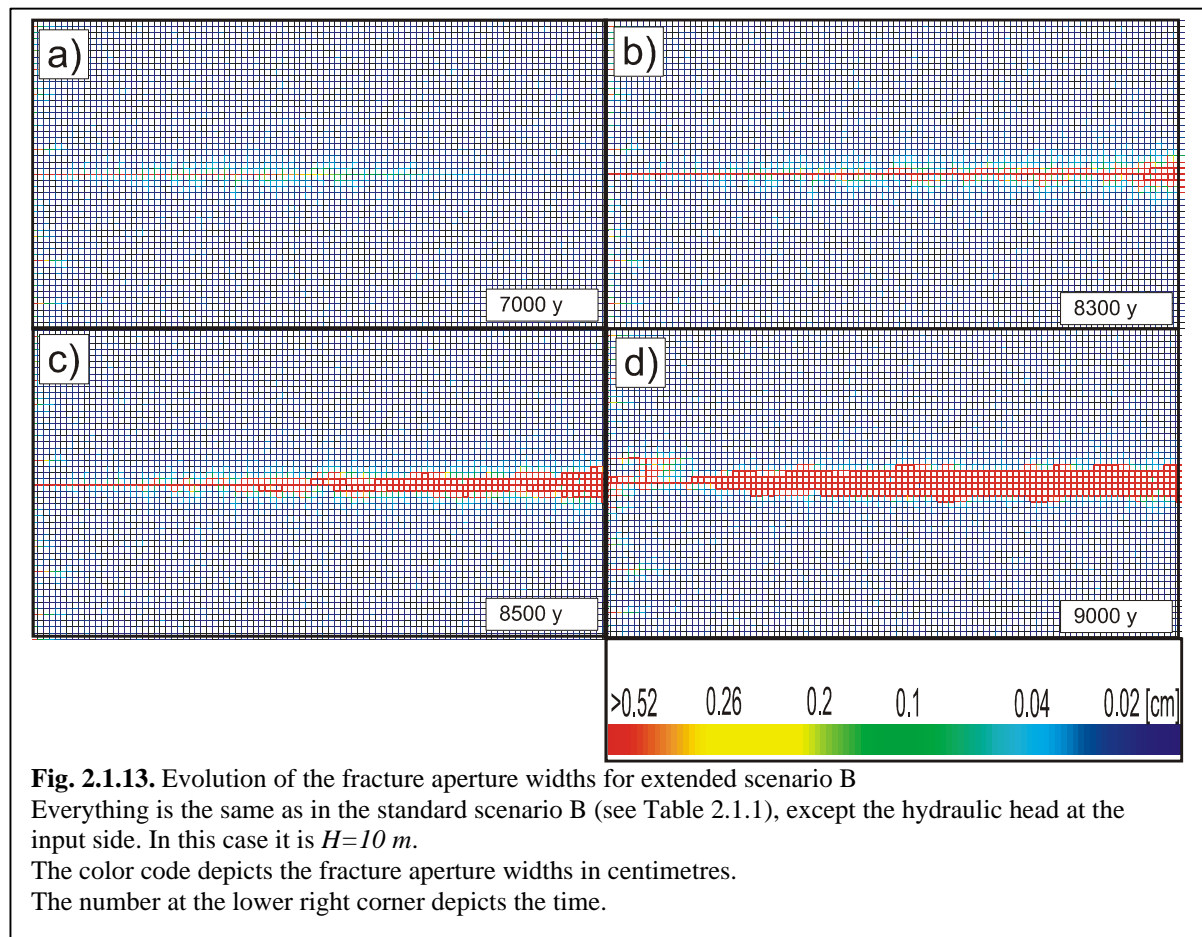
We start the next set of simulations with a change of the pressure head applied to the input site. It is fixed at $H=10$ meters. The head at the output site remains unchanged – $h=0$ meters.



The other initial and boundary conditions are the same as for the standard scenarios A and B (see Table 2.1.1). Fig. 2.1.12a-d depicts the evolution of the fracture aperture widths for the uniform scenario. Lowering the hydraulic head by one order of magnitude increases the breakthrough time of a single conduit (Dreybrodt 1996, Gabrovsek 2000). The breakthrough time of the central conduit in the case when the exchange flow was negligible and under the pressure head of $H=100$ meters is about 800 years. With a 10 times lower head it has to be in the range of 17000 - 18000 years. The breakthrough time of our uniform scenario under the pressure head $H=10$ meters is close to 7500 years. Even under the lower hydraulic gradients, the breakthrough time of the aquifer is reduced in the presence of exchange flow. Fig. 2.1.12a depicts that the central fracture starts to develop downstream. The exit fan starts to grow and at 7800 years (shortly after the breakthrough of the central conduit) some of the fractures are considerably wide – Fig. 2.1.12b. Fig. 2.1.12c depicts the situation after 9100 years of evolution. The exit fan has migrated backwards. At the same time an entry fan starts to grow downstream towards the right hand side boundary. After 9400 years, the evolution of the exit fan is stopped, but the entry fan continues to penetrate deeper into the block (Fig. 2.1.12d). After this moment the constant head boundary condition cannot be supported anymore and the

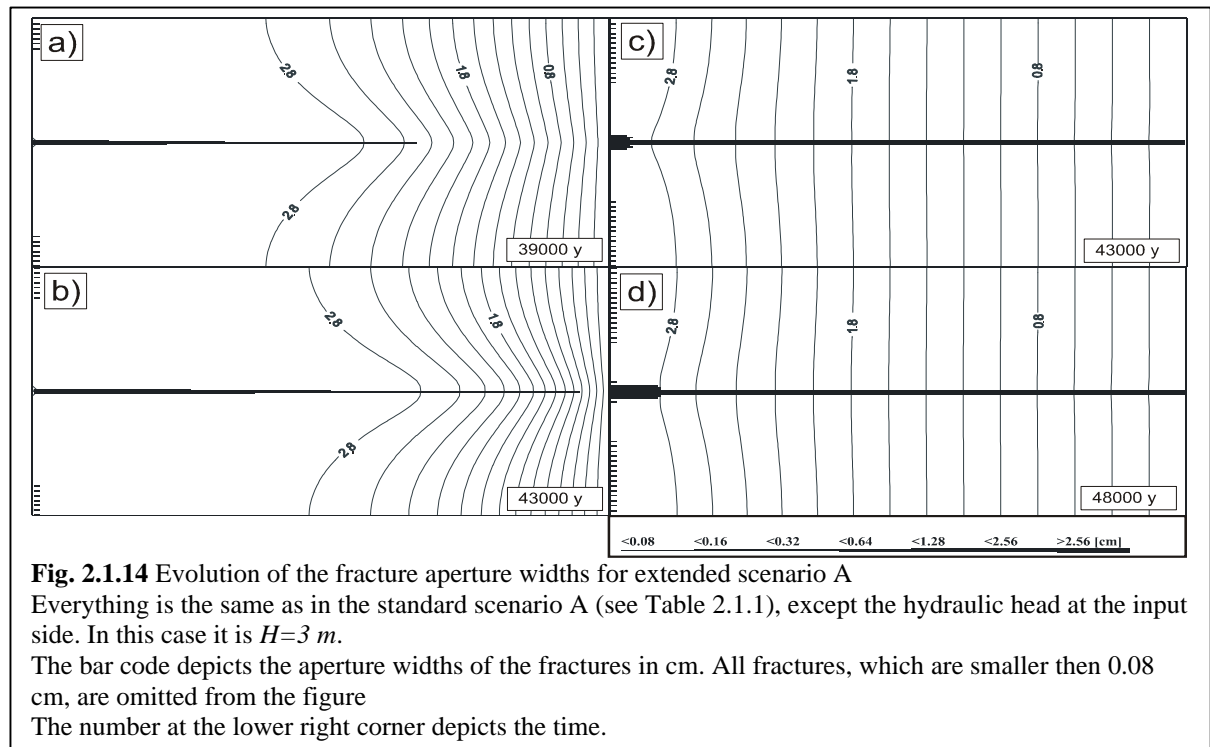
simulation is terminated. The difference with the standard scenario is the penetration distances of both fans. They are shorter. This is an important observation, because it shows that the difference between the time scales for the evolution of both hydraulic systems (the fine network and the central conduit) is important. In this case it is bigger. The fine network evolves slower with respect to the central fracture, than for the standard scenario A.

Fig. 2.1.13 a-d depicts the evolution of the statistical case. The results are similar to the

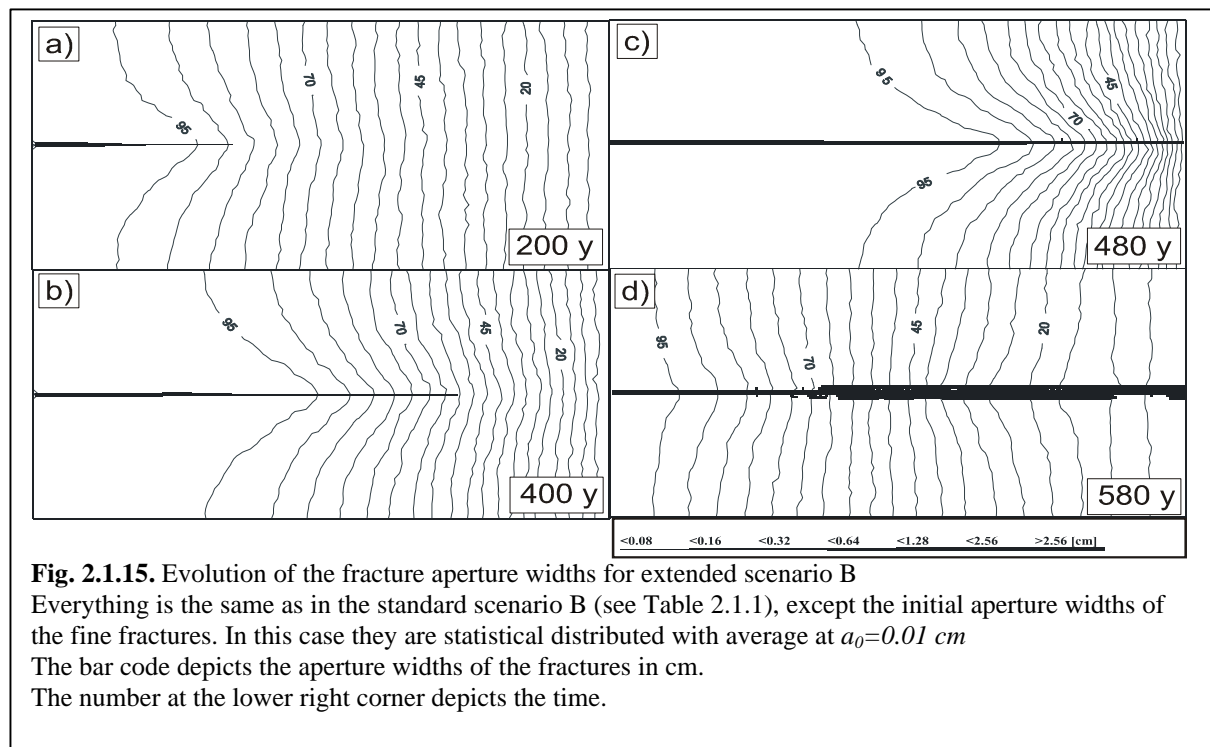


ones for the uniform scenario. Even under lower hydraulic gradients the basic mechanisms are the same but the differences of the time scales are the reason for the relatively smaller changes in the fine network with respect to the ones for the standard scenarios.

Our next experiment is to lower the head at the input part of the domain to 3 meters. This value is realistic for natural karst aquifers. Fig. 2.1.14a-d depicts the evolution of the uniform scenario. Everything else is like in the standard scenario A (see Table 2.1.1). The differences in the time scales for the evolution of the fine network and the central fracture are already so big, that there is no time for considerable changes in the network. After the breakthrough event, the central conduit continues to evolve under turbulent flow conditions. The concentration along its entire length is low and the rates of widening are close to the maximal ones. Therefore the relation between the time from the breakthrough event until the moment when the hydraulic



head can no longer be supported, and the time needed for breakthrough is decreasing with the



decrease of the hydraulic gradient. Consequently the time for the fine network to evolve is decreasing.

The next experiment has the following initial and boundary conditions. Everything (including the hydraulic head on the entrance) is like for the standard scenario B (see Table 2.1.1). The only difference is the average of the distribution of the initial aperture widths of the

fractures consisting the fine network. In this case it is set to $a_0=0.01$ cm. The result is depicted by Fig. 2.1.15 a-d. The time for the evolution of the central conduit as a single fracture is the same like the one from the standard scenario B. Because of the smaller initial aperture widths, the time for the evolution of the fine network is increased. Similar to the low hydraulic gradient case ($H=3m$), there is no time for considerable changes in the fine fractures. This is a confirmation for the conclusion, that if the time scales of both hydraulic systems are similar, then the changes in the fine network are important for the development of the karst aquifer. On the other hand, if these scales are too different, then both systems develop more or less independently.

2.1.3. Conclusion

The goal of the presented study is to show the influence of the exchange flow on the evolution of a karst aquifer. We introduce an idealized model of this aquifer (see Fig. 2.1.3 and Fig. 2.1.4). We use two different distributions of the initial aperture widths for the fractures comprising the fine network. Equal fractures for scenario A (uniform network), and a statistical distribution for scenario B. Table 2.1.1 and Table 2.1.2 depict the initial and the boundary conditions for the experiments.

The first set of simulations is under extremely high hydraulic gradients. The boundary conditions are typical for man made environment ($H=100$ m). Afterwards we decrease the gradients and perform experiments for scenarios closer to the natural situation ($H=10$ and 3 m). The last set of calculations is again under unnaturally high hydraulic gradients ($H=100$ m), but the initial aperture widths of the fine fractures are reduced ($a_0=0.01$ cm). Therefore, the influence of exchange flow on the evolution is reduced.

In this way, we study a wide range of possible geological settings. The results show that in the presence of exchange flow, the evolution of the central wide conduit is accelerated. A considerable effect is observed only for excessive values of this flow. The fine network is not changed significantly before the breakthrough event of the central conduit. Consequently the effect of the dissolution into the network is not important for the early stages of the evolution of the aquifer. Models neglecting this dissolution are reasonable approximations for these scenarios (Bauer et al. 2000). To prove this, we have performed an experiment with no dissolution into the fine network. There was almost no change in the evolution of the central fracture until the breakthrough event. The same result is observed for the cases where the time scales for the evolution of both hydraulic systems (fine net and central conduit) are significantly different. Normally these geological settings are close to the natural environment.

Models neglecting the dissolution in the fine network are a good approximation for these scenarios.

This is not true for the cases with high hydraulic gradients, or similar hydraulic conductivities of both systems. The role of the dissolution into the fine fractures is crucial for these scenarios. Especially when modeling manmade geological scenarios, or extreme natural ones, the models must take into account the changes into the surrounding media.

2.2. The influence of the exchange flow on the evolution of a single conduit

The goal of the previous section was to describe the evolution of a wide fracture embedded into a net of fine fissures. The exchange of flow between these two hydraulic systems has a significant impact on their development in time. The consequences were already discussed in details.

This part is more “process oriented”. Our aim is to understand the mechanisms and the basic laws governing the interaction between the building elements of the network.

2.2.1. Basic setup

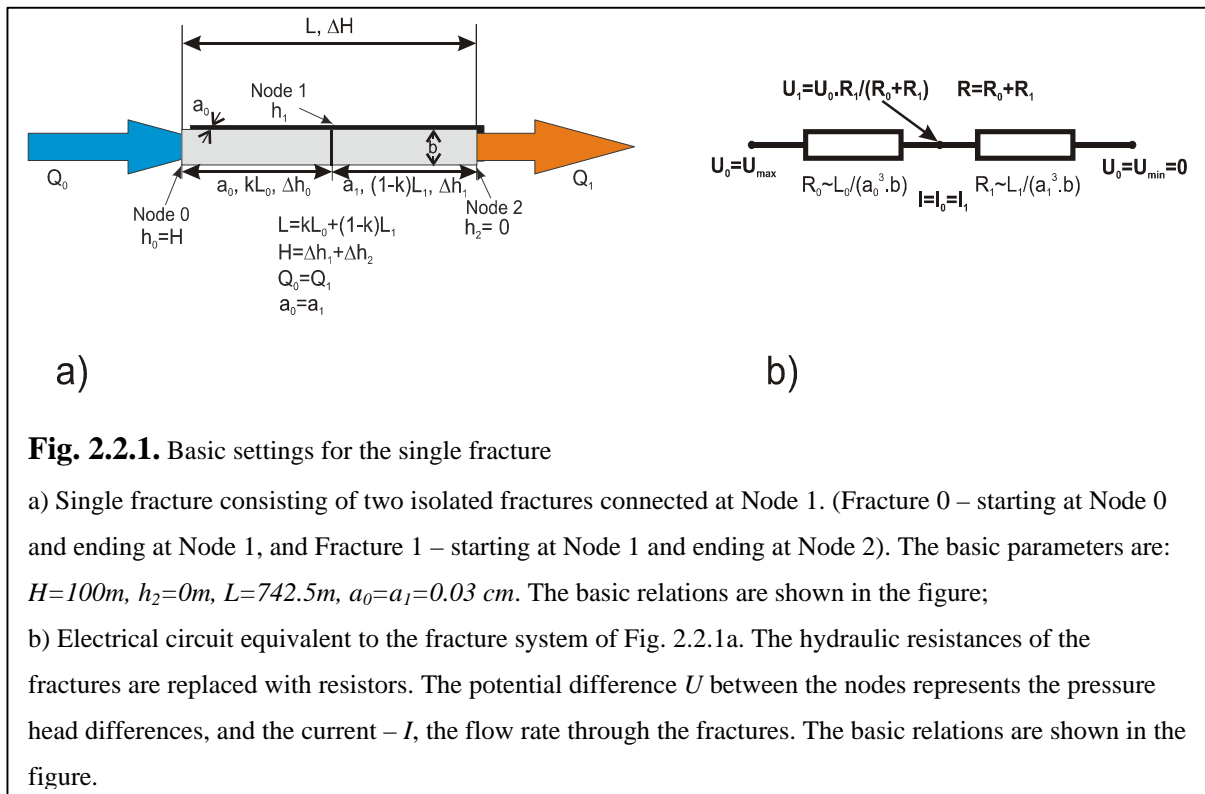


Fig. 2.2.1. Basic settings for the single fracture

a) Single fracture consisting of two isolated fractures connected at Node 1. (Fracture 0 – starting at Node 0 and ending at Node 1, and Fracture 1 – starting at Node 1 and ending at Node 2). The basic parameters are:

$H=100m$, $h_2=0m$, $L=742.5m$, $a_0=a_1=0.03\text{ cm}$. The basic relations are shown in the figure;

b) Electrical circuit equivalent to the fracture system of Fig. 2.2.1a. The hydraulic resistances of the fractures are replaced with resistors. The potential difference U between the nodes represents the pressure head differences, and the current – I , the flow rate through the fractures. The basic relations are shown in the figure.

The single fracture used for our study is represented in Fig. 2.2.1a. It has the same parameters and boundary conditions as the wide fracture from the previous part of this chapter. These are listed in Table 2.2.1. The input Node is Node 0, and the output one is Node 2. We need one more node for the exchange of flow along the length of the fracture. Therefore Node 1 is introduced. It splits the initial conduit into two parts with the same initial aperture widths $a_0 = a_1 = 0.03\text{ cm}$. If no flow is exchanged through Node 1, the system remains unaffected.

We introduce the parameter $0 < k < 1$. Varying its value, we are able to move the

Hydrological parameters	Value	Units
Length of the fracture (Node 0 to Node 2) – $L=L_0+L_1$	742.5	Meters
Number of horizontal sub fractures	2	-
Head on the input side	100	Meters
Head on the output side	0	Meters
Initial aperture width of the single fracture $a_0=a_1$	0.03	Centimeters
Initial width of the fractures – b_0	1	Meter
Chemical parameters		
Ca concentration of the inflowing water	0	mol/cm ³
Equilibrium concentration with respect to Ca	2e-6	mol/cm ³
Temperature of the water	10	°C

Table 2.2.1. Basic geometrical parameters and boundary conditions for the single fracture represented on Fig. 2.2.1.

exchange node along the fracture. The length of Fracture 0 is then defined by $L_0 = k \cdot L$. The length of Fracture 1 is $L_1 = (1-k)L$. In this way the total length $L=L_0+L_1$ is kept constant and only the position of the Node 1 is varied.

The electrical equivalent of the hydrological set up from Fig. 2.2.1a is depicted in Fig. 2.2.1b. The resistors R_0 and R_1 have the same numerical value as the hydraulic resistances of Fractures 0 and 1. As already shown in the introductory part the hydraulic resistance of a fracture is given as (Beek and Muttzall, 1975):

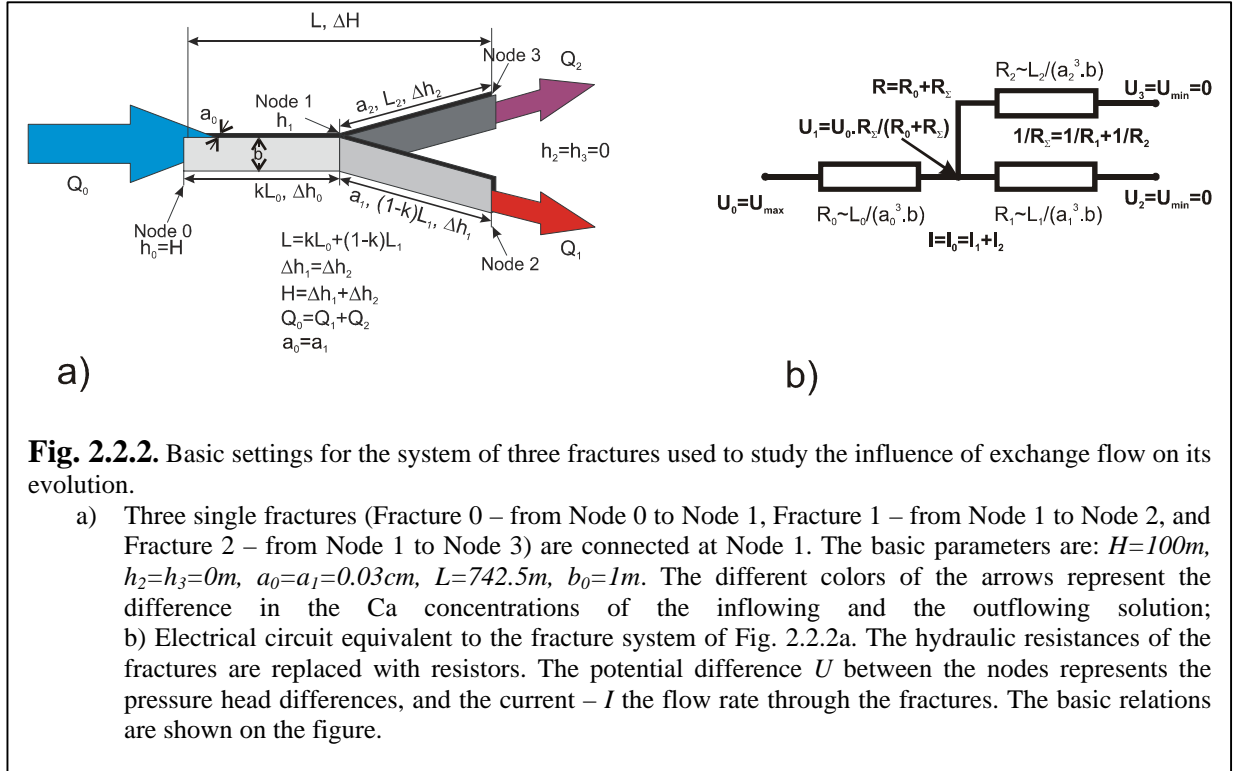
$$R(t) = \frac{12\mathbf{h}}{\mathbf{r}g} \frac{L}{a^3(t)b(t)M(t)} \quad (2.2.1.),$$

Where \mathbf{h} is the dynamic viscosity [g/cm s], \mathbf{r} is the density [g/cm³], a is the aperture width [cm], b is the width [cm], L is the length of the fracture [cm], M is a geometrical factor defined as

$$M = 0.6 - 0.3a/b \text{ - ellipsoidal shape and}$$

$$M = 1 - 0.6a/b \text{ - rectangular shape.}$$

This is all we need to describe the single fracture from Fig. 2.2.1a. But we will use these results only as references and for comparison with the case, where exchange flow through Node 1 is allowed. The set up is represented by Fig. 2.2.2a. Three fractures are



connected at Node 1. The parameters of Fracture 0 and Fracture 1 are the same as the ones from Fig. 2.2.1a. The settings of the third fracture – Fracture 2, are varied. Therefore we need to introduce two more parameters. These are $0 < m < \infty$ and $0 < f < \infty$. The first one is used to define by mL the length of Fracture 2 - $L_2 = m \cdot L$. The second one is used to relate its initial aperture width a_2 to a_0 - $a_2 = f \cdot a_0$. The boundary conditions are as follows:

1. Constant head $H=100m$ at the entrance node of fracture 0 (node 0);
2. Constant head $h_2=h_3=0m$ at the exit nodes of fractures 1 and 2 (nodes 2, 3);
3. The initial aperture widths of fractures 0 and 1 are the same, $a_0=a_1=0.03cm$. The initial aperture width a_2 of Fracture 2 is defined as $a_2 = f \cdot a_1$, where $f \geq 0$. Dissolution is neglected along Fracture 2 and therefore the value of a_2 remains unchanged until the end of the simulations – $a_2(t)=const$;
4. All fractures have the same width $b_0=b_1=b_2$;
5. The lengths of the fractures are defined as follows:

Fracture 0 – $L_0 = k \cdot L$, where $L = L_0 + L_1$, $0 < k < 1$;

Fracture 1 - $L_1 = (1 - k) \cdot L$;

Fracture 2 – $L_2 = m \cdot L$, where $m \geq 0$.
6. The Ca concentration of the inflowing water is $c_{in}=0 mol/cm^3$.
7. The equilibrium concentration with respect to calcite is $c_{eq}=2e-6 mol/cm^3$.

We will compare the evolution of this system with the evolution of the single fracture depicted in Fig. 2.2.1a.

The electrical circuit, equivalent to the setup of Fig. 2.2.2a is depicted in Fig. 2.2.2b. The differences between the initial situations of both scenarios – the isolated one from Fig. 2.2.1a and the exchange one (Fig. 2.2.2a) – are easy to see. In this case we have a group of two parallel resistors (R_1 and R_2) connected with R_0 at Node 1. The effective resistance connected to R_0 is not equal to R_1 anymore but is given by the equation:

$$R_{\Sigma}(t) = \frac{R_1(t) \cdot R_2}{R_1(t) + R_2}, \quad (2.2.2.)$$

If the resistance R_2 is infinitely large, then the circuit is equivalent to the one from Fig. 2.2.1b. ($R_{\Sigma} \rightarrow R_1$). This is also true for the hydraulic resistance of Fracture 2. If it has an infinite large value ($f \rightarrow 0$, see Eq. 2.2.1.), then the system represented by Fig. 2.2.1a is the same as the one of Fig. 2.2.2a, and behaves like a single fracture. But what happens in the case when R_2 is smaller than infinity? According to Eq. 2.2.2 R_{Σ} will be smaller than the smaller of both resistances R_1 and R_2 and, consequently, the value of the effective resistance connected to R_0 will be smaller. Actually this is the reason, which causes the differences in the evolution of both systems (Fig. 2.2.1a, and Fig. 2.2.2a.). We will come back to this during the discussion in the next subsection.

There is one point, which should be clarified from the very beginning. The connection of the end nodes of Fracture 1 and Fracture 2 to the same pressure head means that we will study only the cases where the flow is directed from Fracture 0 into Fractures 1 and 2. There will be no discussion for the situation where inflow is coming from two different locations and mixes in the node. This case is discussed in detail by (Gabrovsek, 2000, and Gabrovsek and Dreybrodt, 2000). Our interest will be concentrated on the cases where the amount of flow leaving the system of Fig. 2.2.1a through Node 1 is varied because of the variation of the parameters f , m and k .

Before the presentation of the results, it is useful to analyze the initial situation. Let us discuss the differences in both systems (see Fig. 2.2.1a, b and Fig. 2.2.2a, b). We define the setup depicted in Fig. 2.2.1 as Case I and the setup from Fig. 2.2.2 is Case II. All variables having upper index I are related to the single fracture situation and the ones with index II, to the scenario from Fig. 2.2.2. The boundary conditions for both scenarios are the same. They remain unchanged at any moment of the simulations.

The continuity equation for Node i is:

$$\sum Q_{in}(i) = \sum Q_{out}(i) \quad (2.2.3.)$$

We are interested of the value of the pressure head at moment $t=0$ at Node 1.

Eq. 2.2.3 for this node is:

$$Q_0^I = Q_1^I \quad (2.2.4.)$$

and

$$Q_0^{II} = Q_1^{II} + Q_2^{II} \quad (2.2.5.)$$

We know that $Q = \frac{\Delta h}{R}$ (Beek and Muttzall, 1975), where R is defined by Eq. 2.2.1.

$$\Rightarrow \frac{\Delta h_0^I}{R_0^I} = \frac{\Delta h_1^I}{R_1^I} \quad (2.2.6.)$$

and

$$\frac{\Delta h_0^{II}}{R_0^{II}} = \frac{\Delta h_1^{II}}{R_1^{II}} + \frac{\Delta h_2^{II}}{R_2^{II}} \quad (2.2.7.)$$

This enables us to find the value of h at Node 1.

$$\Delta h_1^I = H - H \cdot \frac{R_0^I}{R_0^I + R_1^I}; \quad (2.2.8a)$$

$$h_1^I = H \cdot \frac{R_1^I}{R_0^I + R_1^I} \quad (2.2.8b)$$

and

$$\Delta h_1^{II} = H - H \cdot \frac{R_0^{II}}{R_0^{II} + R_\Sigma} \quad (2.2.9a)$$

$$h_1^{II} = H \cdot \frac{R_\Sigma}{R_0^{II} + R_\Sigma} \quad (2.2.9b)$$

See (Fig. 2.2.1a, Fig. 2.2.2a and Eq. 2.2.2.).

According to our initial conditions, $R_0^I = R_1^I = R_0^{II} = R_1^{II}$ at time $t=0$. This means that the difference in the initial values of h_1^I and h_1^{II} is only due to the differences in the resistances R_1 and R_Σ . As already discussed $R_\Sigma \leq R_1^{II}$. Therefore, $h_1^{II} \leq h_1^I$ in any case at the initial moment $t=0$. The consequence is that the flow rate through R_0^I is smaller than the flow rate through R_0^{II} at $t=0$. At the same time the amount of flow through R_1^I is higher than the one through R_1^{II} at moment $t=0$. If there would be no dissolution along the fractures, this situation would remain unchanged.

Our next goal will be to find out the differences in the initial dissolution rates along Fractures 0 and 1 for both scenarios. As already stated, the dissolution rate along Fracture 2 is set to 0 mol/(cm²s).

We assume that the rates along each fracture are constant and their value at $t=0$ is that at the end of each fracture, which can be calculated analytically. This means even widening from the very beginning, such that the walls remain parallel to each other during the entire evolution. Although the dissolution rates change in time, by this way we are able to obtain an analytical solution of the evolution of fracture aperture widths (Gabrovsek, 2000) and an upper limit of the breakthrough time.

The dissolution rates at the entrances of Fracture 0 for both cases are the same. What is the situation at their exits – Node 1, assuming that the length kL of Fracture 1 $\gg x_s$, the place along the fracture, where the dissolution kinetics switches from a linear to a nonlinear rate law (Gabrovsek 2000)?

$$F(kL, t) = F(x_s) \left(1 + \frac{kL}{I_n(x_s)} \right)^{\frac{n}{1-n}} \quad (2.2.10.)$$

the penetration length I is given by:

$$I_n(x_s) = \frac{Q(t) \cdot c_{eq} \left(1 - \frac{c_s}{c_{eq}} \right)^{1-n}}{Pk_n(n-1)} \quad (2.2.11.)$$

$Q(t)$ is the flow through Fracture 0, P is the perimeter of the fracture's cross-section, c_s is the switch concentration, c_{eq} is the equilibrium concentration with respect to calcite, and k_n is the higher order kinetics constant (see the introduction) (Gabrovsek, 2000).

Applying these equations to our scenarios we come to the conclusion, that the dissolution rate at the exit of Fracture 0 for Case II is higher than the dissolution rate at the exit of Fracture 0 for Case I, because $Q_0^{II} > Q_0^I$. This means that Fracture 0 will start to widen with a higher rate than the one from the isolated case. The resistances of the fractures change in time and consequently the pressure head at Node 1 will change also (see Eqs. 2.2.8b and 2.2.9b).

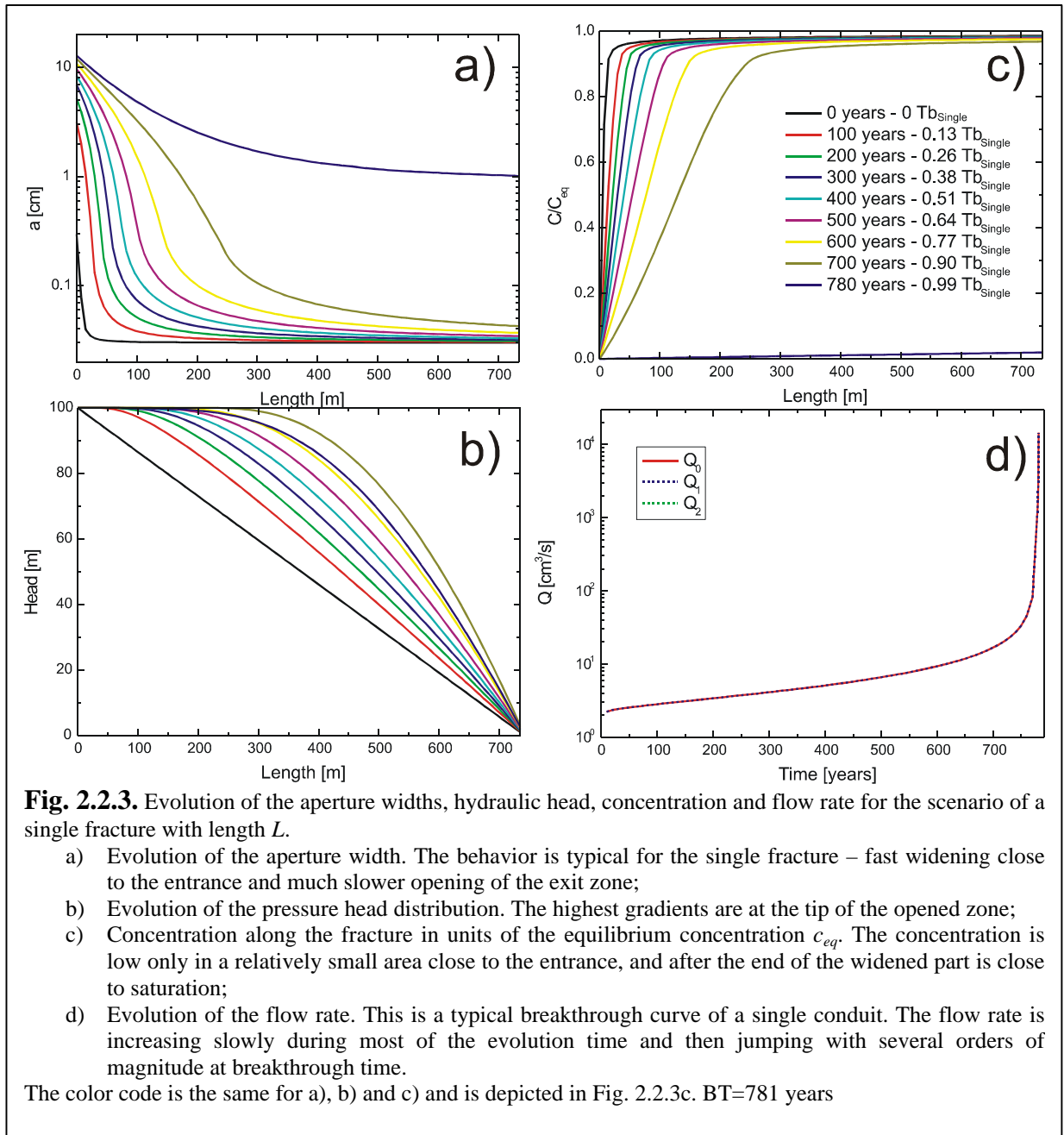
At the same time the situation for Fracture 1 is more complicated. The flow rate through it in Case II is initially smaller than the one for Case I. Furthermore, the water entering Fracture 1 is coming from the exit of Fracture 0. But the dissolution rates there are different for Case I and Case II in contrast to the dissolution at the input of Fracture 0. By this way, the input concentration at the entrance of fracture 1 is also different. Its value can be obtained by solving the rate equation for c :

$$F_n(kL, t) = k_n \left(1 - \frac{c}{c_{eq}}\right)^n \quad (2.2.12.)$$

This means that the input concentration for Fracture 1 in case II is lower than the one in case I. It is possible to calculate whether this is enough to guarantee higher rates at the exit for case II, but because of the changing conditions at Node 1 this information will not help us too much. In other words, it looks quite difficult to get analytical solutions to these problems.

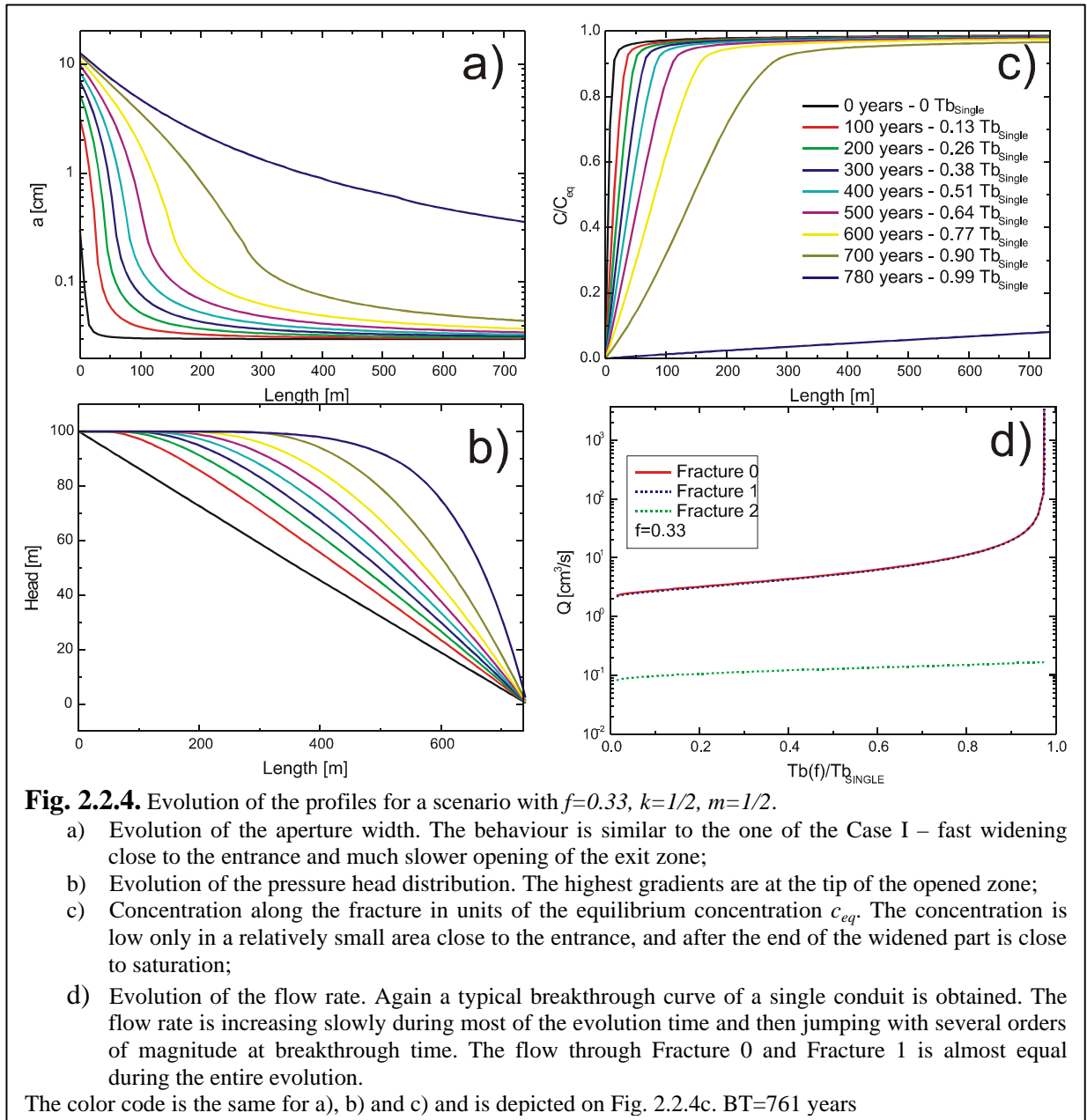
So, we have to try to find some other way. The first one is to use our model and find numerical results. The second one is to continue to simplify the problem, with the help of further approximations. We will use both options and will compare the results at the end.

2.2.2 Numerical results



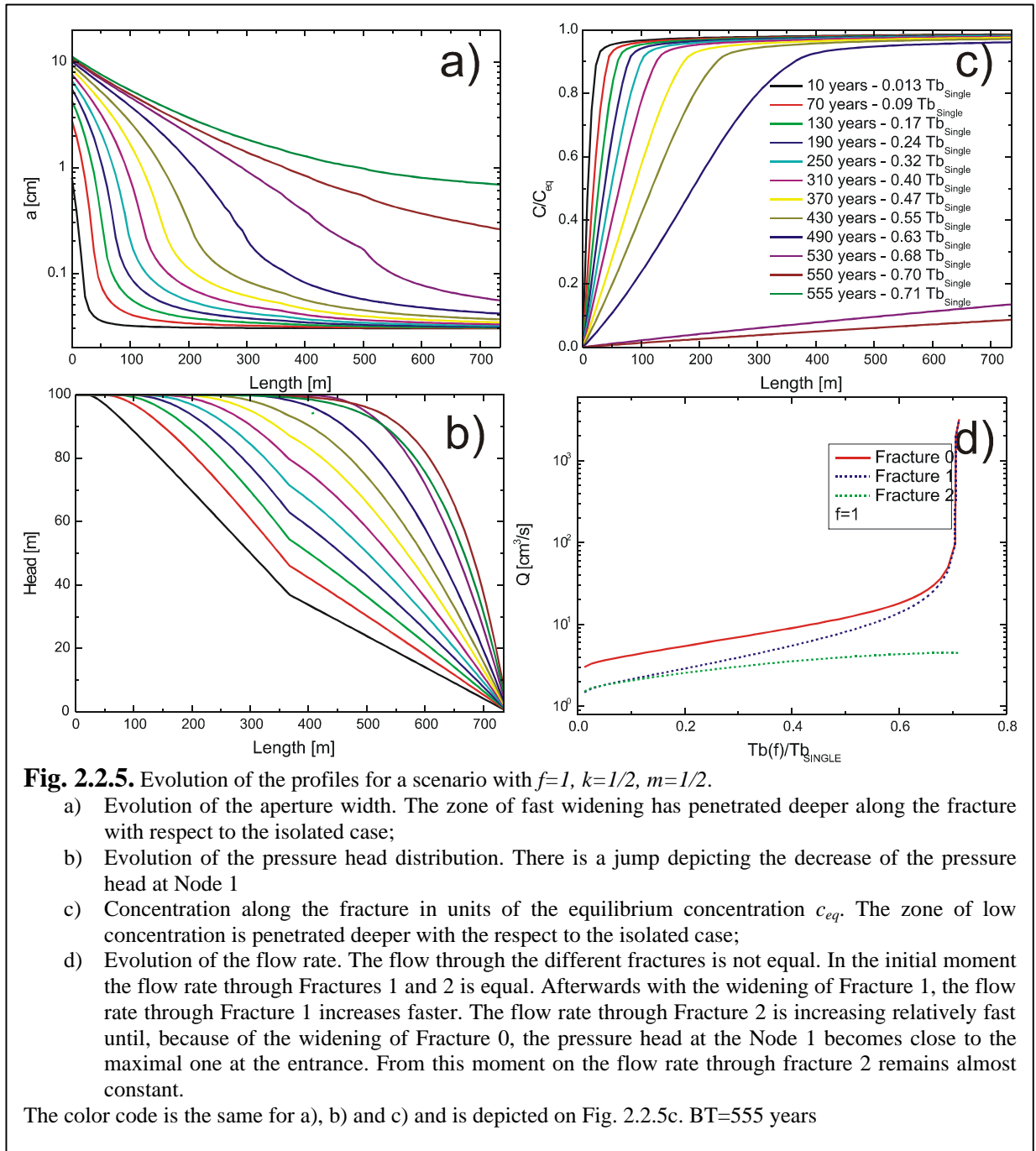
Let us start with the numerical simulations. The model setup was already discussed in 2.2.1. The idea is to compare the evolution of the single fracture case I with the exchange scenario – case II.

The development of the single fracture with the selected boundary conditions is already well known. It was discussed in the previous part of this chapter. We will directly present the results obtained there. Fig. 2.2.3 depicts the profiles of the aperture widths (see Fig. 2.2.1a), the pressure head distribution, the concentration profile, and the flow rates. The colors represent time. It is depicted in years. The resistance of Fracture 2 is infinitely large for this scenario.



Therefore the flow rates through Fracture 0 and Fracture 1 are equal (Fig. 2.2.3d). They are limited by the constriction at the exit of Fracture 1 (see Fig. 2.2.3a). The pressure head at $t=0$ is decreasing linearly along the conduit and then is changing with the change of the aperture width. The main head loss per length is at the tip of the widened zone (see Fig. 2.2.3b). The concentration profiles are also typical for the single fracture case (see Fig. 2.2.3c). Because of the slow growth of the exit part of Fracture 1, the flow rate remains low for most of the evolution time. The solution entering the fracture is attaining high Ca concentrations close to the entrance. Shortly before breakthrough, when the rate of widening of the exit is higher, the fresh solution starts to penetrate deeper into the channel. After the breakthrough (at 761 years), the concentration becomes low along the entire length of the fracture.

We have performed two series of calculations for Case II – the exchange case. During the first run, the values of k , and m are fixed at $k=1/2$ and $m=1/2$. This means that the position



of Node 1 (see Fig. 2.2.2a) is such that $L_0=L_1=L_2$. The value of f is varied in the range from f almost equal to zero (this scenario is similar to the isolated Case I), to $f \rightarrow \infty$.

We start the discussion with the case $f=0.33$. Fig. 2.2.4a-d depicts the profiles for the aperture width (Fig. 2.2.4a), pressure head (2.2.4b), and concentration with respect to c_{eq} (Fig 2.2.4c), and the evolution of the flow rate (Fig. 2.2.4d). The breakthrough time in this case is only 20 years lower than the one for Case I. Because of this, one shouldn't expect big changes in the profiles. This is exactly what can be seen in the figures. Profiles look almost the same. There is only one small detail, which is actually the reason for the deviation of the breakthrough time (see Fig. 2.2.4d). The flow rate through Fracture 1 is a little bit lower than the one through Fracture 0. The reason for this is the presence of Fracture 2. Its resistance is so high that it

cannot influence too much the evolution of the system, but even in this case we observe a reduction in the breakthrough time. We expect that this effect will become stronger with increasing value of f .

We increase the value of f to $f=1$. This is a symmetrical scenario, because the initial values of the aperture widths are the same for all fractures, and their lengths also. Of course,

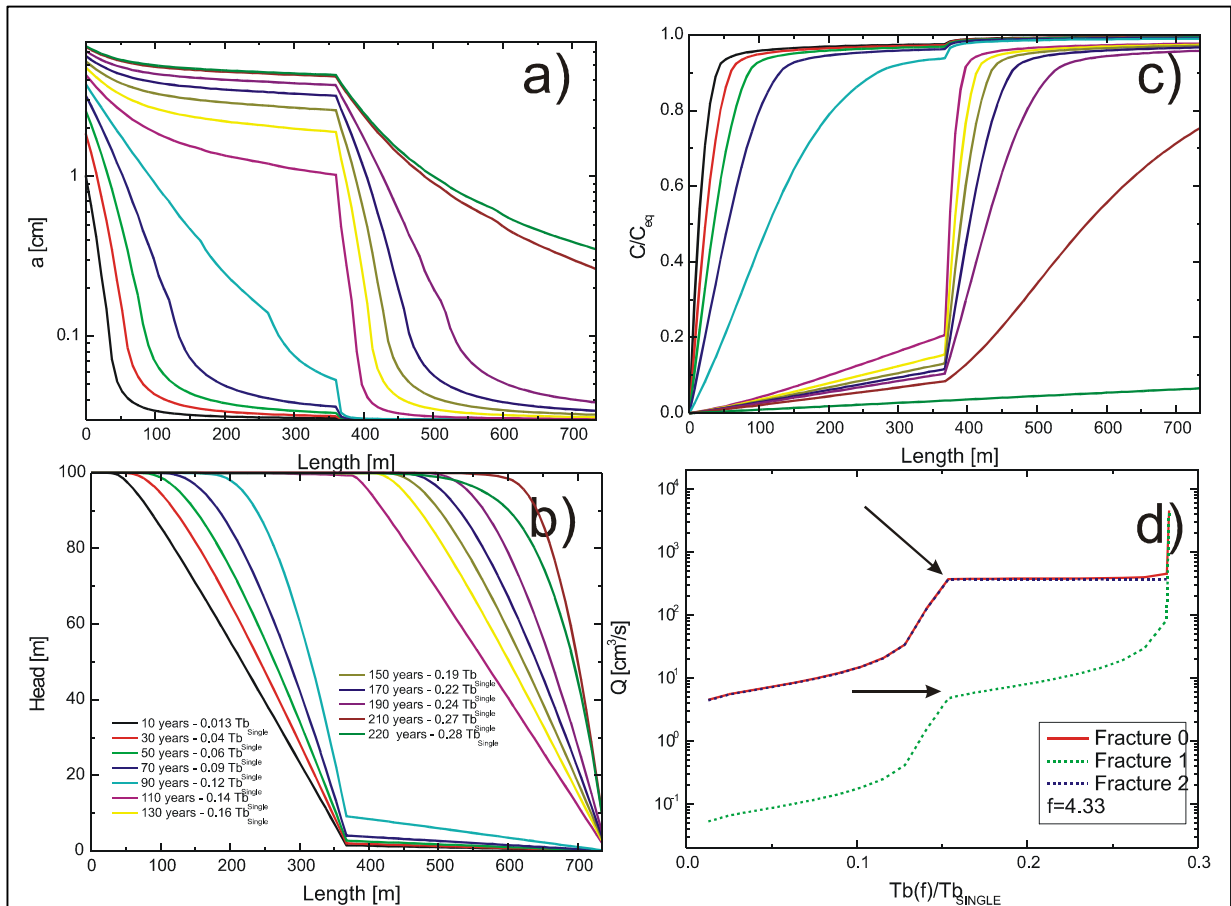


Fig. 2.2.6. Evolution of the profiles for a scenario with $f=4.33$, $k=1/2$, $m=1/2$.

- Evolution of the aperture width. Fracture 0 grows independently of Fracture 1 until the moment of breakthrough at 90 years. Fracture 1 remains unchanged during this period. After the breakthrough event of Fracture 0, the development of Fracture 1 starts under similar conditions – highest possible hydraulic gradient, and low input concentration;
- Evolution of the pressure head distribution. The pressure head distribution resembles the evolution of two fractures – shifted in time. The second one starts to evolve after the jump in the value of the head at Node 1 – 90 years.
- Concentration along the fracture with respect to the equilibrium concentration c_{eq} . The evolution of the concentration profiles also shows two independently evolving fractures;
- Evolution of the flow rate. Because of the high initial aperture width of fracture 2, the initial flow through Fracture 0 is also high. The contribution from the flow through Fracture 1 is negligible. After the breakthrough of Fracture 0, the flow through Fracture 2 remains constant. The flow through Fracture 0 remains close to it until the moment of breakthrough of Fracture 1, which marks the breakthrough for the whole system.

The color code is the same for a), b) and c) and is depicted in Fig. 2.2.6b. BT=221 years

The arrows indicate restricted breakthrough of Fracture 0, where the flow rates are limited by the finite resistance of Fractures 1 and 2.

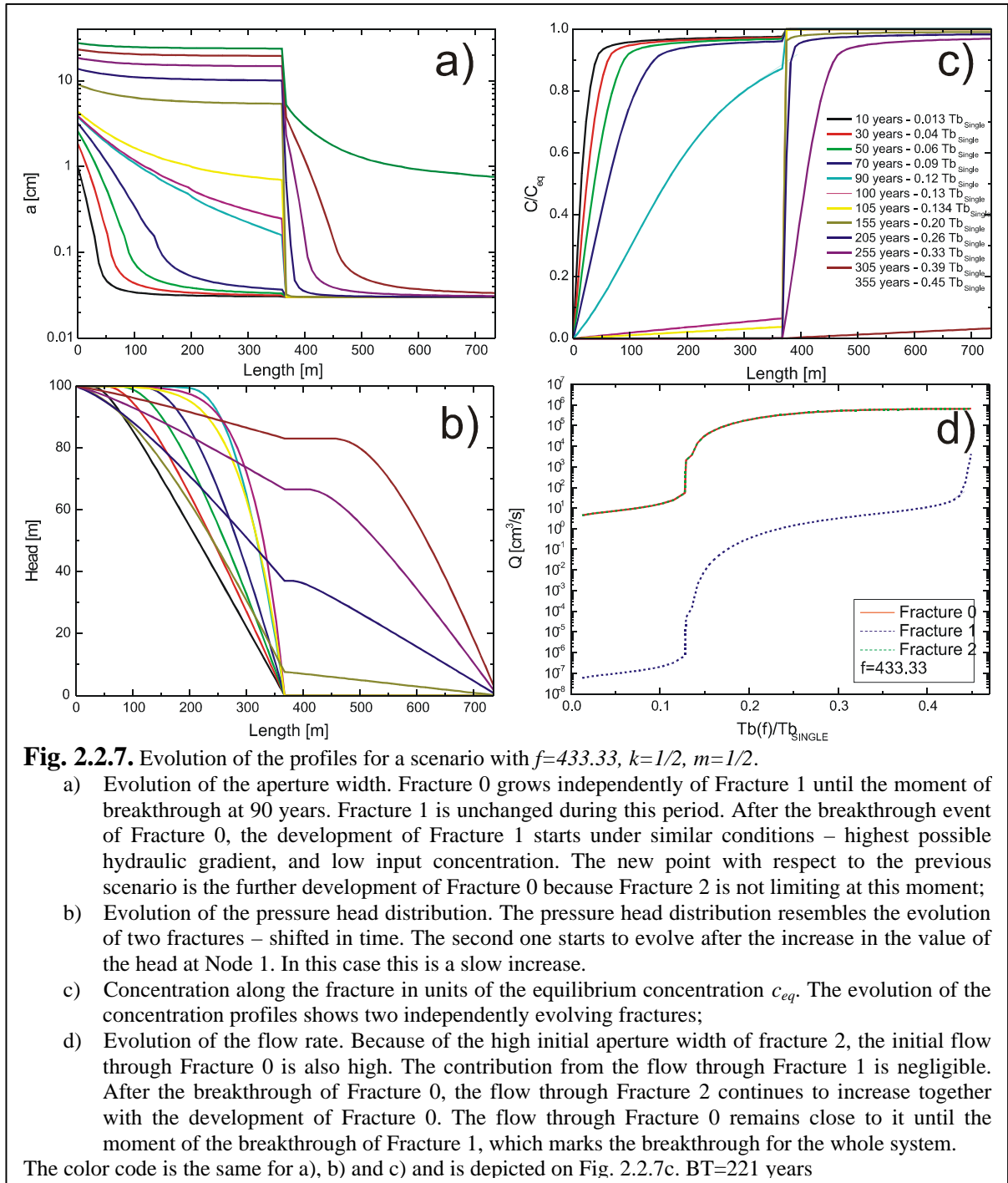
this is true only for the beginning of the simulation. Afterwards, because of the dissolution along Fracture 0 and Fracture 1, their resistances decrease, while the one of Fracture 2 remains

constant. This is easy to see on Fig. 2.2.5d. It depicts the evolution of the flow rates along the fractures. The evolution of the aperture widths is depicted in Fig. 2.2.5a. The difference with respect to the already discussed cases is that the widening of Fracture 0 is more effective. The opening zone progresses faster towards the exit. The differences in the pressure head distribution are even easier to note. There is a clearly visible change at Node 1 (see Fig.2.2.5b). It shows that the presence of Fracture 2 is increasing the gradient along Fracture 0. The resistance of Fracture 2 is already sufficiently low and the flow rate through it is comparable to the flow rate through Fracture 1 (see Fig. 2.2.5d). The profiles of the concentration are depicted in Fig. 2.2.5c. Because of the deeper penetration of the widened zone (see Fig. 2.2.5a) and the higher flow rate through Fracture 0, the zone of lower concentration has also penetrated deeper along the fracture. The reduction of breakthrough time for this scenario is already more than 300 years.

As we have already seen the influence of Fracture 2 is quite important. Until this moment we have worked with values of f smaller than or equal to 1. In other words, the initial aperture width of Fracture 2 was always smaller or equal to the one of the single fracture. Our next set of experiments will study the behavior of the system at high values of f .

We start with $f=4.33$. The results are depicted in Fig. 2.2.6a-d. The influence of Fracture 2 on the pressure head at node 1 is significant (see Fig. 2.2.6b). Actually, the value there is close to the minimal value of the exit boundary condition. This is the reason for the separate evolution of Fractures 0 and 1. There is almost no change in the aperture widths of Fracture 1 during the first 90 years of evolution of Fracture 0 (before breakthrough) (see Fig. 2.2.6a.). This evolution is fast (90 years). The reason is the low input concentration and the high hydraulic gradient along the fracture. The jump at 90 years marks the breakthrough of Fracture 0. This is also visible from the concentration profiles (Fig. 2.2.6c), the pressure head distribution (Fig. 2.2.6b), and the jump in the flow rates in Fig. 2.2.6d. After this, the value of the pressure head at Node 1, changes from 0 m to 100 m – the maximal possible value. This is the moment of the beginning of the evolution of Fracture 1. The flow through Fracture 2 remains constant, because there is no dissolution along this conduit. This will also limit the fast growth of the flow rate through Fracture 0. The evolution of Fracture 1 takes roughly the same time, and the second breakthrough event for the system is depicted by the abrupt changes in the profiles (see Fig. 2.2.6 a-d) at 221 years.

As a last example we increase f to 433.33. The results are depicted on Fig. 2.2.7a-d. This case is surprisingly interesting. Normally one should expect that a further increase of the initial aperture width would result in further decrease of the breakthrough time of the system.



This is not the case. The breakthrough time increases by almost 100 years. This “simple” system of three fractures (see Fig. 2.2.2a) is actually not so simple. Let us have a look at the profiles.

They are depicted on Fig. 2.2.7a-d. The first impression is that the only change is for the pressure head distribution (Fig. 2.2.7b), but a closer look shows that the aperture width of Fracture 0 after its local breakthrough event is several times larger than the one for the previous simulation. This is easy to explain. The limitations for further evolution of Fracture 0, for the previous scenario, are Fractures 2 and 1. Now, in this case Fracture 2 is so large, that

actually it allows further considerable opening of Fracture 0 even before the breakthrough of Fracture 1 and at the same time does not allow a fast jump of the pressure head to its maximal value. The increase of the pressure head at Node 1 starts at the moment when the aperture width of Fracture 0 becomes close to the one of Fracture 2. This is also visible from the profiles of the flow rate evolution (see Fig. 2.2.7d). After the breakthrough of Fracture 0, the curve for the flow through it is not flat. It continues to grow under turbulent flow conditions. Close to the moment when the aperture width of Fracture 0 becomes similar to the one of Fracture 2 (13 cm), (see Fig. 2.2.7a), the pressure head at Node 1 starts to increase, but slowly, not like the jumping change of the previous scenario. This is the reason for a delayed development of Fracture 1 in comparison to the previous case.

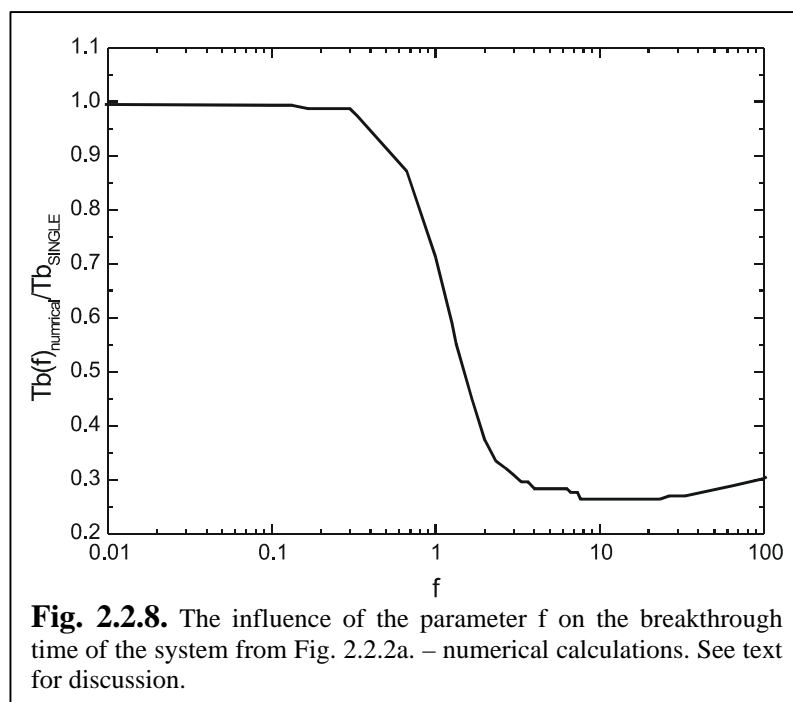


Fig. 2.2.8 depicts the influence of the parameter f on the breakthrough time of the system.

The main result is that for all values of f , the breakthrough time of the system is reduced. The reason for the minimum of the curve at values of f about 10 is that with the initial conditions for Fractures 0 and 1, the breakthrough event of Fracture

0 happens when its aperture width is still smaller than the one of Fracture 2. As a consequence the conditions for the development of Fracture 1 are not the perfect ones (maximal gradient, and low input concentration). If the breakthrough event for Fracture 0 would happen at values of the aperture width already larger or close to a_2 then the pressure head at Node 1 obtains its maximal possible value immediately after the breakthrough event of Fracture 0. These are the best conditions for Fracture 1 to develop, and marks the zone of the minimum in Fig. 2.2.8 (see Fig. 2.2.6). Afterwards, with decreasing f the breakthrough times increase and reach a maximal value at $f \rightarrow 0$ - the isolated fracture case.

To study the influence of the position of the junction Fig. 2.2.9 depicts the influence of the parameter k on the breakthrough time of the system. The value of f is also varied.

We select several values for f , representing interesting regions of the breakthrough curve from Fig. 2.2.8. These

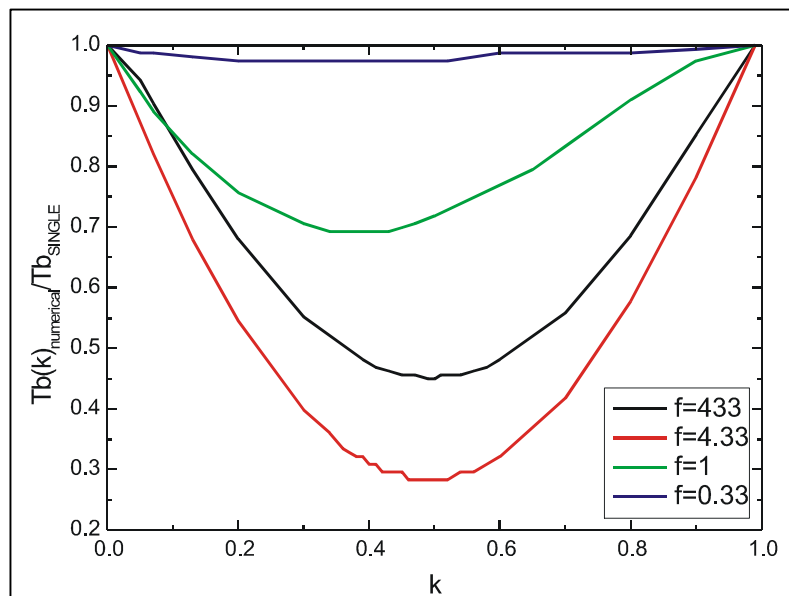


Fig. 2.2.9. Influence of the position of the junction to the evolution of the system.

The minimum of the curves is changing with the change of the f parameter. For values of f much greater than 1, the minimum in the breakthrough time is when the junction is in the middle of the single fracture. With the decrease of f , the minimum is moving in the direction towards the entrance of the fracture.

are: $f=0.33$, $f=1$, $f=4.33$, $f=433.33$. The evolution of the system with these values of f and $m=k=1/2$ were already discussed in details. We change the value of the parameter k . This corresponds to a movement of the position of Node 1 along the fracture. It is clear that the maximum of the breakthrough time will be at values of $k = 0$ or 1 . In these cases the system develops like a single conduit. With the movement of the junction along

the fracture, the breakthrough times decrease. The position of the minimum depends on the value of f and m . For large values of f and $m=1/2$ the minimum is $k=1/2$. This is clear, because in these cases both fractures develop independently of each other, and the breakthrough time of the system will depend only of the lengths of Fractures 0 and 1. The minimum in this case is when $L_0=L_1$, which corresponds to $k=1/2$.

2.2.3. Discussion

In the following we will discuss a situation as in Fig. 2.2.2, where all initial fracture aperture widths are identical ($f=1$) and $k=m=1/2$. Depending on the value of f two regions of the impact of exchange flow can be envisaged. For small $f \ll 1$ exchange flow is small with respect to the initial flow through Fractures 0 and 1, because the resistance of Fracture 2 is high. Note that this resistance increases with the third power of f . In the extreme case $f=0$ the system behaves like an isolated fracture. When the resistances of all three fractures are of similar magnitude, i.e. $f=1$, then the existence of exchange flow acts as positive perturbation to enhance breakthrough times. This is the situation we have encountered in the system of Fig.

2.2.4. ($f=0.33$) and 2.2.5 ($f=1$), where slight reduction of breakthrough times have been observed.

Now we turn to the case $f>1$. If the resistance of Fracture 2 is much smaller than that of Fracture 0, the latter fracture experiences a high drop of the hydraulic head. Under these conditions it behaves like an isolated fracture with a head drop close to H and experiences breakthrough accordingly. After breakthrough the head at node 1 becomes close to H . During this time Fracture 1 has increased its aperture width slightly by Δa_1 according to the small head, which has acted along it. After breakthrough it experiences the full hydraulic head and breakthrough occurs like for an isolated fracture with aperture width $(a_1 + \Delta a_1)$. The total breakthrough time for the system is just the sum of these of the two subsequent events. Such scenarios are shown by Fig. 2.2.6 ($f=4.33$) and Fig. 2.2.7 ($f=433.33$). In both cases the total breakthrough times are equal since R_2 is larger by a factor of 81 or a factor of $81 \cdot 10^6$, respectively. In other words, in both cases $R_2 \ll R_0, R_1$.

This behavior is also reflected by Fig. 2.2.8, which gives the dependence of the total breakthrough time on f . For $f>2$ we find an almost constant but significant reduction of total breakthrough time. For $f<0.33$ breakthrough times are those of the isolated series of Fracture 0 and Fracture 1. The intermediate range of perturbation is between $0.33 < f < 2$.

2.2.4. Analytical approximation

In the following we will give an analytical estimation for the region with $f>2$ to find the dependence of breakthrough time on the position of Fracture 2, i.e. k , and also the parameter m . We calculate the breakthrough time of Fracture 1. Assuming that the dissolution rates in Fracture 1 are even along its entire length, equal to the rates at the exit, we find the aperture width of this fracture after the breakthrough of Fracture 0. Using this aperture width we calculate the breakthrough time for the subsequent breakthrough of Fracture 1.

We will not give details of the straight but tedious algebra. The result is:

$$T_B^{analytical} = \left(\left(k \left(k + \frac{(1-k)\frac{m}{f^3}}{(1-k) + \frac{m}{f^3}} \right) \right)^{\frac{n}{n-1}} + \left(\frac{(1-k)^2}{v^3} \right)^{\frac{n}{n-1}} \right) \cdot T_B^{single} \quad (2.2.13),$$

where

$$v = \left(\left(1 - \frac{k \frac{m}{f^3}}{k \frac{m}{f^3} + (1-k)^2 + (1-k) \frac{m}{f^3}} \right)^{\frac{n}{n-1}} \right)^{\frac{1-n}{2n+1}} \quad (2.2.14)$$

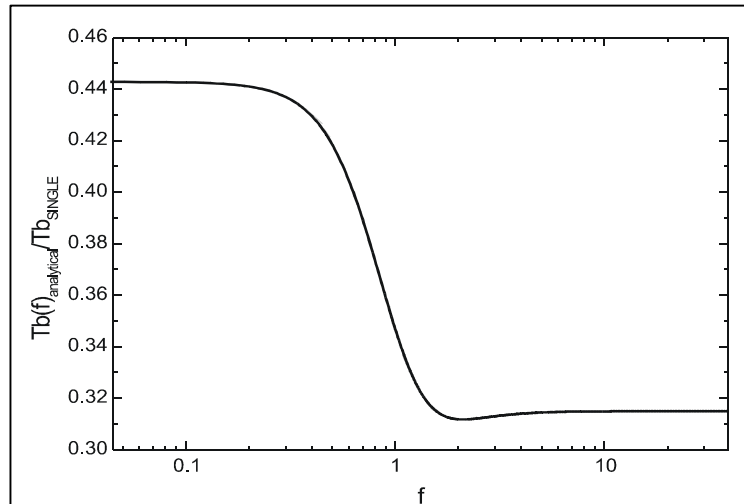


Fig. 2.2.10. Analytical approximation for the breakthrough time of the system presented on Fig. 2.2.2 in dependence on f . For values of $f > 1$, the behaviour is similar to the results of the numerical calculations. For values of $f < 1$, the approximation is unrealistic.

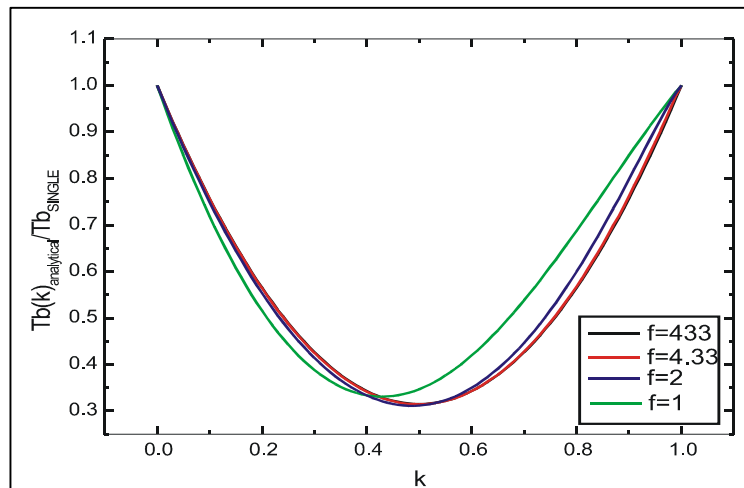


Fig. 2.2.11. The influence of the position of the junction to the evolution of the system. In this case the value of T_b for the system from Fig. 2.2.2a is estimated with the help of Eq. 2.2.13.

Fig. 2.2.10 depicts the influence of f on the calculated breakthrough time of the system. The values of k and m are fixed at $\frac{1}{2}$. One can see that the trend of the breakthrough time dependence is similar to the one found by the numerical calculations. Even the minimum is there. Of course, the breakthrough time found by Eq. 2.2.13 is extremely underestimated for values of $f < 1$. This is the

reason for the value of $\frac{T_B^{analytical}}{T_B^{single}} = 0.46$ for f approaching zero.

Fig. 2.2.11 depicts the influence of the calculated breakthrough time on the position of Node 1 along the fracture. Again, as in the numerical case, the dependence is calculated for different values of $f=0.33, 1, 4.33$ and 433.33 . The value of m is fixed at $\frac{1}{2}$.

One can see that also for this calculation the curves show behavior similar to the one found by the numerical calculations. The minimum of the curves is moving towards the entrance of the fracture, with decreasing f . We also observe the trend that the minimum of the breakthrough time shifts towards the entrance with decreasing f , whereas its value increases. In a few words. The approximation cannot be used to estimate the real decrease of the

breakthrough time of the system exchanging flow with another system, with respect to the breakthrough time of an isolated one for values of f lower than 1. But on the other hand it can be used to get an idea about the influence of the breakthrough time of the basic parameters defining the exchange flow.

2.2.5 Conclusion

As a short summary we will go through the results once again.

The influence of the exchange flow on the evolution of a system of three fractures (see Fig. 2.2.2b) was discussed in details. In any case, when the exchange of flow is in a direction outside of the studied system, it will decrease the time needed for the evolution of this system. The decrease is maximal if the exchange flow is large and if the place of the connection with the surrounding environment is close to the center of the studied system.

There are two modes of karstification with respect to the exchange flow. The switch between these is fast and is observed for a relatively narrow interval of the values of f (see Fig. 2.2.8).

If the amount of the exchanged water is low ($f < 1$) then the reduction in the breakthrough time of the system is negligible and there is no considerable influence on the evolution.

The second mode of karstification is observed for values of $f > 1$. Then the amount of the exchanged water is considerable and the evolution of the system is largely affected. The reduction of the breakthrough time is almost by an order of magnitude.

These results confirm the ones obtained for the case of a wide fracture embedded into a net of fine fissures.

3. Karstification below dam sites

The topic of the discussion so far was the early evolution of a karst aquifer under various hydrological boundary conditions. It described how sensitively the aquifer reacts to variations of these parameters. This complex behavior was observed even for the highly idealized scenarios studied in the previous chapter.

Limestone rocks underlay 15 % of the earth's dry ice-free land (Ford and Williams, 1989). A large number of dam sites were constructed successfully in these terrains.

The time scale of the evolution of a karst aquifer under natural boundary conditions – in general low hydraulic gradients - is in the range of ten thousands to several hundred thousands of years. The changes of the aquifer are so slow, that it remains practically unaffected during the life times of generations. Under man made hydraulic boundary conditions, such as dam sites, this does not need to be true. In these cases the process of karstification is accelerated by extremely high hydraulic gradients and comparably short pathways. The evolution time may become comparable with the lifetime of the hydraulic structures (see Eq. 1.21). Underestimating the dynamics of the changes in the aquifer can endanger the function of the construction.

For example the Great Falls Reservoir in the USA showed an increase of leakage from 0.47 m³/s in 1926 to 6.6 m³/s in 1939, and to 12.7 m³/s in 1945, which caused a decrease of its water level by 8.1 m (Milanovic 2000). There are examples of dam sites, whose initial leakage was so high, that they never could be filled to their planned capacity. An interesting case study describing the problems associated with the construction of the Lar Dam in Iran has been published recently (Uromeihy, 2000). It describes the interplay between the man made high hydraulic gradients and the naturally calcite aggressive, water of this region.

As soon as the dam site is filled with water, the boundary conditions of the karst aquifer are changed dramatically. Because of the high hydraulic gradients, the flow rates through the channels and the joints in the soluble rock below the dam increase with respect to the natural situation. Consequently the dissolution rates are enhanced and the changes in the aquifer are considerably faster. Together with the study of the reaction of the dam sites to flooding events, it is necessary also to investigate this process. Techniques can be developed to avoid water losses and to assure the stability of the hydraulic structures.

James and Kirkpatrick (1980) and James (1992) discuss the four major classes of soluble rocks found on dam sites. They describe the risk in terms of potential settlements and leakage paths, caused by dissolution of these materials within the foundation of the dams. Site

investigation procedures and a quantitative basis for the design of safe structures are described and proposed for future use in the engineering design. James (1992) created models based on one-dimensional conduits. His work investigates the enhanced dissolution in limestone and in gypsum terrains and its relation to the failures of dams. James (1992) reports several case histories of failures due to excessive water losses, which he believes are due to dissolution of gypsum.

Palmer (1988) proposes a one-dimensional model of limestone dissolution and concludes that the increase of the water loss of the Great Falls Reservoir, USA, resulted from dissolutional widening of fracture pathways, connecting the bottom of the reservoir to the valley downstream. Palmer (1988) suggests a crude estimation, for hydraulic conditions under which a pathway in limestone with aperture widths of about 0.01 cm would suffer dissolutional widening, leading to significant water losses.

Dreybrodt (1992, 1996) and Dreybrodt and Gabrovsek (2000) confirm these estimations. Their works describe the crucial parameters, determining failure of hydraulic structures. These are the aperture widths of the fractures comprising a percolating pathway, and the hydraulic ratio given by H/L^2 , where H is the height of the impounded water, and L is the length of the pathway from its input at the bottom of the reservoir, to its output. For hydraulic structures with $H/L^2 > 0.2 \text{ m}^{-1}$ water losses of about $0.5 \text{ m}^3\text{s}^{-1}$ can arise within 50 years for a single pathway with an initial aperture width of 0.01 cm and a width of 1m.

These single conduit models neglect the exchange of flow between the single percolating pathways and the surrounding network of fractures. It was already shown in the previous chapter, that this exchange has a strong influence on the evolution of the karst aquifer. Because of the mechanisms discussed there, the evolution is accelerated. Consequently, the estimations, on the values of the crucial parameters derived by the single conduit models can sometimes be misleading. First approaches in avoiding these problems are reported by Bauer et al. (1999). Dreybrodt and Siemers (2000) and Dreybrodt et al. (2001) demonstrate first attempts on two-dimensional modeling, and on a systematical study of the processes governing the evolution of a karst aquifer under the boundary conditions of a dam site. In a recent study, Kaufmann (2003) discussed the effect of mixing corrosion on the evolution of a karst aquifer in an artificial environment.

The topic of this chapter is the process of karstification below dam sites, and the timescales of karstification of short pathways subjected to high hydraulic gradients. We present a more realistic two-dimensional model of a fractured soluble rock, underlying a dam site. We study the evolution of the fracture aperture widths under the action of steep hydraulic gradients

imposed by impounded water. Our aim is to find rough estimations for the dependence of the breakthrough time of the aquifer on different initial boundary conditions. These are the height of impounded water H , the grouting depth G , the average aperture widths a_0 of the fractures extending through the modeled block of soluble rock, the equilibrium concentration c_{eq} of the Ca with respect to calcite, and the initial calcium concentration c_{in} of the inflowing water.

3.1. Basic settings

3.1.1. Geological settings

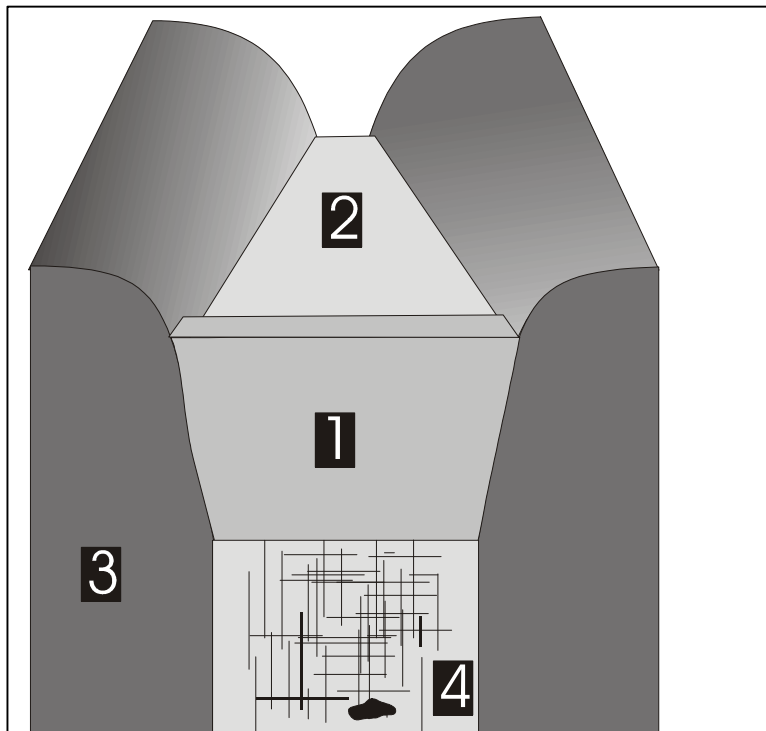


Fig. 3.1.1. Geological setting.

- 1) Dam site;
- 2) Impounding water;
- 3) Valley – impermeable rocks;
- 4) Bottom of the valley – soluble rock dissected by a net of fractures. Larger voids and a cave are also presented.

Fig. 3.1.1 presents an idealized model of a dam site. It is a narrow valley underlain by karstifiable soluble rock. Our main interest is for limestone, but for comparison we present also a scenario, where this rock is gypsum. The slopes of the valley consist of insoluble and impermeable rocks extending below the surface down to the soluble rock. The dam site impounds water at height H . Its impermeable basis has width W . An impermeable grouting curtain extends into the soluble rock to a depth G , below the dam.

The height of the impounded water is constant during the evolution of the system. We assume that there is enough water, flowing from the catchment area to keep the level constant until the end of the simulation. We stop the calculations, when the leakage reaches a prescribed maximal allowed value – $2 \cdot 10^5 \text{ cm}^3/\text{s}$ per meter of the dam width. In the case of a dam site 100 meters wide, this corresponds to leakage rates of $20 \text{ m}^3/\text{s}$, which are regarded as unbearable.

As in the scenario of the preceding chapter, there is a net of primary, yet unwidened fractures and fissures, which comprise percolating pathways from the bottom of the reservoir to the valley downstream. This network is characterized by the average spacing s of the

fractures, their aperture widths a_0 and their widths b_0 . As already discussed, the hydraulic conductivity of such a fracture system is given by Eq. 1.22 (Lee and Farmer, 1993). In the reality not all of the fractures have equal initial aperture widths. Therefore, in addition to the network with equal initial aperture widths of its fractures (Uniform scenario), we use also a statistical distribution of the fracture initial aperture widths (Statistical scenario).

There is one important difference in the geological setting in comparison with the scenarios discussed in Chapter 2. The soluble rock is extending below the dam to a certain depth under the ground. In this case, the average aperture widths of the primary joints are about 0.015 cm, and are decreasing exponentially with depth to values of about 0.008 cm (Lee and Farmer, 1993). In already karstified rocks these numbers may be higher, but in any case aperture widths in the range between several 10^{-2} cm to $3 \cdot 10^{-3}$ cm are considered as reasonable. At the same time the average spacing s of the fractures is decreasing from 5 m at the surface to about 10 m at depths below 50 meters (Lee and Farmer, 1993).

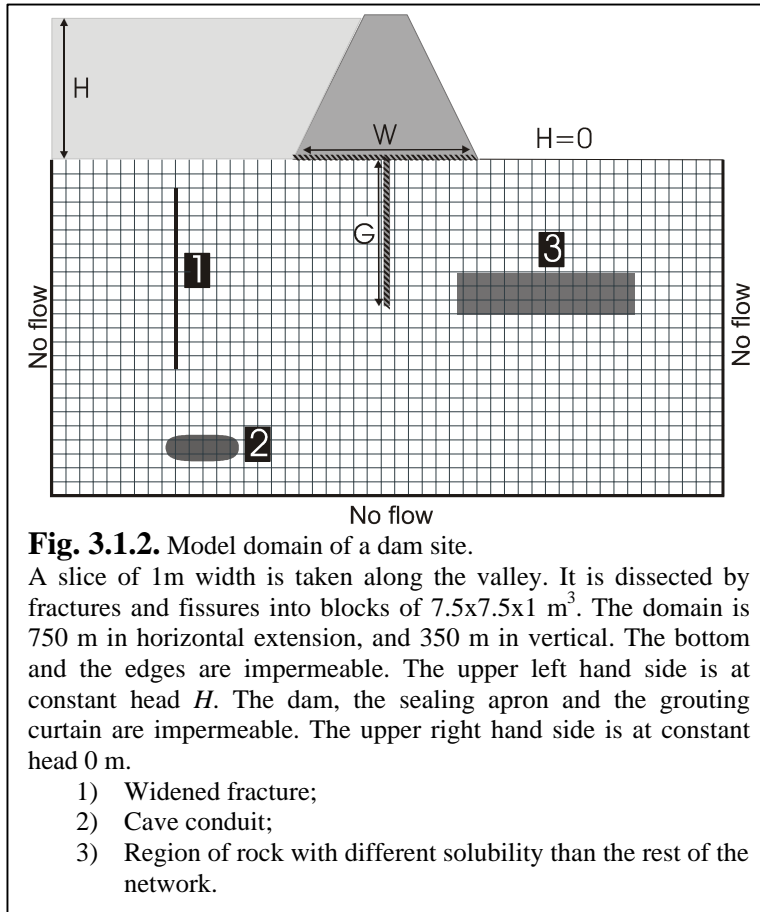
In our scenario we use a net of fractures with a lognormal statistical distribution of the initial aperture widths (Gale, 1987). In this way we fulfill the requirements discussed so far. At the same time we are able to take into account the influence of some initially significantly larger fractures forming preferential pathways through the rock.

Some regions where dams are constructed, are highly karstified (Milanovic, 2000). Our model is able to take into account situations like this. We are able to model the behavior of the structure in the presence of large cave conduits below the grouting curtain.

3.1.2. Modeling domain

Fig. 3.1.2 depicts a two-dimensional cross section of the scenario from Fig. 3.1.1. This is our modeling domain. It is a rectangular network - 750 m x 350 m x 1m – divided by fractures and fissures into blocks of 7.5 m by 7.5 m by 1 m. We are able to apply different properties to every fracture in the modeling domain. Using different initial aperture width for every fracture we are able to model any kind of heterogeneity in the aquifer. At places where the bedrock is impermeable (the region of the grouting curtain for example) the fractures are omitted from the network.

At the same time different lithologies of the bedrock may cause changes in its dissolution kinetics reflected by the rate constants k_l and k_n (see Eq. 1.15). Assigning different rate constants to each fracture individually, gives us the opportunity to model the influence of different lithologies and also insoluble rock ($k_l=k_n=0$) embedded into the domain.



We start with the investigation of the basic processes governing the evolution of the system dam site - underlying block of soluble rock. In the first set of simulations the soluble rock is limestone, therefore the laws governing the dissolution kinetics typical for limestone must be applied. Detailed discussion about these laws is given by Buhmann and Dreybrodt (1985 a, b), Dreybrodt (1988), Dreybrodt and Buhmann (1991), Liu and Dreybrodt (1997), Dreybrodt et al. (1996), Svenson and Dreybrodt (1992),

Eisenlohr et al. (1999) and Dreybrodt and Eisenlohr (2000).

Two basic scenarios are discussed:

- a) Scenario A – the width W of the dam is 262 meters, and the grouting depth G is 97 meters;
- b) Scenario B has width $W=82$ meters and grouting depth $G = 187$ meters.

We present two sets of calculations for both basic scenarios:

- a) Uniform initial distribution of the fractures aperture width $a_0=0.02$ cm;
- b) Lognormal distribution with average aperture width with mean $a_0=0.02$ cm and $\sigma=0.01$.

In all simulation runs throughout this work the sealing apron and the grouting curtain are considered as impervious.

The hydrological boundary conditions are the same for both basic scenarios:

- a) Height H of the impounded water – 150 meters (see Fig. 3.1.2);
- b) Hydraulic head on the valley side - 0 meters;
- c) No flow boundary conditions on the left hand side and right hand side boundaries, and at the bottom of the domain.

In our case the bottom of the modeling domain is 375 meters below the ground. Even if the soluble rock extends further in vertical direction, its permeability at depths close to 400 meters is so low, that it can be considered as practically impermeable (Milanovic, 1981, 2000). The situation with the left hand side and the right hand side boundaries is not so simple.

Description	Symbol	Unit	Numerical values
Network parameters			
Initial fracture aperture with	a_0	cm	0.02
Fracture width	b	cm	100
Fracture length	L	cm	750
Domain dimension		m	750 x 375
Parameters of dam site			
Hydraulic head	H	m	150
Grouting depth	G	m	97 (A), 187 (B)
Apron width	W	m	262 (A), 82 (B)
Limestone: Chemical parameters			
Order of nonlinear kinetics	n		4
Nonlinear kinetics constant	k_n	$\text{mol} / \text{cm}^2 \text{s}^{-1}$	$4 * 10^{-8}$
Concentration of calcium	c	mol/cm^3	$c_{in} < c < c_{eq}$
Initial concentration	c_{in}	mol/cm^3	0
Switch concentration	c_s	mol / cm^3	$0.9 c_{eq}$
Equilibrium concentration	c_{eq}	mol / cm^3	$2 * 10^{-6}$
Gypsum: Chemical parameters			
Order of nonlinear kinetics	n		4.5
Nonlinear kinetics constant	k_n	$\text{mol} / \text{cm}^2 \text{s}^{-1}$	$3 * 10^{-3}$
Concentration of calcium	c	mol/cm^3	$c_{in} < c < c_{eq}$
Initial concentration	c_{in}	mol/cm^3	0
Switch concentration	c_s	mol / cm^3	$0.95 c_{eq}$
Equilibrium concentration	c_{eq}	mol / cm^3	$15.4 * 10^{-6}$

Table 3.1.1. Model parameters

According to Fig. 3.1.1 the rock is not impermeable. To model this, we would have to extend the modeling domain to kilometers in both, left and right, directions. Since our computer capacity is limited, this is actually not possible at present. On the other hand, most flow to the valley will be through a finite region below the dam. Consequently, the influence of the left and right hand side boundaries on the evolution will decrease relatively fast with increasing

size of the modeling domain. We perform several test runs for a domain with dimensions 1500 by 750 meters. The spacing between the fractures is – 7.5 meters. We observe no change in the evolution of our basic scenarios in comparison with the evolution for a size of the domain 750 by 375 meters. Therefore we regard the impervious boundaries as appropriate for the dimensions of the modeling domain (750 meters by 375 meters) and the dimensions of the hydraulic structure.

The concentration of the inflowing water is assumed to be $c_0=0 \text{ mol/cm}^3$. All the chemical and hydrological parameters used for the basic scenarios are depicted in Table. 3.1.1.

3.1.3. Numerical results for the standard scenarios

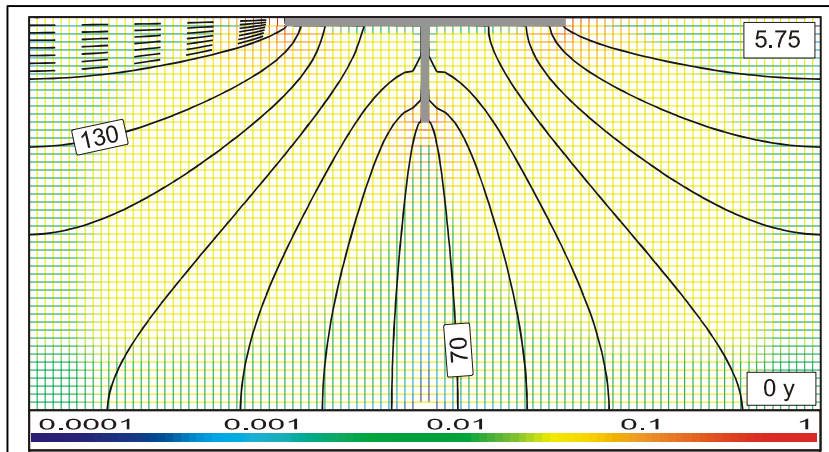


Fig. 3.1.3. Initial distribution of flow rates and aperture widths – Standard Scenario A (see text).

The thick black lines represent the hydraulic head distribution – starting at 150 m at every 1.25 m (dashed lines), and at every 10 m (solid lines).

The color code designates the flow rates in a logarithmic scale. The maximal flow rate $Q_{max} [cm^3/s]$ is depicted at the upper right corner and by the red color. Dark blue means $0.0001 \times Q_{max}$. Note that all fractures carrying flow smaller than $0.0001 \times Q_{max}$ are omitted from the figure.

Fig. 3.1.3 depicts the initial flow rates, aperture widths and pressure head distribution for the uniform case of scenario A. The color code represents the flow rate through the current fracture, with respect to the maximal flow carried by a fracture from the network. The scale is logarithmic. This means that the blue fractures carry four orders of magnitude

less flow than the red ones. The dashed black lines depict the pressure head distribution at steps of 1.25 meters and the full ones at 10 meters.

Note that Fig. 3.1.3 shows only the initial situation for the uniform domain of scenario A. The network is still unchanged and there are no widened fractures. The aquifer is homogeneous and the pressure lines are evenly distributed. The pressure lines show a symmetrical pattern with respect to the grouting curtain. Hydraulic gradients are steepest for the pathways close to the structure (see Fig. 3.1.3). The amount of flow through the fractures close to the dam is almost two orders of magnitude higher than through the fractures more distant and towards right hand side boundaries of the domain. This higher flow means more aggressive water entering the upstream part of the domain. Consequently, the dissolution rates

will be higher there, and a channel will start its growth from the bottom of the reservoir, downstream along the grouting curtain, towards the output part of the domain. This channel grows along the shortest route from the input to the output side.

3.1.3.1. Standard scenario A – uniform case

The dimensions of the dam structure for the standard scenario A are: $W=262$ meters, and $G=97$ meters.

The evolution of the aperture fracture widths, the flow rates, the dissolution rates, and the pressure head distribution is depicted in Fig. 3.1.4 a-1. The meaning of the color and the bar code is:

Fig. 3.1.4a, c, e, g, i, k – the color code designates the flow rates in a logarithmic scale. The maximal flow rate Q_{max} is depicted by the red color. Dark blue means $0.0001 \times Q_{max}$. All fractures carrying flow smaller than $0.0001 \times Q_{max}$ are omitted from the figure.

Fig. 3.1.4b, d, f, h, j, l – the color code designates the dissolution rates in a logarithmic scale. The maximal dissolution rate F_{max} is depicted by the red color. Dark blue means $0.0001 \times F_{max}$. If the dissolution rate along the fracture is smaller than $0.0001 \times F_{max}$, then the fracture is omitted from the figure.

The bar code is the same for all subfigures of Fig. 3.1.4. It depicts the aperture width of the fracture in centimeters. Note that even sufficiently widened fractures can be omitted from the figure if the flow through them or the dissolution rate at their exit is too small.

The thick black lines represent the hydraulic head distribution – at every 1.25 meters (dashed lines) and every 10 meters (full lines). Note that the figure is split into two parts.

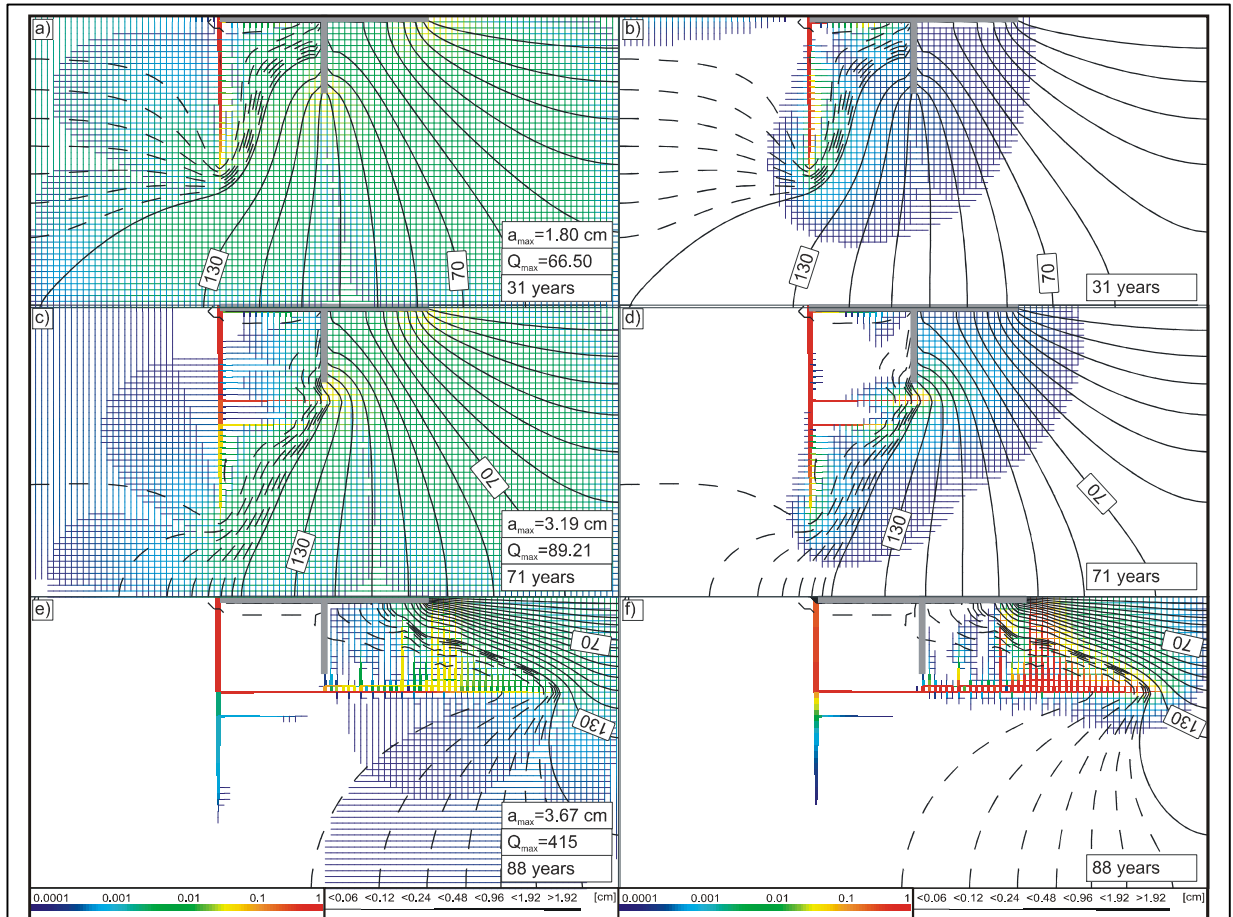


Fig. 3.1.4 (part 1 - a-f). Evolution of the fracture aperture widths, pressure head, flow rates, and dissolution rates for Standard Scenario A uniform case (see text).

The bar code represents the fracture aperture widths in centimetres. The maximal aperture width $a_{max}[cm]$ is depicted at the lower right corner.

Time is depicted at the lower right corner.

The thick black lines represent the isolines of the pressure head distribution starting at 150 m at every 1.25 m (dashed lines), and every 10 m (solid lines).

The color code (subfigures a, c, e) designates the flow rates in a logarithmic scale. The maximal flow rate Q_{max} [cm^3/s] is depicted at the lower right corner, and by the red color. Dark blue means $0.0001 \times Q_{max}$. Note that all fractures carrying flow lower than $0.0001 \times Q_{max}$ are omitted from the figure.

The color code (subfigures b, d, f) designates the dissolution rates in a logarithmic scale. The maximal dissolution rate F_{max} ($4 \cdot 10^{-11} \text{ mol cm}^{-2} \text{ s}^{-1}$) is depicted by the red color. Dark blue means $0.0001 \times F_{max}$. Note that all fractures with dissolution rates smaller than $0.0001 \times F_{max}$ are omitted from the figure.

Fig. 3.1.4 a, b depict the situation after 31 years of evolution. A channel starts to grow vertically close to the rim of the sealing apron and parallel to the grouting. It grows in the region with the highest initial flow and steepest hydraulic gradient (see Fig. 3.1.3). There is flow out from the widened channel into the surrounding network, increasing with depth and maximal at the tip. This behavior looks similar to the early evolution of the standard scenario of Chapter 2 (see Fig. 2.1.7a). The channel growth here follows the different head distribution imposed by the geometry of the setup. The flow out at the tip accelerates the evolution of the channel in comparison to the rest of the network. Once it is created, it behaves in the same way as the central conduit discussed in the previous chapter. The widened part of the channel

causes a redistribution of the pressure head along it. The highest hydraulic gradients are at the tip. The rest of the network is still unaffected and consequently the pressure distribution there remains even. The flow out from the channel is higher from the side directed to the dam (right hand side). Consequently the dissolution rates on both sides are different (Fig. 3.1.4 b). In contrast to the left hand side, where the dissolution rates are almost negligible, the situation on the right hand side is quite complicated. There are already some fractures growing there, which are perpendicular to the widened conduit (see the bar code Fig. 3.1.4 a, b). The depth, where these fractures start to develop is close to the level of the grouting curtain. Fig. 3.1.4 b shows that the dissolution rates at the tip of the channel are close to the rates along the widened fractures. These fractures belong to the shortest pathways to the exit. Consequently, the growth of the widened conduit will be diverted in a direction below the dam.

This is exactly what is depicted in Figs. 3.1.4 c, d. After 71 years of evolution, the widened channel has penetrated further downwards. Its growth in this direction is much slower than in the first 31 years. The main head drop is close to the end of the widened part. This is the zone of the highest hydraulic gradients. The pressure distribution in the unwidened part of the network is still unaffected and even. Consequently the flow out at the valley is evenly distributed.

The small fractures, growing on the right hand side of the widened conduit, continue to develop in the direction below the grouting. The ones, at depths lower than the depth of the grouting, have stopped their growth. Only two of them continue to propagate below the dam. The reason for these channels to develop is, that the region where they grow is the most dynamically evolving part of the network. The figures depicting the dissolution rates (Fig. 3.1.4 b and Fig. 3.1.4 d) show that these rates are different in the different parts of this region. Consequently the region becomes inhomogeneous and some characteristics are common with the statistical scenarios.

The upper horizontal competitive channel has penetrated beyond the grouting curtain. The flow out to the surrounding network is maximal at its tip (see Fig. 3.1.4 c), and because of the asymmetry of the setup, is higher in the vertical direction. The dissolution rates (Fig. 3.1.4 d) are also higher along the fractures on the upper side of the widened conduit. Our experience from Fig. 3.1.4a, b, shows that these conditions will cause new channels to grow vertically from the leading horizontal walls.

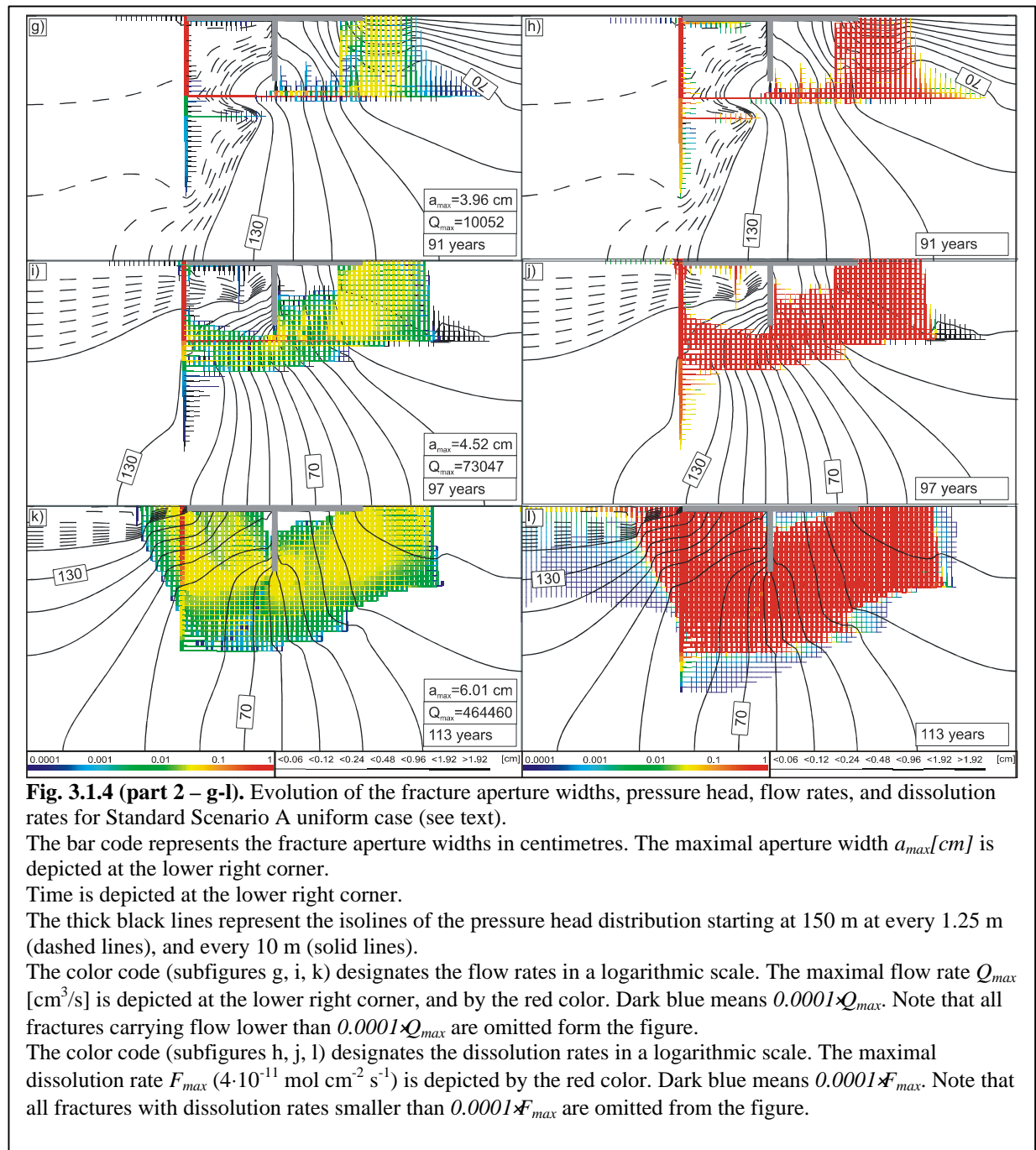


Fig. 3.1.4 e, f depicts the situation after 88 years. The upper competitive channel has propagated further and its widened part is already in the region of the right hand side impervious boundary. Some vertical fractures start to grow on the upper part of the channel. The pressure distribution along them marks the region of the highest hydraulic gradients. The dissolution rates there are close to the maximal value for the whole domain. Consequently, these fractures mark the area of the further evolution of the aquifer. As soon as one of them reaches the exit at the valley, breakthrough occurs. The way and the pattern of the growth of the presently discussed vertical fractures show, that the aquifer in the zone below the dam, along the length of the sealing apron, is highly inhomogeneous. This is depicted by the vertical

fractures growing there. Some of them are still active with high flow and dissolution rates along them. Others are abandoned and do not continue their evolution. This is similar to the evolution of the two horizontal channels discussed above.

The evolution of the lower horizontal channel is stopped. The flow, and the dissolution rates along it are four orders of magnitude lower than the ones along the upper conduit (see Fig. 3.1.4 e, f).

Fig. 3.1.4 g, h depicts the situation at 91 years. This is shortly after breakthrough. Some of the vertical growing channels are already connected to the exit. There is a clearly visible widened pathway, starting at the bottom of the dam site, extending below the impermeable structure, and exiting at the valley below the dam. The pressure head is redistributed along this pathway and consequently along the whole domain. This channel is embedded into a network of still unwidened fractures. The highest flow rates are along the widened conduits (see Fig. 3.1.4g). The regime of the flow is already turbulent. Solution with a very low Ca concentration is entering these fractures, and the dissolution rates along the pathway are almost even (see Fig. 3.1.4 h). This causes continuous further growth of the channels comprising the pathway. There is no zone of outflow of aggressive solution from the widened pathway into the surrounding net. Only a little amount of water from the net enters the widened fractures – Fig. 3.1.4 g. Consequently an exit type fan cannot grow.

Fig. 3.1.4 i, j depict the situation after 97 years of evolution. The pressure head distribution is more even along the whole domain. Net of widened fractures at the bottom of the reservoir and below the sealing apron has extended, because they grow on the left and on the right hand sides of the widened pathway and parallel to it. At the same time in the beginning of the horizontal part of the pathway, some fractures from the surrounding network are already widened and connected to it. The same is visible in the beginning of the second vertical part of the main pathway. These fractures mark the beginning of the evolution of entrance fans. Any of the three branches (two vertical along the grouting curtain, and one horizontal below the sealing apron) develop entrance fans. Because of the asymmetry of the setup, these fans will not grow symmetrically on both sides of the pathway. Another reason is the secondary heterogeneity of the network in the region close to the impervious structure. For details about the evolution of an entry fan – see Chapter 2.

The continuing growth of the fans and their incorporation into the widened pathway, is depicted on Fig. 3.1.4 k, l. It shows the situation after 113 years. The widened pathway carries most of the flow through the domain (see Fig. 3.1.4 k). The dissolution rates are even and close to maximum along the whole pathway – Fig. 3.1.4 l. This assures its continuous, fast widening.

Because of the evolution of the fans, this zone expands radially around the impervious structure, conquering the whole modeled domain.

3.1.3.2. Standard scenario B – uniform case

The dimensions of the dam structure are: $W=82$ meters, $G=187$ meters. By this way we keep the $W+2G$ the same as for the standard scenario A. Consequently the length of the evolving pathway is similar for both scenarios. The hydrological and the chemical boundary conditions for the standard scenario B are shown in Table 3.1.1.

The evolution of the aperture fracture widths, the flow rates, the dissolution rates and the pressure head distribution is depicted in Fig. 3.1.5 a-l. The meaning of the color and the bar code is:

Fig. 3.1.5a, c, e, g – the color code designates the flow rates in a logarithmic scale. The maximal flow rate Q_{max} is depicted by the red color. Dark blue means $0.0001 \times Q_{max}$. All fractures carrying flow smaller than $0.0001 \times Q_{max}$ are omitted from the figure.

Fig. 3.1.5b, d, f, h – the color code designates the dissolution rates in a logarithmic scale. The maximal dissolution rate F_{max} is depicted by the red color. Dark blue means $0.0001 \times F_{max}$. If the dissolution rate along the fracture is smaller than $0.0001 \times F_{max}$, then the fracture is omitted from the figure.

The bar code is the same for all subfigures of Fig. 3.1.5. It depicts the aperture width of the fracture, in centimeters. Note that even sufficiently widened fractures can be omitted from the figure if the flow through them or the dissolution rate at their exit is too small.

The thick black lines represent the hydraulic head distribution – at every 1.25 meters (dashed lines) and every 10 meters (full lines).

Fig. 3.1.5 a, b depicts the situation after 26 years. A vertical channel is growing from the bottom of the reservoir similar to the evolution of the standard scenario A (see Fig. 3.1.4a). This channel changes the head distribution in the neighboring area. The flow rates are maximal along the channel – Fig. 3.1.5 a. The pressure distribution depicts the outflow of water from the channel into the surrounding network. This outflow is maximal at the tip of the conduit. The dissolution rates are maximal along the channel and on the right hand side of the tip. This marks the area of the further growth of the pathway.

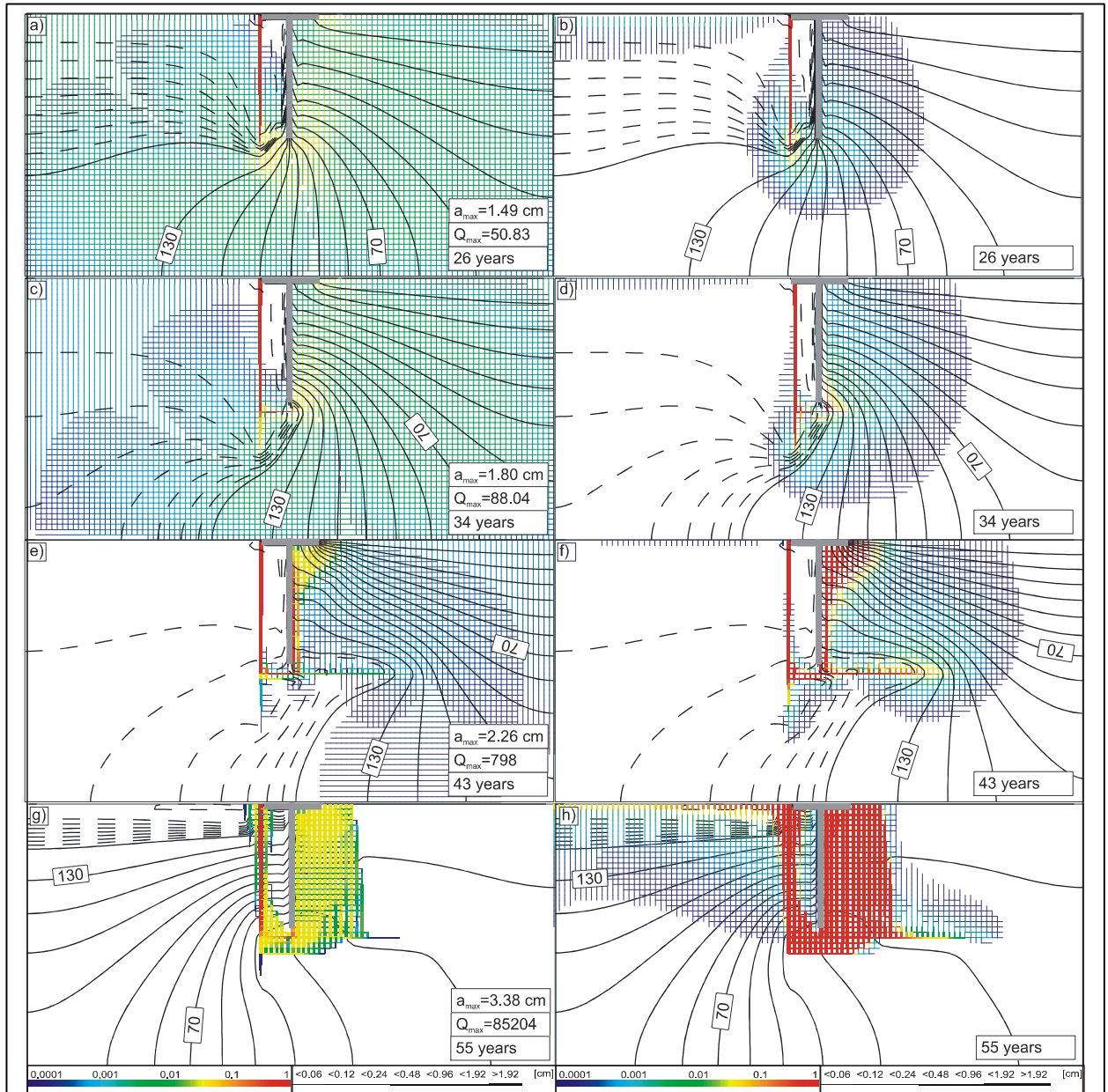


Fig. 3.1.5. Evolution of the fracture aperture widths, pressure head, flow rates, and dissolution rates for Standard Scenario B uniform case (see text).

The bar code represents the fracture aperture widths in centimetres. The maximal aperture width $a_{max}[cm]$ is depicted at the lower right corner.

Time is depicted at the lower right corner.

The thick black lines represent the isolines of the pressure head distribution starting at 150 m at every 1.25 m (dashed lines), and every 10 m (solid lines).

The color code (subfigures a, c, e, g) designates the flow rates in a logarithmic scale. The maximal flow rate Q_{max} [cm^3/s] is depicted at the lower right corner, and by the red color. Dark blue means $0.0001 \times Q_{max}$. Note that all fractures carrying flow lower than $0.0001 \times Q_{max}$ are omitted from the figure.

The color code (subfigures b, d, f, h) designates the dissolution rates in a logarithmic scale. The maximal dissolution rate F_{max} ($4 \cdot 10^{-11} \text{ mol } cm^{-2} s^{-1}$) is depicted by the red color. Dark blue means $0.0001 \times F_{max}$. Note that all fractures with dissolution rates smaller than $0.0001 \times F_{max}$ are omitted from the figure.

This growth is depicted in Fig. 3.5 c, d after 34 years of evolution. The speed of vertical growth of the channel is reduced. Instead of this a horizontal one is evolving below the grouting curtain at depth close to the length of this curtain. It marks the area of the steepest hydraulic gradients, and the shortest pathway to the exit in the valley. The vertical channel is divided into two branches in the same way like in the standard scenario A. The horizontal channel takes most of the water coming from the entrance (Fig. 3.1.5 c). The dissolution rates along both branches are similar (Fig. 3.1.5 d). The picture around their tips shows that the horizontal branch will be divided once again, and a second vertical conduit will develop along the grouting curtain in the direction of the exit of the domain.

The situation shortly before the breakthrough event, at 43 years, is depicted in Fig. 3.1.5 e, f. As expected the horizontal branch has divided into two parts.

The vertical one grows in the direction of the exit, while the horizontal one continues to penetrate further in the direction to the right hand side. In contrast to the situation in scenario A, the vertical channel grows practically next to the grouting curtain. A zone of high permeability is created in the area below the dam site.

The situation at 55 years is depicted in Fig. 3.1.5 g, h. This is several years after the breakthrough event. Similar to the first standard scenario the flow through the widened part of the network is already turbulent (Fig. 3.1.5 g). The pressure head is redistributed and is more even along the whole domain. The Ca concentration of the water flowing through the widened pathway is low causing almost equal dissolution rates there (see Fig. 3.1.5 h). The entrance type fans develop along the main branches of the pathway, assuring the expansion of the widened area throughout the whole domain.

3.1.3.3. Standard scenario A – statistical case

In order to model scenarios closer to the natural conditions we extend our standard setups by introducing a statistical distribution of the initial aperture widths of the fractures used to build the networks. The mean value of the lognormal distribution is set to $a_0=0.02$ cm and $\sigma=0.01$. We use the same boundary and geometrical conditions as in the simulations so far (see Table. 3.1.1).

The evolution of the aperture fracture widths, the flow rates, the dissolution rates and the pressure head distribution is depicted in Fig. 3.1.6 a-l. The meaning of the color and the bar code is:

Fig. 3.1.6a, c, e, g – the color code designates the flow rates in a logarithmic scale. The maximal flow rate Q_{max} is depicted by the red color. Dark blue means $0.0001 \times Q_{max}$. All fractures carrying flow smaller than $0.0001 \times Q_{max}$ are omitted from the figure.

Fig. 3.1.6b, d, f, h – the color code designates the dissolution rates in a logarithmic scale. The maximal dissolution rate F_{max} is depicted by the red color. Dark blue means $0.0001 \times F_{max}$. If the dissolution rate along the fracture is smaller than $0.0001 \times F_{max}$, then the fracture is omitted from the figure.

The bar code is the same for all subfigures of Fig. 3.1.6. It depicts the aperture width of the fracture, in centimeters. Note that even sufficiently widened fractures can be omitted from the figure if the flow through them or the dissolution rate at their exit is too small.

The thick black lines represent the hydraulic head distribution – at every 1.25 meters (dashed lines) and every 10 meters (full lines).

The basic behavior of the evolution is similar to the ones of the uniform scenario A. A vertical channel evolves downwards on the left hand side of the sealing apron, along the grouting curtain. This is depicted on Fig. 3.1.6 a, b. As already discussed, this channel evolves in the zones favored by the geometry of the setup, and by its initial boundary conditions. The main difference, resulting from the statistical distribution of the initial aperture widths, is the existence of several pathways, which could be favored because of their initially wider aperture widths. This is the reason for the observed diversion of the vertical pathway in the direction of the grouting curtain. The existence of such initially wider pathways also causes the growth of vertical channels in the areas away from the impermeable dam site structure. These channels are depicted in Fig. 3.1.6 c, d. They start from the bottom of the reservoir and grow independently of the evolution of the zone with low resistance below the dam site. After the breakthrough event, when the growth of the entrance type fans will start to extend this zone, these channels will be integrated into it (Fig. 3.1.6 e-h).

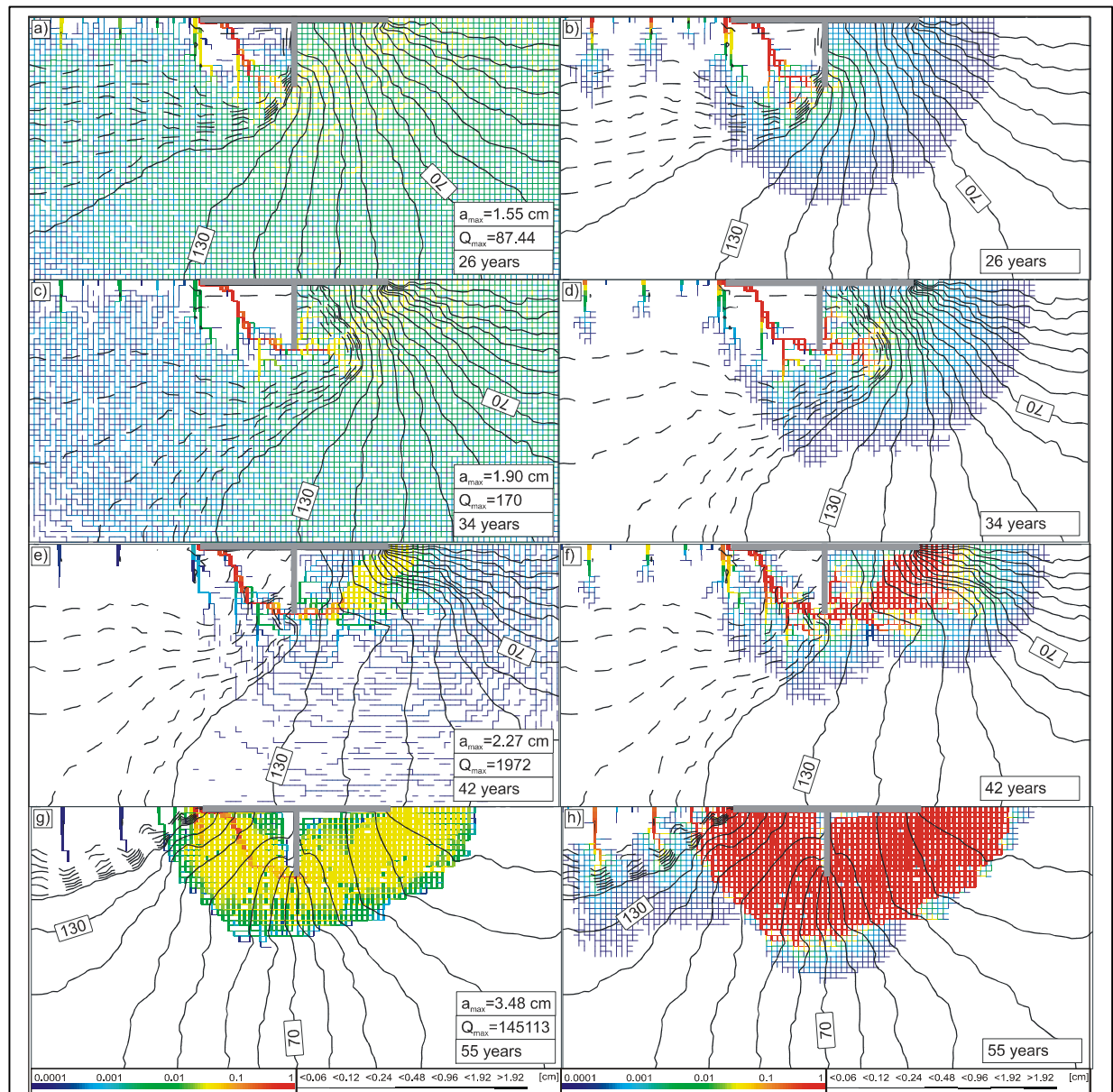


Fig. 3.1.6. Evolution of the fracture aperture widths, pressure head, flow rates, and dissolution rates for Standard Scenario A statistical case (see text).

The bar code represents the fracture aperture widths in centimetres. The maximal aperture width $a_{max}[cm]$ is depicted at the lower right corner.

Time is depicted at the lower right corner.

The thick black lines represent the isolines of the pressure head distribution starting at 150 m at every 1.25 m (dashed lines), and every 10 m (solid lines).

The color code (subfigures a, c, e, g) designates the flow rates in a logarithmic scale. The maximal flow rate Q_{max} [cm³/s] is depicted at the lower right corner, and by the red color. Dark blue means $0.0001 \times Q_{max}$. Note that all fractures carrying flow lower than $0.0001 \times Q_{max}$ are omitted from the figure.

The color code (subfigures b, d, f, h) designates the dissolution rates in a logarithmic scale. The maximal dissolution rate F_{max} ($4 \cdot 10^{-11}$ mol cm⁻² s⁻¹) is depicted by the red color. Dark blue means $0.0001 \times F_{max}$. Note that all fractures with dissolution rates smaller than $0.0001 \times F_{max}$ are omitted from the figure.

3.1.3.4. Standard scenario B – statistical case

The evolution of the aperture fracture widths, the flow rates, the dissolution rates and the pressure head distribution is depicted in Fig. 3.1.7 a-l. The meaning of the color and the bar code is:

Fig. 3.1.7a, c, e, g – the color code designates the flow rates in a logarithmic scale. The maximal flow rate Q_{max} is depicted by the red color. Dark blue means $0.0001 \times Q_{max}$. All fractures carrying flow smaller than $0.0001 \times Q_{max}$ are omitted from the figure.

Fig. 3.7b, d, f, h – the color code designates the dissolution rates in a logarithmic scale. The maximal dissolution rate F_{max} is depicted by the red color. Dark blue means $0.0001 \times F_{max}$. If the dissolution rate along the fracture is smaller than $0.0001 \times F_{max}$, then the fracture is omitted from the figure.

The bar code is the same for all subfigures of Fig. 3.1.7. It depicts the aperture width of the fracture, in centimeters. Note that even sufficiently widened fractures can be omitted from the figure if the flow through them or the dissolution rate at their exit is too small.

The thick black lines represent the hydraulic head distribution – at every 1.25 meters (dashed lines) and every 10 meters (full lines).

Because of the longer grouting curtain, and the shorter sealing apron, the evolution of this case is not much different than the one of the uniform scenario. Fig. 3.1.3 depicts the zone of the steepest hydraulic gradients around the dam site structure. For a case of much longer grouting curtain than sealing apron, this zone is narrow. Therefore none of the initially wider pathways outside of this zone can be used. The only significant difference from the uniform scenario is the independent growth of some vertical fractures, starting at the bottom of the reservoir. As already discussed they will be integrated later into the widened area below the dam - see Fig. 3.1.7 g, h.

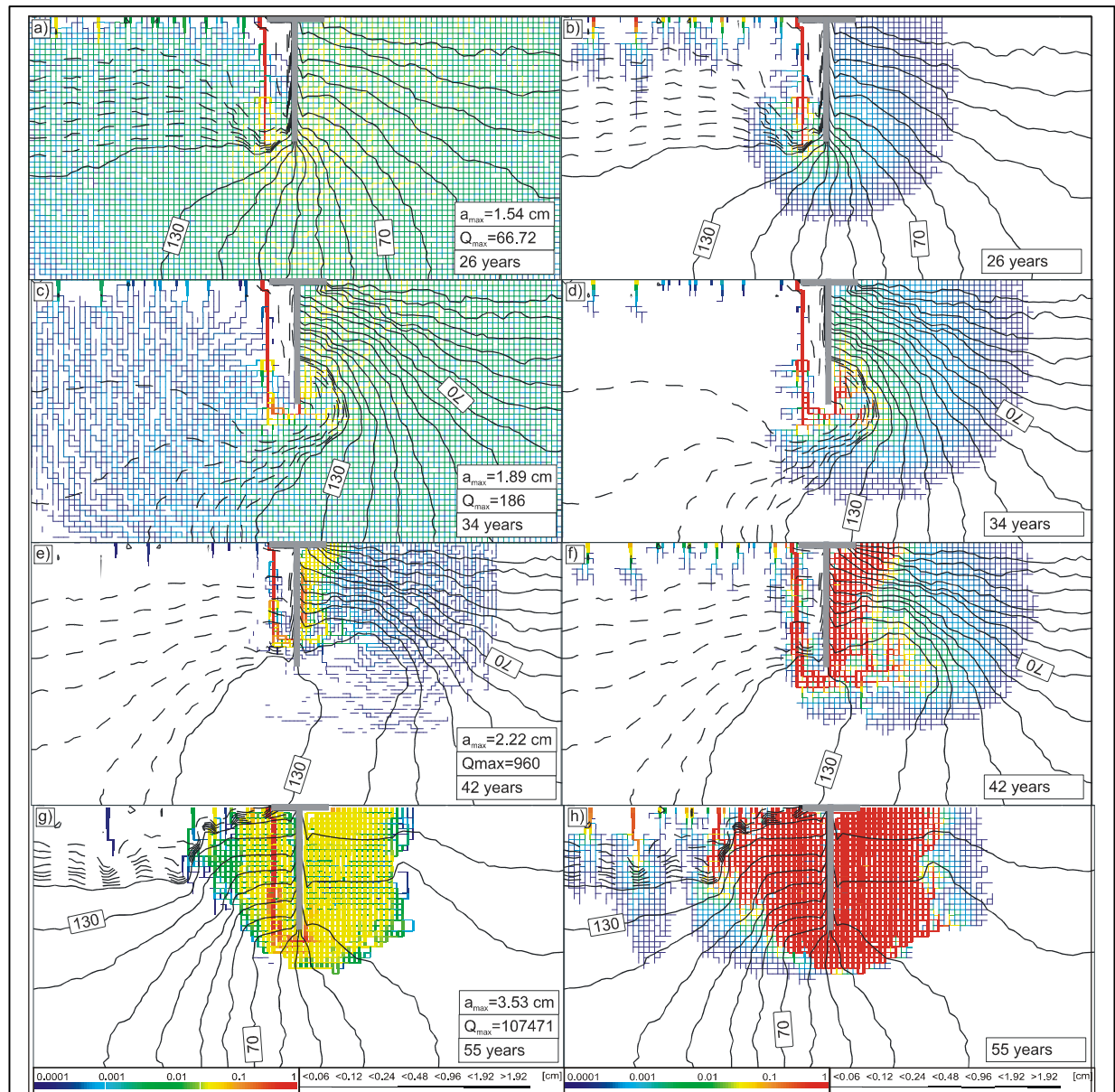


Fig. 3.1.7. Evolution of the fracture aperture widths, pressure head, flow rates, and dissolution rates for Standard Scenario B statistical case (see text).

The bar code represents the fracture aperture widths in centimetres. The maximal aperture width $a_{max}[cm]$ is depicted at the lower right corner.

Time is depicted at the lower right corner.

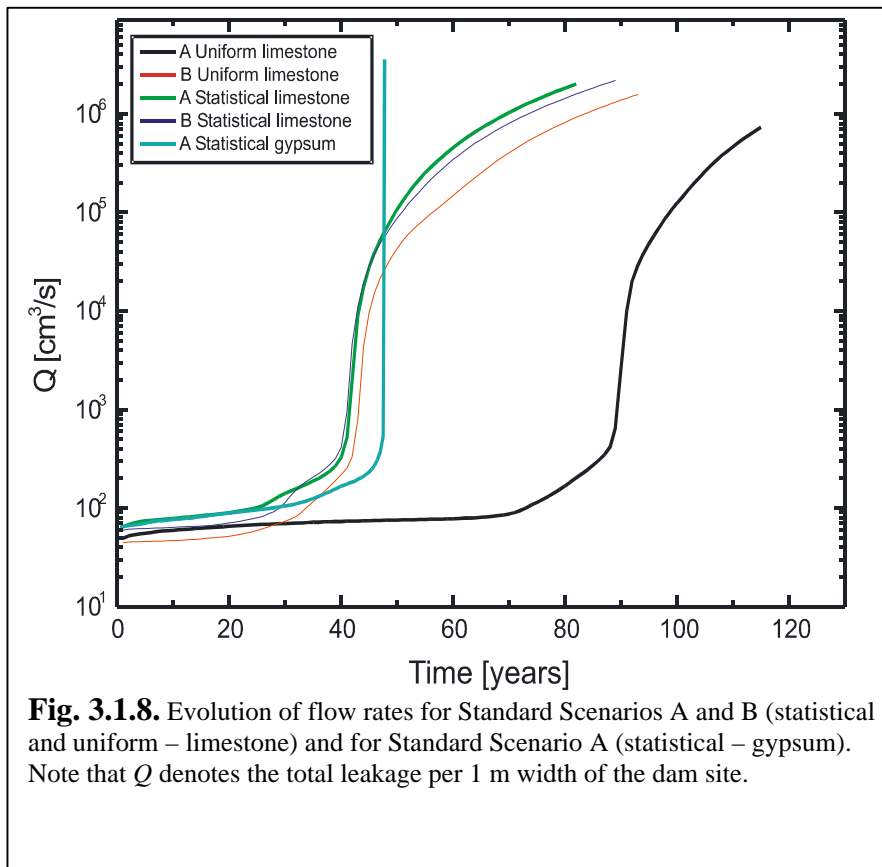
The thick black lines represent the isolines of the pressure head distribution starting at 150 m at every 1.25 m (dashed lines), and every 10 m (solid lines).

The color code (subfigures a, c, e, g) designates the flow rates in a logarithmic scale. The maximal flow rate Q_{max} [cm^3/s] is depicted at the lower right corner, and by the red color. Dark blue means $0.0001 \times Q_{max}$. Note that all fractures carrying flow lower than $0.0001 \times Q_{max}$ are omitted from the figure.

The color code (subfigures b, d, f, h) designates the dissolution rates in a logarithmic scale. The maximal dissolution rate F_{max} ($4 \cdot 10^{-11} \text{ mol cm}^{-2} \text{ s}^{-1}$) is depicted by the red color. Dark blue means $0.0001 \times F_{max}$. Note that all fractures with dissolution rates smaller than $0.0001 \times F_{max}$ are omitted from the figure.

3.1.4. Evolution of the leakage rates for the standard scenarios

The results obtained so far show the complexity of the processes governing the



evolution of the fractured rock close to a dam site. Our goal was to understand this evolution and its relation to different geometries of the dam structures. We know that there is a large zone of widened fractures growing below the hydraulic structure. In order to get a better understanding on the scales of the changes happening in the karst aquifer, we

discuss the evolution of the leakage rates of the dam site with time. Fig. 3.1.8 depicts these for the uniform and the statistical scenarios. They show the total amount of flow through all the fractures with an output at $H=0$ downstream at the valley below the dam. A slow initial increase of the leakage rates is observed. Note that the flow rates are given per meter of the width of the dam, because the width of the fractures used in our model scenarios is 100 cm. The initial leakage for all cases starts with a value of about $60 \text{ cm}^3\text{s}^{-1}$. This amounts to a total of 6 l/s for a hundred meter wide dam. The slow increase of the leakage rates continues until the moment of the breakthrough event. The fast jump in the leakage rates with several orders of magnitude depicts the breakthrough time. After breakthrough the Ca concentration of the water flowing along the widened part of the network is low. Consequently, the dissolution rates in this region reach their maximal values. This causes a stable increase of the leakage rate until it reaches a prescribed value of $2 \cdot 10^5 \text{ cm}^3\text{s}^{-1}$, which for a dam of 100 m width accounts to $20 \text{ m}^3\text{s}^{-1}$, and is regarded as unbearably high.

The breakthrough time for the statistical case of scenario A is around 40 years. In contrast to this, the breakthrough time for the uniform case of this scenario is almost 90 years.

Why? It cannot be caused by the length of the pathways growing below the dam site structure. In both scenarios this is close to $W+2G = 456$ meters. Another reason could be preferential pathways discussed for the statistical cases. It is possible that some of them have initial aperture widths wider than 0.02 cm, and this could be the reason for the accelerated evolution. But to have a significant change in the breakthrough time, we need initially wider channels, which constitute a percolating pathway close to the hydraulic structure. The density of the model network used for our simulations gives a very low probability for the existence of such a channel. We have performed several calculations using different initial distributions of the aperture widths of the fractures. In all cases the breakthrough time was close to 90 years.

Actually the reason for the difference in the breakthrough is the exchange of flow between the growing conduits and the rest of the network.

It was already discussed that the setup of the uniform case for scenario A is similar to

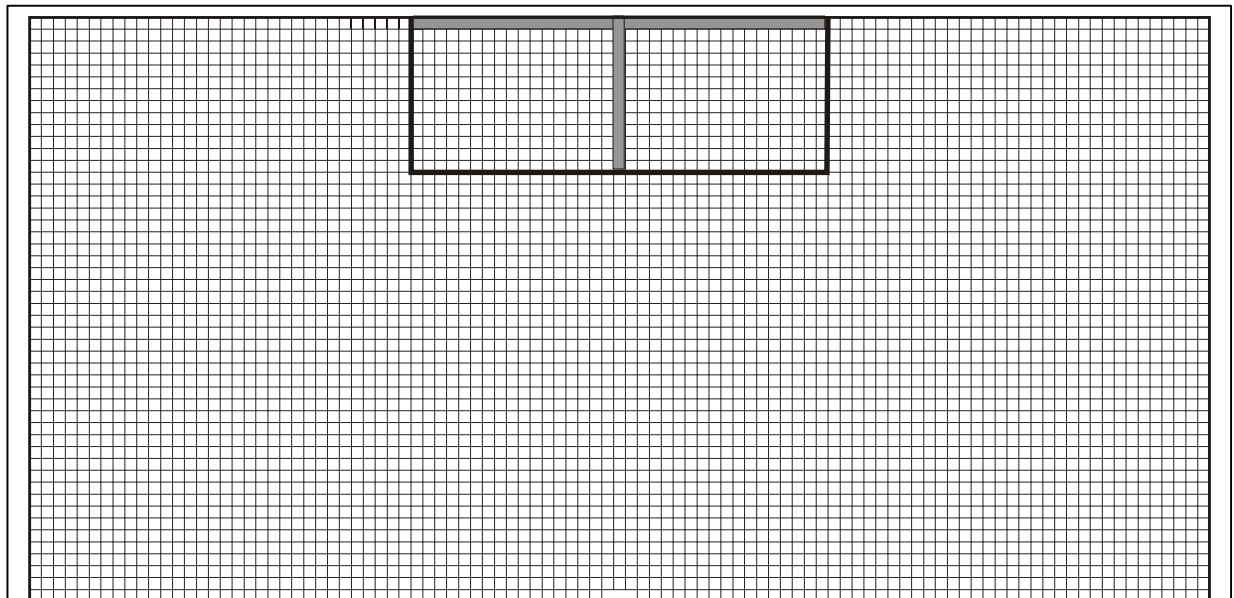


Fig. 3.1.8a. A model scenario used to investigate the influence of the exchange flow on the evolution of the aquifer. Everything is the same as in the Standard Scenario A – uniform case (see Table 3.1.1). The only difference is the aperture widths of the fractures. They are 0.019 cm for all fractures, and 0.02 cm for the pathway depicted by the thick black line.

the setup of the case discussed in the previous chapter, where all the fractures of the network had equal initial aperture widths (see Fig. 2.1.4). Figs. 2.1.5 and 2.1.6 show that the breakthrough time of this scenario (all fractures have initial aperture widths $a_0=0.03$ cm and $A_0=0.03$ cm) was one order of magnitude longer than the breakthrough time of the standard scenario, where a central fracture with the same initial aperture width $A_0=0.03$ cm is embedded into a fracture network consisting of fractures with initial $a_0=0.02$ cm. The reasons for this were already discussed in the previous chapter.

The geometry of our dam site scenario is more complicated and therefore one should not expect exactly the same changes in the breakthrough time. But the mechanism is the same. The growth of the channel is slower for the uniform case because of the smaller amount of flow exchanged with the rest of the network especially in the initial phases. One can argue that in this case the breakthrough time of the uniform case of scenario B should be similar to the one of scenario A – close to 90 years. But as already discussed the geometry of the setup is playing a crucial role for the evolution of the dam site scenarios. Therefore the interaction between the growing conduit and the surrounding network is more complicated than in the scenarios of the previous chapter. But in any case the breakthrough time of the uniform scenario B is longer than any of the breakthrough times obtained for different statistical distributions. The influence of the flow exchanged with the network is different with respect to the geometry of the dam. In some cases the evolution is closer to the single channel case, in some cases it deviates considerably.

To prove the influence of the surrounding network on the breakthrough time of the uniform case of scenario A the following setup is created – see Fig. 3.1.8a. The initial aperture widths of the fractures comprising the shortest pathway from the bottom of the reservoir to the valley downstream are unchanged – $a_0=0.02$ cm. At the same time the initial aperture widths of all the remaining fractures in the network are set to 0.019 cm. It is logical to assume that this will increase the breakthrough time of the system, because of the increased resistance of most of the fractures comprising the network. Actually the breakthrough time is reduced by 7.9%. This is not really a dramatic change, but it proves that increasing the exchange flow between the growing channel and the surrounding network reduces the time for the evolution of the system – a result, discussed in the first chapter. The evolution of the statistical case of the scenario A is even faster, because the heterogeneity of the initial network causes even higher exchange between the growing channel and the surrounding network.

For scenarios B breakthrough times are close to each other, because the close vicinity of the grouting curtain to the evolving channel determines exchange flow similar for both cases.

3.1.5. Standard scenario A – statistical case - gypsum

The setup of our following scenario is exactly the same as the setup and the boundary conditions of the statistical case of scenario A. The only difference is the type of the soluble rock below the dam site structure. In this case it is gypsum. For details about the dissolution

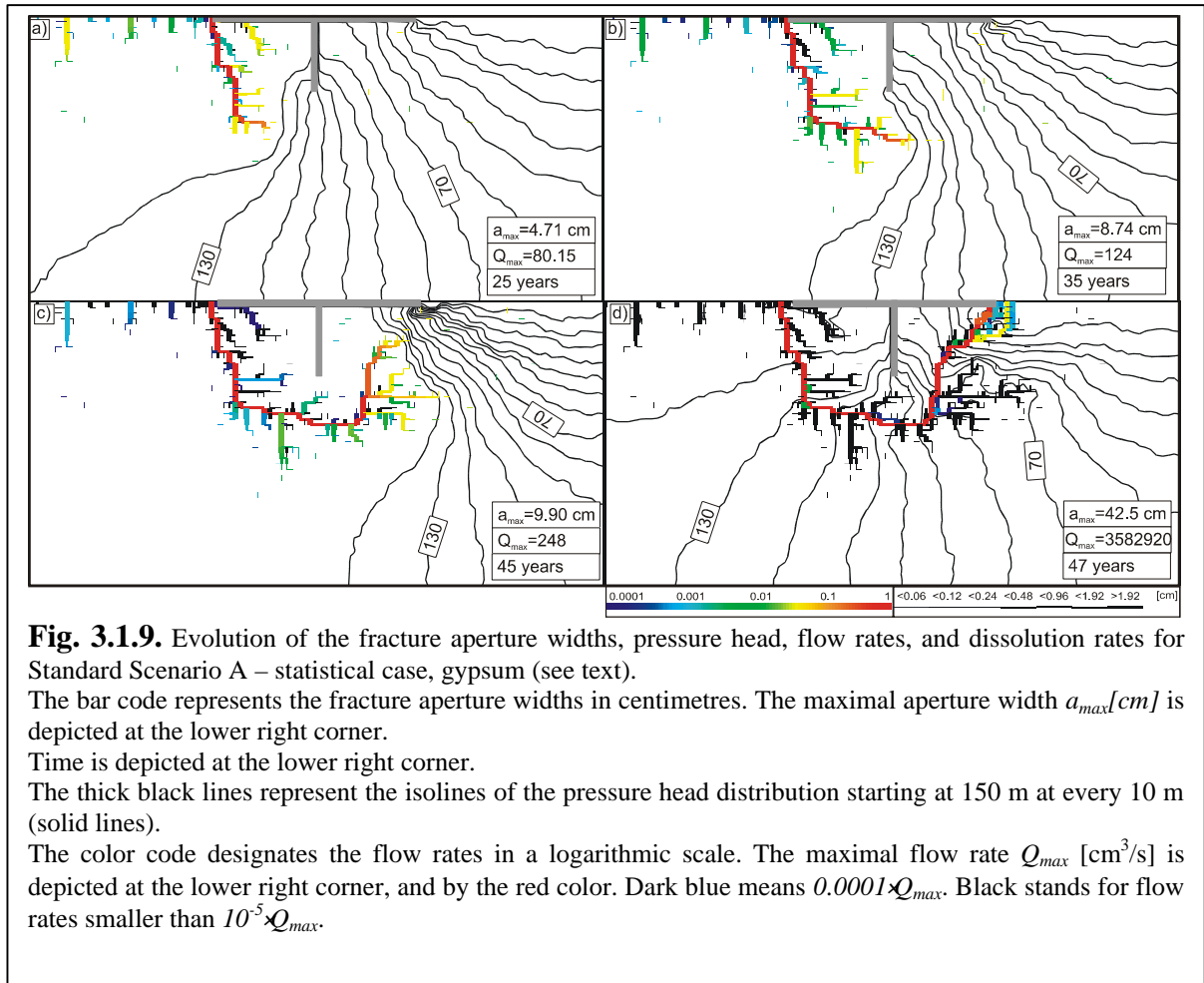
rates and the dissolution constants see (Jeschke et al., 2001). The chemical parameters used in our model are taken from this work and are shown in Table 3.1.1.

The evolution of the aperture fracture widths, the flow rates, the dissolution rates and the pressure head distribution is depicted on Fig. 3.1.9 a-h. The meaning of the color and the bar code is:

Fig. 3.1.9a, b, b, d – the color code designates the flow rates in a logarithmic scale. The maximal flow rate Q_{max} is depicted by the red color. Dark blue means $0.0001 \times Q_{max}$.

The bar code is the same for all subfigures of Fig. 3.1.9. It depicts the aperture width of the fracture, in units of the initial one. All fractures with aperture width smaller than 0.06 the initial one, are omitted from the figure.

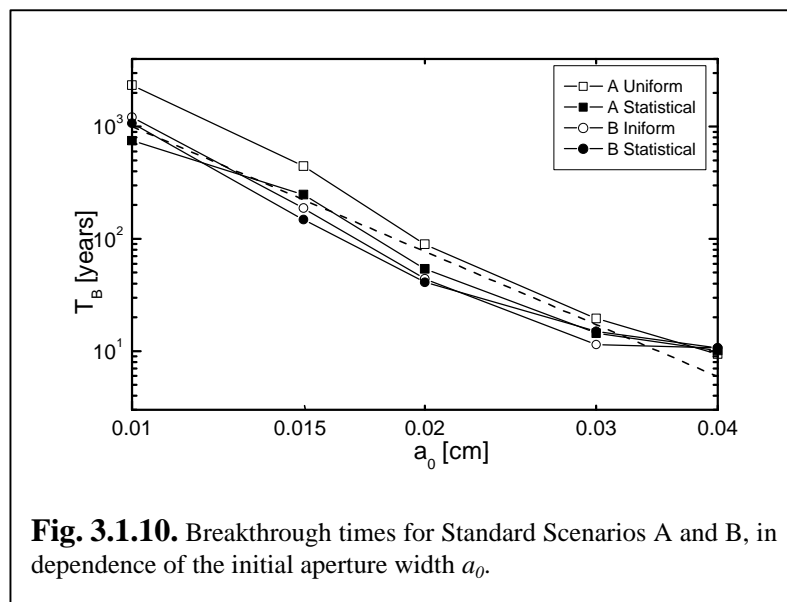
The thick black lines represent the hydraulic head distribution – at every 1.25 meters (dashed line) and every 10 meters (full lines)



There is no significant difference in the evolution of these parameters in comparison to the limestone scenarios. The breakthrough times are also similar, since the nonlinear rate laws mainly determine the evolution of the system before breakthrough. After the breakthrough event water with very low Ca concentration is entering the domain. The dissolution rates are determined by the linear rate laws and are much higher for gypsum than for limestone. The rest of the evolution until the leakage rates become unbearably high is less than a year. Therefore there is no time for the entrance fans to develop and to conquer the whole domain. The pattern of the distribution of the fracture aperture widths is simpler in comparison to the limestone cases. There is only a widened channel along the preferential pathway from the bottom of the reservoir to the valley downstream. But the aperture widths of the fractures there are almost one order of magnitude higher in comparison to the aperture widths of the fractures comprising the widened zone below the dam site construction in the limestone scenarios. The evolution of the leakage rate is depicted in Fig. 3.1.8. The main difference with the leakage rate curves for the limestone cases is after breakthrough because for gypsum bedrock, the dangerous leakage rates are reached in less than a year after breakthrough.

3.1.6. Influence on the basic hydrological and geochemical parameters on the breakthrough time

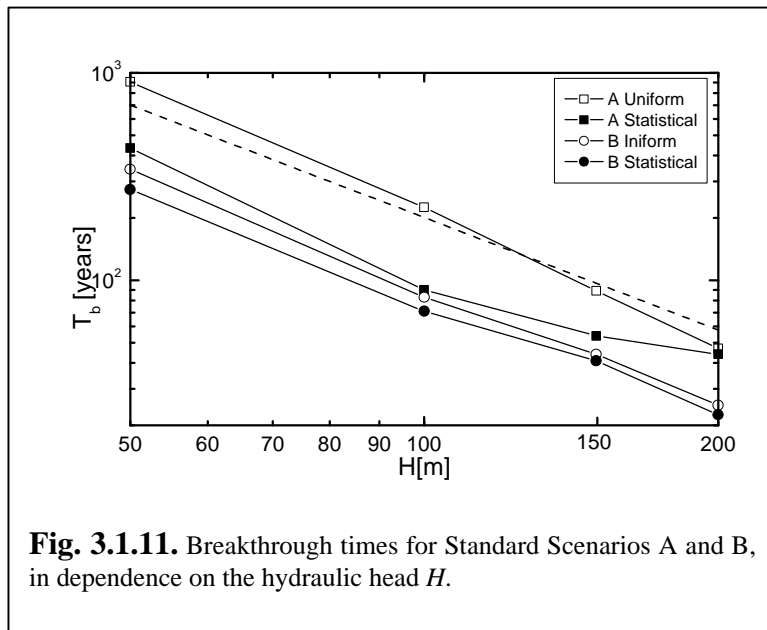
Our next goal is to determine the influence of some of the main parameters on the breakthrough time (T_B). These are the initial aperture width a_0 of the fractures comprising the modeling network, the height H of the impounded water, the length of the grouting curtain G , the concentration c_{in} of the water entering the domain at the bottom of the reservoir, and the equilibrium concentration c_{eq} . In order to estimate the breakthrough behavior of smaller dams we scale H , G and W by a factor f_s , and investigate the variation in the breakthrough time. The soluble rock is assumed to be limestone in all of the discussed scenarios. In all calculations only one parameter is varied. Everything else is kept like in the standard scenarios.



We start with a variation of the initial aperture widths a_0 of the fractures keeping everything else constant. For the statistical scenarios the mean values of the distributions are varied. σ is kept constant. Fig. 3.1.10 depicts the breakthrough time in dependence of the initial aperture widths in a double logarithmic scale. The range of a_0 is – 0.01 to 0.04 cm. The straight dashed line depicts the dependence $T_B \propto a_0^{-3}$ reported by Dreybrodt (1996) and by Dreybrodt and Gabrovsek (2000), for the breakthrough times of single conduits. Siemers and Dreybrodt (1998) find a similar relation for two-dimensional percolation networks. This dependence is valid also for our scenarios if the initial aperture widths are in the range 0.01 cm – 0.03 cm. For $a_0 > 0.03$ cm, T_B drops to about 10 years and the constructions can be regarded as critical. For $a_0 < 0.01$ cm the breakthrough time is larger than 1000 years, which is longer than the exploitation time of the dam.

We start with a variation of the initial aperture widths a_0 of the fractures keeping everything else constant. For the statistical scenarios the mean values of the distributions are varied. σ is kept constant. Fig. 3.1.10 depicts the breakthrough time in dependence of the initial aperture widths in a double

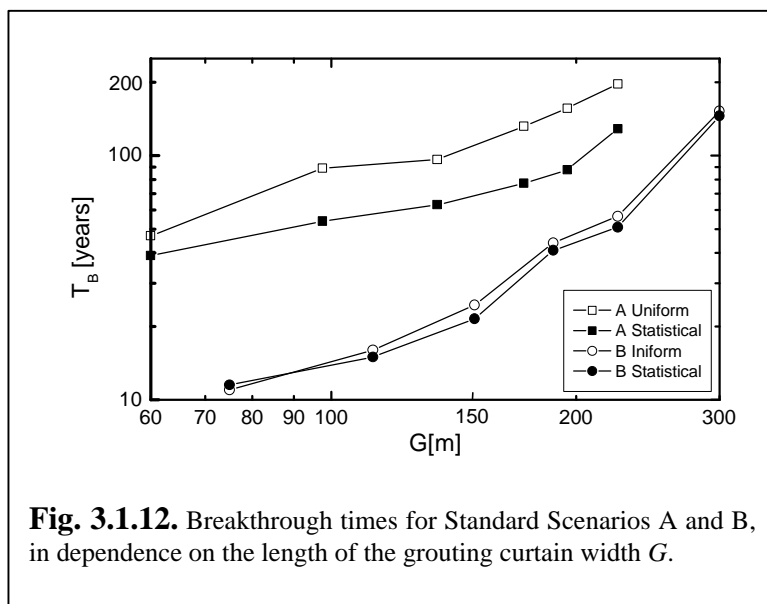
The next parameter is the height H of the impounded water. The dependence of the



breakthrough time on this parameter is depicted in the double logarithmic plots of Fig. 3.1.11. The dashed line shows the dependence $T_B \propto H^{-4/3}$, reported by Dreybrodt (1996) for single channels and by Siemers and Dreybrodt (1998) for percolation networks. This dependence is valid also for the cases of two-dimensional networks discussed in the present

work.

The grouting curtain plays very important role in the construction of the dam sites. Fig. 3.1.12 depicts the dependence of the breakthrough time on the depth G of the grouting curtain. Breakthrough times increase steeply for grouting depths larger than the height H of the impounded water (150 meters in our scenarios).



All the parameters discussed so far describe the hydrological part of the problem. The following two parameters are connected with the chemistry of the impounded water. As already discussed we have assumed very low concentration of the water at the bottom of the reservoir. There is not enough information for the real chemical parameters of the water there.

Therefore, it is important to know the dependence of the T_B on different initial Ca concentrations. This dependence is plotted in Fig. 3.1.13. The ratio c_{in}/c_{eq} is depicted on the x-axis. Note that the scale of the y-axis is also linear. There is no significant influence of the c_{in}

on the breakthrough time for values lower than $0.5 c_{eq}$. However for values higher than $0.8 c_{eq}$ the breakthrough time is significantly increased.

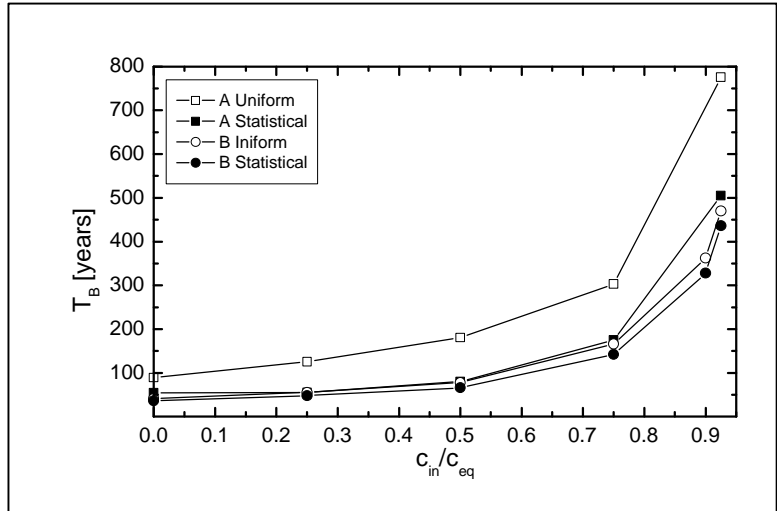


Fig. 3.1.13. Breakthrough times for Standard Scenarios A and B, in dependence on the calcium concentration of the impounded

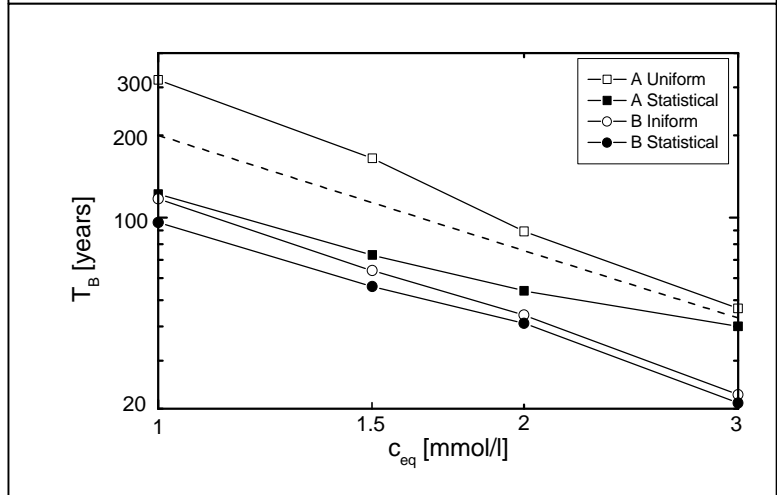


Fig. 3.1.14. Breakthrough times for Standard Scenarios A and B, in dependence on the equilibrium concentration of the impounded water c_{eq} .

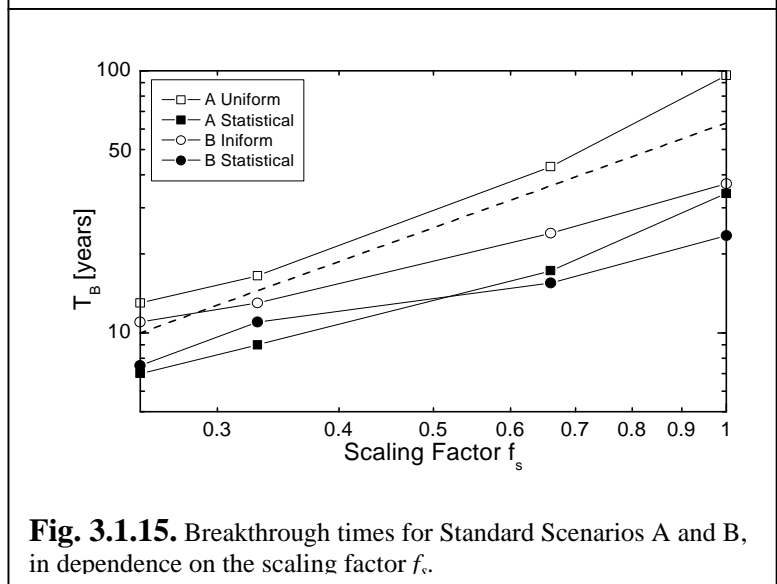


Fig. 3.1.15. Breakthrough times for Standard Scenarios A and B, in dependence on the scaling factor f_s .

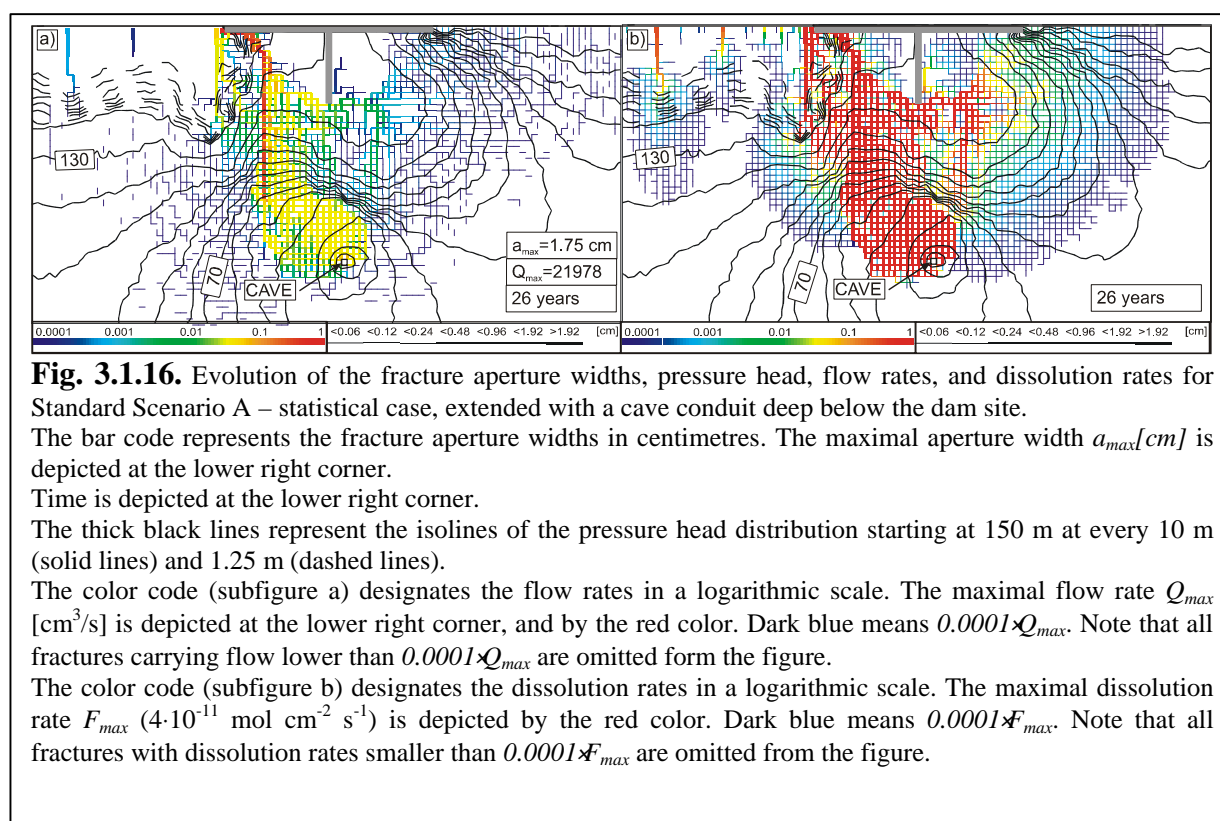
The other important chemical parameter is c_{eq} . For limestone it depends on the concentration of the CO_2 at the bottom of the reservoir. The dependence of the breakthrough time on this chemical parameter is depicted in Fig. 3.1.14. The dashed line shows that the breakthrough times follow a power law and are approximately proportional to $c_{eq}^{-1.4}$, similar to what has been reported for single conduits by Dreybrodt (1996) and for percolation networks by Siemers and Dreybrodt (1998).

We scale the values of the H , G and W with a common factor f_s . The reaction of the breakthrough time is depicted in Fig. 3.1.15. It shows the decrease of the breakthrough time with the decrease of the size of the structure. At $f_s=0.5$, breakthrough times are reduced to more than 50 % in comparison with the basic standard scenarios. For smaller structures, a deeper grouting curtain is necessary to prevent the fast karstification of the rock below. The dashed line depicts the power law

dependence of the breakthrough time on the ratio $(L^2/H)^{4/3}$, reported by Dreybrodt (1996) for single fractures, and by Siemers and Dreybrodt (1998) for percolation networks. In our scenario L is equal to $W+2G$. The conclusion is that scaling H , W and G with a common factor f_s , scales the breakthrough time by $(f_s)^{4/3}$. This is shown by the dashed line. This is in a way a surprising result, because it shows that smaller geometrically similar dam structures become unstable earlier in comparison with large dams.

3.1.7. Examples of different geological settings

The goal of the discussion so far was to describe the basic mechanisms governing the evolution of a karst aquifer under the boundary conditions of large hydraulic structures. This was the reason to try to simplify the setups of the models as much as possible. The goal of the following three examples will be to demonstrate the abilities of our programs to model scenarios closer to real geological settings.



We use the statistical case of the standard scenario A as a base. All the initial boundary conditions as well as the statistical net distribution are the same as in this scenario (see Table 3.1.1). In order to study the influence of a phreatic cave conduit below the dam, we introduce an area marked with a white square in Fig. 3.1.16. This area has constant head boundary condition valid for all its fractures. The value of this constant head is 0.1 meters. In this way

we are able to model a phreatic cave conduit, whose spring is somewhere downstream of the dam site.

The evolution of the aperture fracture widths, the flow rates, the dissolution rates and the pressure head distribution is depicted in Fig. 3.1.16 a, b. The meaning of the color and the bar code is:

Fig. 3.1.16a – the color code designates the flow rates in a logarithmic scale. The maximal flow rate Q_{max} is depicted by the red color. Dark blue means $0.0001 \times Q_{max}$. All fractures carrying flow smaller than $0.0001 \times Q_{max}$ are omitted from the figure.

Fig. 3.1.16b – the color code designates the dissolution rates in a logarithmic scale. The maximal dissolution rate F_{max} is depicted by the red color. Dark blue means $0.0001 \times F_{max}$. If the dissolution rate along the fracture is smaller than $0.0001 \times F_{max}$, then the fracture is omitted from the figure.

The bar code is the same for all subfigures of Fig. 3.1.16. It depicts the aperture width of the fracture, in centimeters. Note that even sufficiently widened fractures can be omitted from the figure if the flow through them or the dissolution rate at their exit is too small.

The thick black lines represent the hydraulic head distribution – at every 1.25 meters (dashed line) and every 10 meters (full lines).

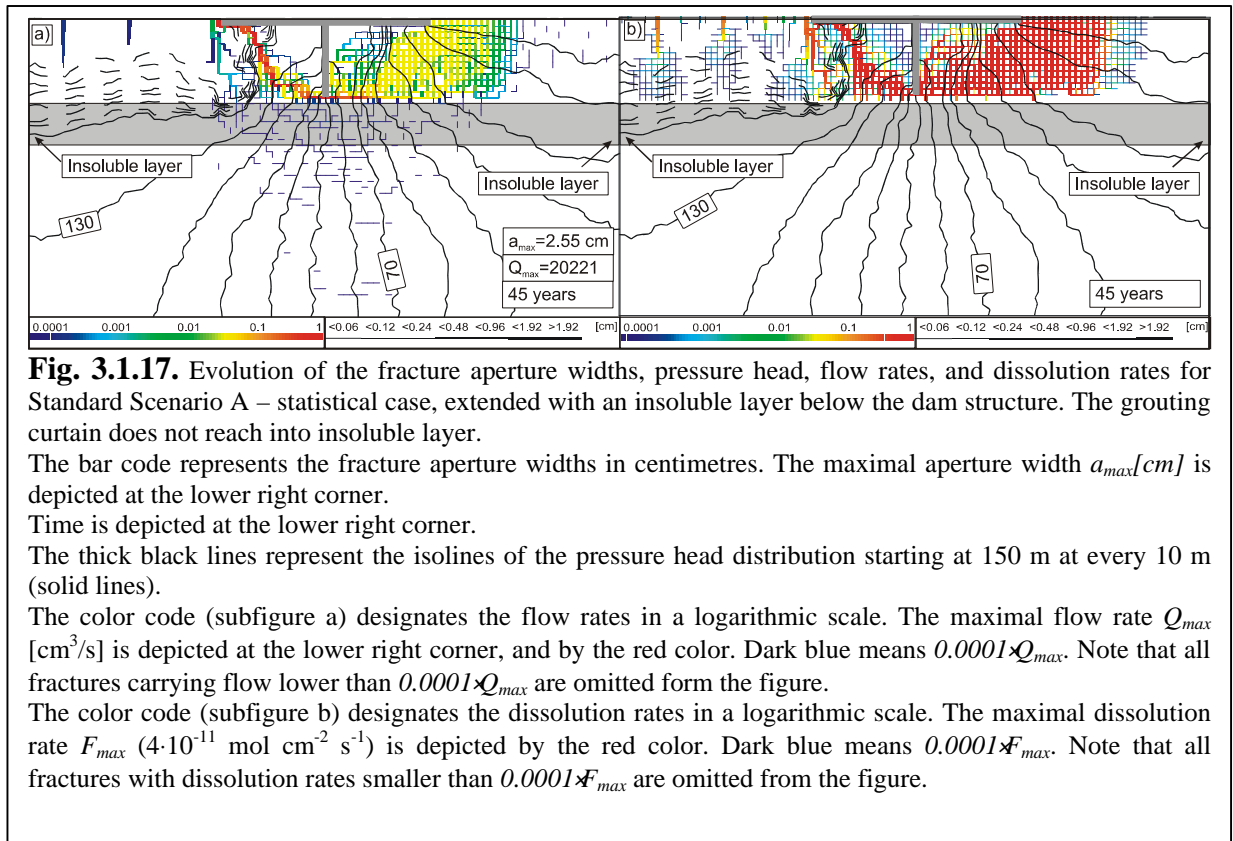
The figure depicts the situation after 26 years of evolution. Similar to the standard cases, a vertical channel starts its growth from the bottom of the reservoir parallel to the grouting curtain. In this case however after its division into two channels, the vertical one continues to grow in the direction to the cave. The second one is growing below the dam site structure and is directed towards the exit. This route was already discussed. The position of the cave favors the evolution of the vertical branch and after 26 years it is connected with the cave. This is the moment of the breakthrough for the system. It is 16 years earlier in comparison with the breakthrough time of the statistical case of scenario A. This is a decrease of almost 30%. The presence of cave conduits in the area close to the dam site structure can significantly reduce the evolution time for the system dam site – soluble rock below it. This causes unbearable leakage rates earlier than estimated. The leakage rate for this scenario is depicted by the red curve on Fig. 3.1.19.

In order to simulate the influence of different layers of rock, with different dissolutional properties, we introduce a horizontal layer of insoluble rock extending from the left hand side boundary of the domain, below the dam, to the right hand side boundary. The thickness of this layer is 67.5 meters. Everything else remains exactly like in the statistical case of the standard scenario A. We discuss two cases.

In the first one the grouting curtain does not reach the layer.

The evolution of the aperture fracture widths, the flow rates, the dissolution rates and the pressure head distribution is depicted in Fig. 3.1.17 a, b.

Because of the small soluble fringe between the tip of the grout and the insoluble layer, the evolution is similar to the statistical case of the standard scenario A. The evolution of the leakage rates is depicted by the blue curve on Fig. 3.1.19. Even the presence of an insoluble



layer cannot change significantly the evolution of the dam site system, if the grouting curtain does not penetrate into this insoluble layer.

The next example has the same setup as the previous one. The only difference is that the grouting curtain is reaching into the insoluble layer.

The evolution of the aperture fracture widths, the flow rates, the dissolution rates and the pressure head distribution is depicted in Fig. 3.1.18 a, b. The meaning of the color and the bar code is as before.

The evolution of the system in this scenario is quite different. Because of the insoluble layer, widening of pathways is blocked. Widening of fractures occurs only above this layer and also below it. The insoluble layer cannot be affected during the whole evolution time. Therefore, the flow through the layer is limited, and no matter what happens with the network

above it, there will be no breakthrough event. This is also depicted by the green curve of the leakage rate in Fig. 3.1.19.

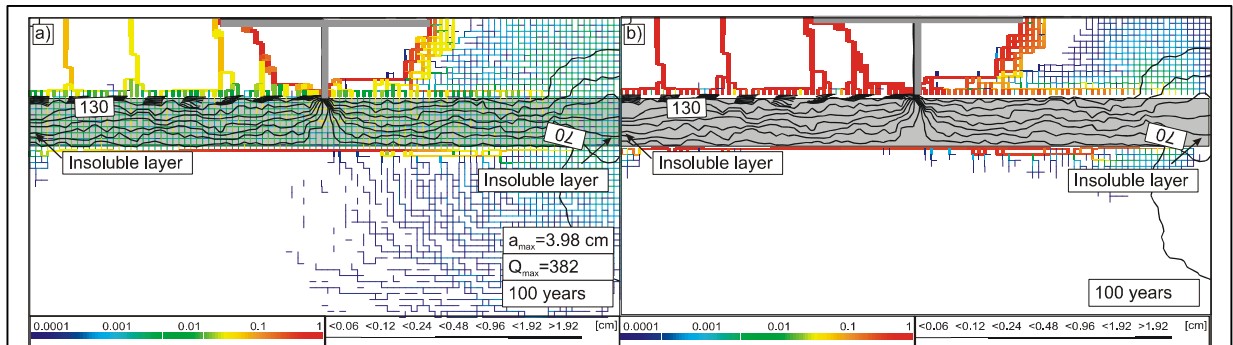


Fig. 3.1.18. Evolution of the fracture aperture widths, pressure head, flow rates, and dissolution rates for Standard Scenario A – statistical case, extended with an insoluble layer below the dam structure. The grouting curtain reaches down into the layer.

The bar code represents the fracture aperture widths in centimetres. The maximal aperture width $a_{max}[cm]$ is depicted at the lower right corner.

Time is depicted at the lower right corner.

The thick black lines represent the isolines of the pressure head distribution starting at 150 m at every 10 m (solid lines).

The color code (subfigure a) designates the flow rates in a logarithmic scale. The maximal flow rate Q_{max} [cm^3/s] is depicted at the lower right corner, and by the red color. Dark blue means $0.0001 \times Q_{max}$. Note that all fractures carrying flow lower than $0.0001 \times Q_{max}$ are omitted from the figure.

The color code (subfigure b) designates the dissolution rates in a logarithmic scale. The maximal dissolution rate F_{max} ($4 \cdot 10^{-11} \text{ mol cm}^{-2} \text{ s}^{-1}$) is depicted by the red color. Dark blue means $0.0001 \times F_{max}$. Note that all fractures with dissolution rates smaller than $0.0001 \times F_{max}$ are omitted from the figure.

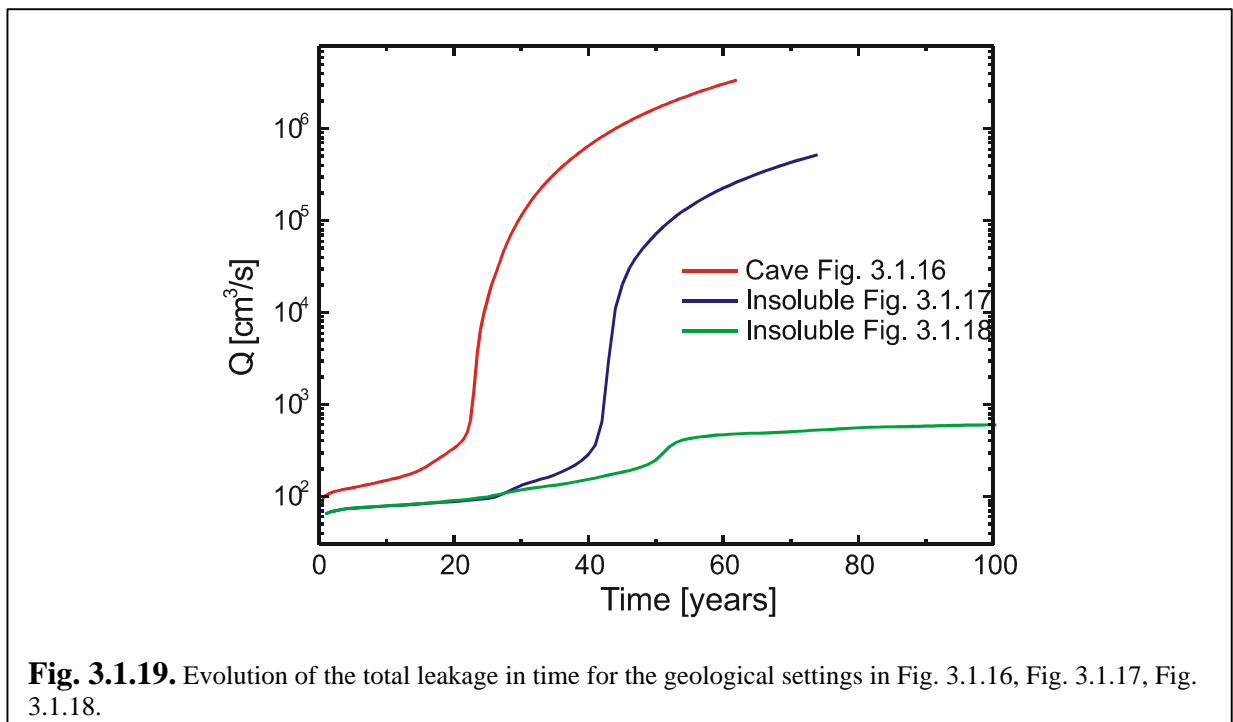


Fig. 3.1.19. Evolution of the total leakage in time for the geological settings in Fig. 3.1.16, Fig. 3.1.17, Fig. 3.1.18.

3.1.8. Effect of mixing corrosion on the evolution of a dam site

Mixing corrosion can influence the evolution only in the cases of initial Ca concentration of the impounded water close to saturation. The scales of the evolution of a

system governed mainly by mixing corrosion are in the order of several ten thousands to hundred thousands years (see next chapter). Therefore mixing corrosion can alter the evolution of a dam site system only in cases, when the evolution of the dam system itself takes times longer than several hundred years. This is not the topic of our research and can be a possible subject of the future work. Recently Kaufman (2003) reports some results on the influence of the mixing corrosion on the evolution of a dam site, which confirm such timescales.

3.1.9. Conclusion

A model of karstification under unnatural boundary conditions was presented. These conditions are characterized by high hydraulic heads, steep hydraulic gradients and relatively short pathways from the input to the output in limestone and gypsum terrains. Such conditions exist at dam sites, but also at some other hydraulic structures, e.g. impounding water in a cave system by blocking the outflows (Milanovic, 2000).

Our model scenario simulates the initial conductivity of the soluble rock block, by a fracture network with average aperture widths in the order of 10^{-2} cm. This is highly idealized. Nevertheless, nets with fracture aperture widths of 0.02 cm and spacing of 10 meters correspond to hydraulic conductivities of $8 \cdot 10^{-7}$ m s⁻¹, which is not an unrealistic value in natural karst terrains.

The main result from our model runs is that the discussed man made initial and boundary conditions cause the increase of the leakage rates of dam sites. Sometimes this increase is so fast that it can endanger the stability of the structures within a period of several years.

We have presented models of very simple scenarios in order to get an idea of the basic processes governing the evolution of the dam site system. On the other hand we are able to change the properties of every single fracture comprising our model networks. This enables us to simulate complicated geological situations. But a detailed knowledge of the geology of the modeled region is needed then.

The goal of this work is not to give exact values of the life times of dam sites. The results presented here cannot be directly transferred to real dams with similar geometrical properties. Our goal is to give some scales of the impact, which a man made large hydraulic structure can have on the surrounding environment. Our results confirm the basic laws discovered by the use of one-dimensional models, but also show the influence of the surrounding network, which sometimes can be significant. To build 3D models of hydraulic structures, and to study in details the influence of the exchange of flow between the growing

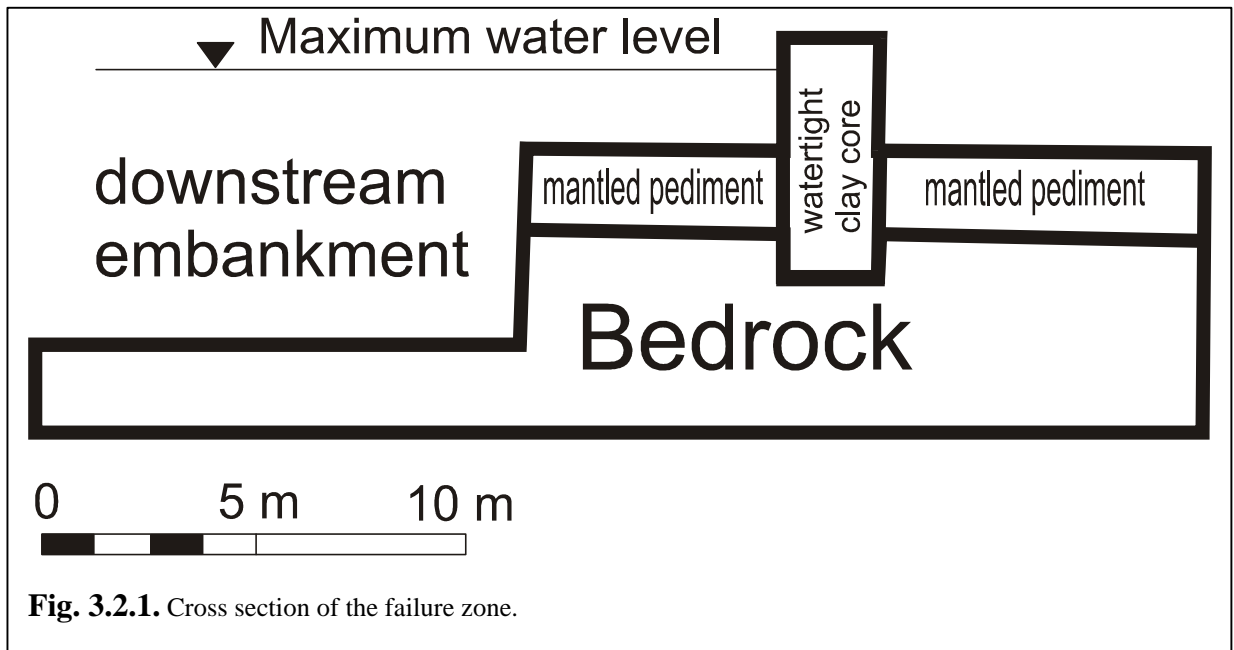
channels and the unaffected part of the modeled soluble rock block is an interesting topic for a future research. In 3-D models exchange flow can be enhanced and, consequently, breakthrough times may decrease significantly.

3.2. Modeling of a catastrophic failure of the San Juan reservoir (NE Spain).

3.2.1. Modeling domain.

Gutierrez et al. (2002) analyze the causes for a catastrophic failure of the San Juan reservoir. The reservoir was built in 1999 on gypsiferous mantled pediment deposits overlaying Tertiary dispersive clay sediments. An earth dam was constructed on the pediment surface along the perimeter of the artificial basin. The core of the dam is compacted clay material derived from the excavation. The core is indented 1m in the Tertiary shales of the bedrock, cutting the highly pervious mantle of gypsiferous deposits (40 % gypsum). The earth dam is 6m wide at the top. The maximum depth of the basin is 19m. It is designed to host a water column of up to 17.5m. The capacity of the reservoir is 850 000 m³. The geometry of the reservoir is a “sheared rectangle” with curved apexes of around 400m long and 230m wide. A cross section is presented on Fig. 3.2.1. For more details about the reservoir and the geological settings of the area see Gutierrez et al. (2002).

In order to model the impact of karstification processes on the safety of this dam structure, we create the modeling domain presented by Fig. 3.2.2. It is a rectangular network,



comprised by 201 horizontal and 125 vertical fractures. The spacing between the fractures is 20 cm. The green fractures, depict the area of the low permeable core of the dam. The orange ones depict the highly permeable pediment, and the yellow – the low permeable bedrock (see Fig. 3.2.2.). The blue zone marks for the water column.

The hydraulic boundary conditions are as follows:

- Constant head boundary condition at the upstream side of the dam, depicted by the thick dark blue line – $H=17.5m$;
- Constant head boundary condition at the downstream side of the dam, depicted by the light blue line – $h=9m$;
- The left hand side, the right hand side and the bottom of the domain are impervious (thick black lines on Fig. 3.2.2).

3.2.2. Numerical results

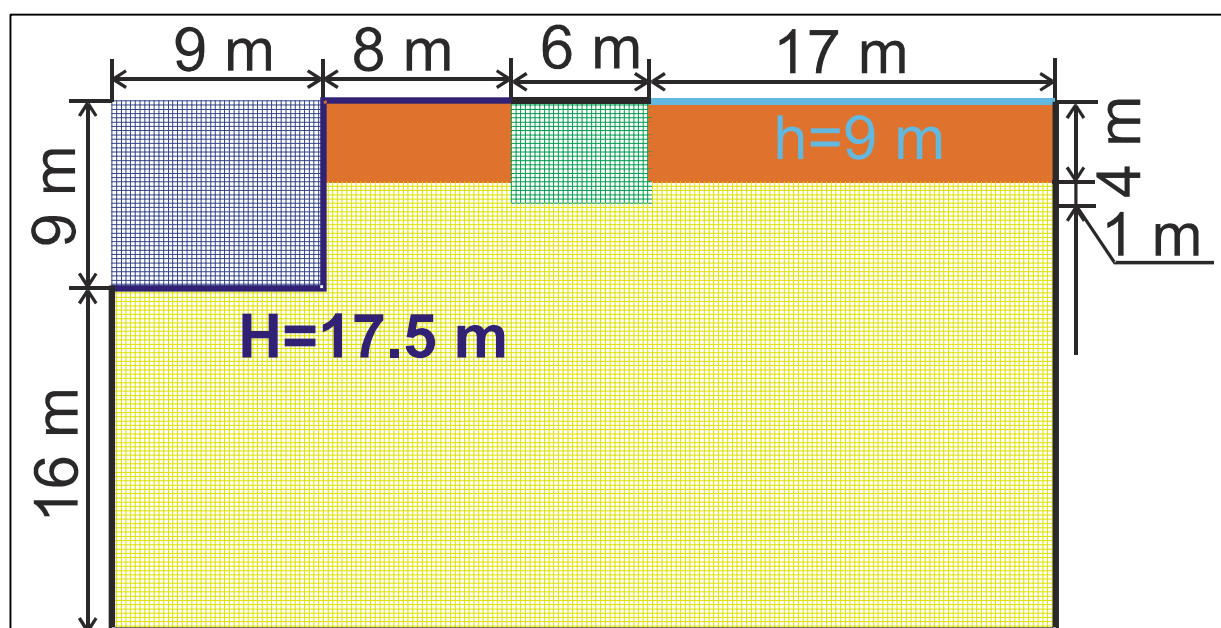


Fig. 3.2.2. Model domain of the San Juan reservoir.

The blue zone depicts the impounded water. A constant head at 17.5 along the boundary depicted by the thick dark blue line.

The constant head is at 9 m at the downstream side of the dam, depicted by the light blue line.

The orange zone represents the soluble mantle pediment.

The green zone shows the clay core penetrating 1 m into the bedrock (depicted by the yellow zone).

The thick black lines represent the impervious boundaries.

We have studied several scenarios. The hydraulic boundary conditions are the same for all of them (see section 3.2.1). The initial values for the hydraulic conductivities of the core, and the bedrock are varied. The values are presented by Table 3.2.1. Dissolution is allowed for the mantled pediment, but not for the bedrock and the clay core. Only for Scenario 2 we assume that dissolution also is active in the clay core.

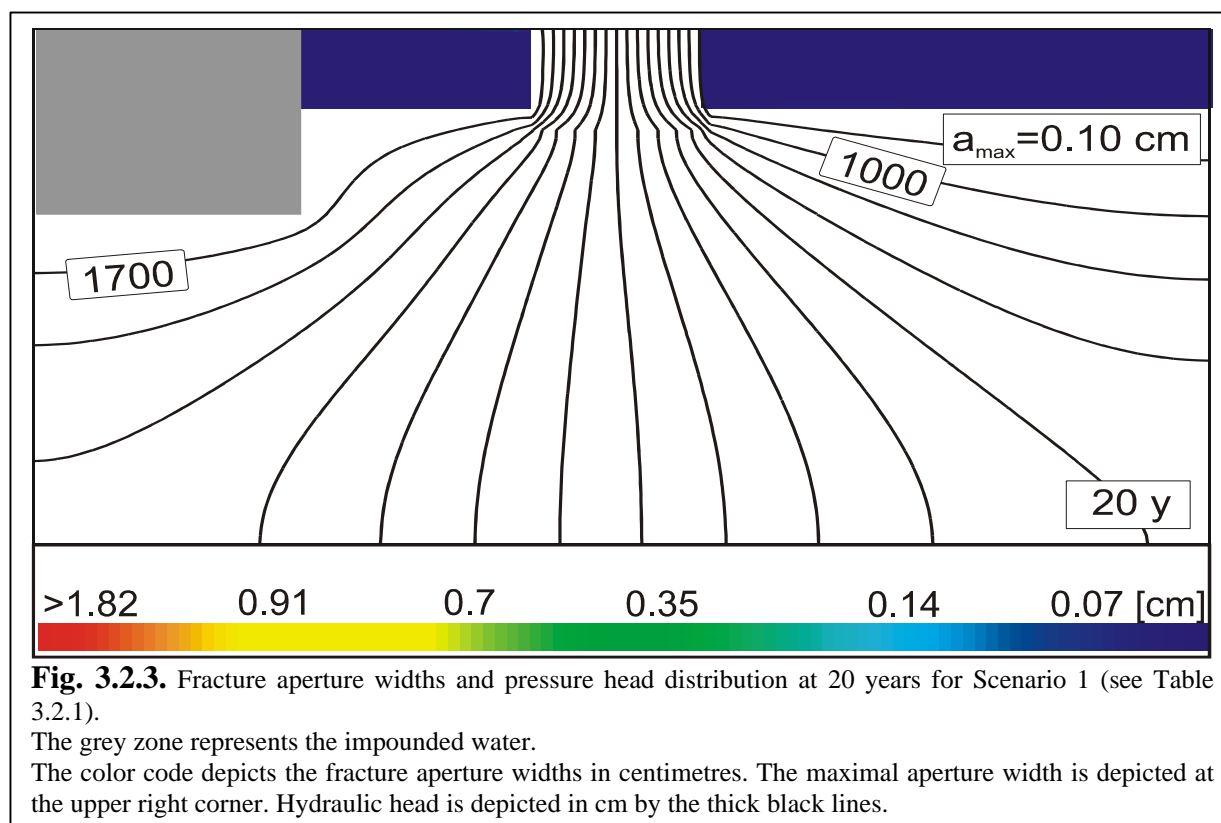
The hydraulic conductivity of the pediment is in the range of 10^{-1} cm/s for all experiments.

We start with Scenario 1. In this case the core is assumed as impervious, and the hydraulic conductivity of the bedrock is lower by one order of magnitude with respect to the other scenarios (see Table 3.2.1). Fig. 3.2.3 depicts the fracture aperture widths and the pressure head distribution at the end of the calculations (20 years). One can see that there is almost no change in the gypsum pediment.

This is not the case for Scenarios 2 and 3. The core is assumed pervious (hydraulic conductivity 10^{-5} cm/s), and the hydraulic conductivity of the bedrock is by one order of magnitude higher (10^{-4} cm/s) than for Scenario 1. One can see that the differences with respect to Scenario 1 are considerable. There is a widened channel growing along the left hand side of the clay core (see Fig. 3.2.4 and Fig. 3.2.5). At the same time another zone of widening is observed at the base of the pediment on the downstream side of the structure. The aperture widths of the fractures comprising these areas are almost 2 cm.

Element	Hydraulic conductivity [cm/s]	Initial aperture width [cm]	Type of the network
Scenario 1			
Core	0	$1e^{-5}$	Uniform
Pediment	10^{-1}	0.07	Uniform
Bedrock	10^{-5}	0.0035	Uniform
Scenario 2			
Core	10^{-5}	0.0035	Uniform
Pediment	10^{-1}	0.07	Uniform
Bedrock	10^{-4}	0.0078	Uniform
Scenario 3			
Core	10^{-5}	0.0035	Uniform
Pediment	10^{-1}	0.07	Uniform
Bedrock	10^{-4}	0.0078	Uniform
Scenario 4			
Core	10^{-4}	0.0078	Uniform
Pediment	10^{-1}	0.07	Uniform
Bedrock	10^{-4}	0.0078	Uniform
Scenario 5			
Core	10^{-4}	0.0078	Uniform
Pediment	10^{-1}	0.07	Uniform
Bedrock	10^{-4}	0.0078	Statistical ($\sigma=0.01$)
Scenario 6			
Core	10^{-4}	0.0078	Statistical ($\sigma=0.01$)
Pediment	10^{-1}	0.07	Statistical ($\sigma=0.01$)
Bedrock	10^{-4}	0.0078	Statistical ($\sigma=0.01$)

Table 3.2.1. Basic parameters of the dam structure for the modelling scenarios



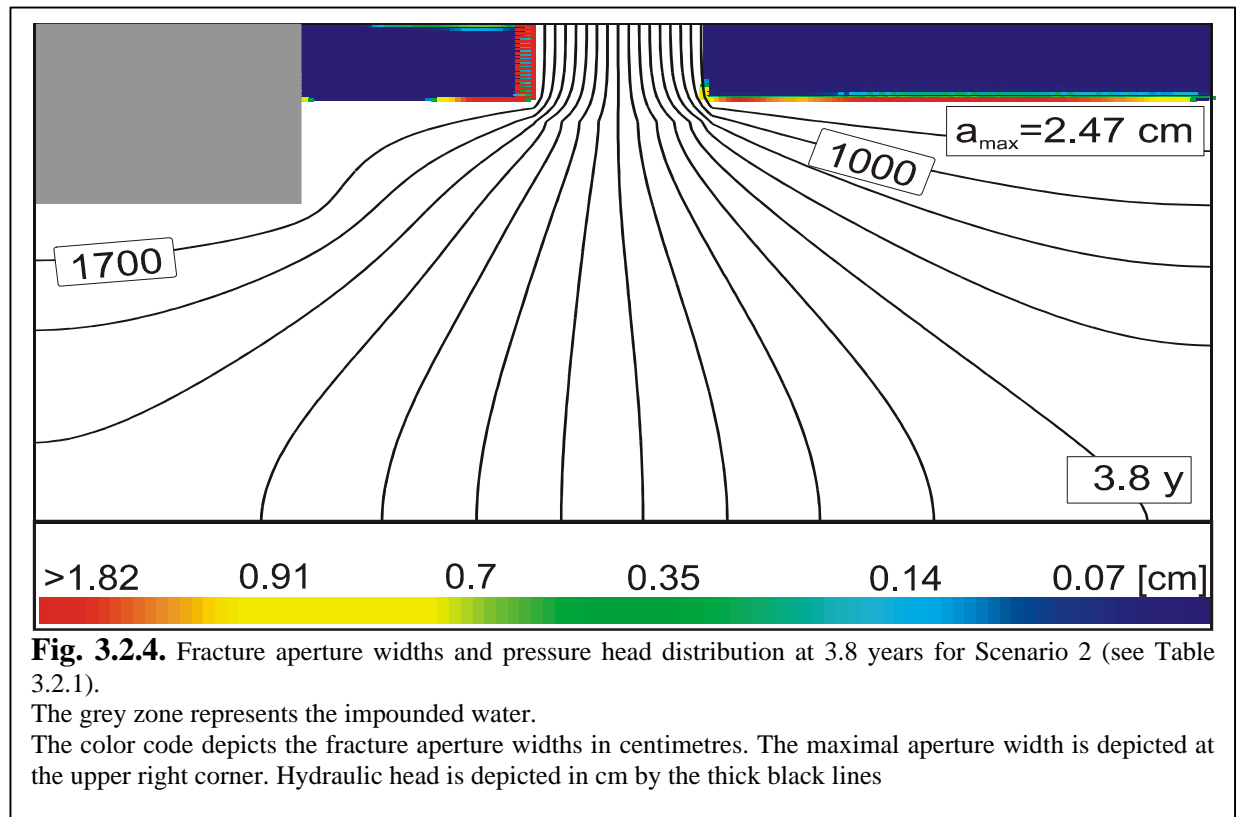
The difference between Scenario 2 and Scenario 3 is, that we assume, that the clay core contains soluble material for Scenario 2. Therefore some of its primary fissures can be widened. Because of the low aperture widths, the water flowing through the soluble fissures becomes quickly saturated. Therefore the time scale for considerable changes in the core is extremely long and we will not discuss this effect further.

The hydraulic conductivity of the clay core is increased for Scenarios 4, 5, and 6. It is the same as the hydraulic conductivity of the bedrock (10^{-4} cm/s). The differences between these scenarios (4, 5 and 6) are the initial distribution of the fracture aperture widths. They are:

- Uniform for the pediment, the bedrock, and the core (Scenario 4);
- Statistical for the bedrock and uniform for the pediment and the core (Scenario 5);
- Statistical for the pediment, the bedrock and the core (Scenario 6).

See Table 3.2.1 for the numerical values.

Fig. 3.2.6, Fig. 3.2.7, and Fig. 3.2.8 depict the aperture width and the pressure head distributions for Scenario 4, Scenario 5, and Scenario 6, respectively.



One can see that together with the channels observed for Scenario 2 and Scenario 3, there is a third considerably widened pathway along the right hand side of the clay core. The aperture widths of the fractures comprising these pathways are in the range 2 – 2.5 cm. These channels needed less than two years to develop in Scenarios 4, 5, and 6.

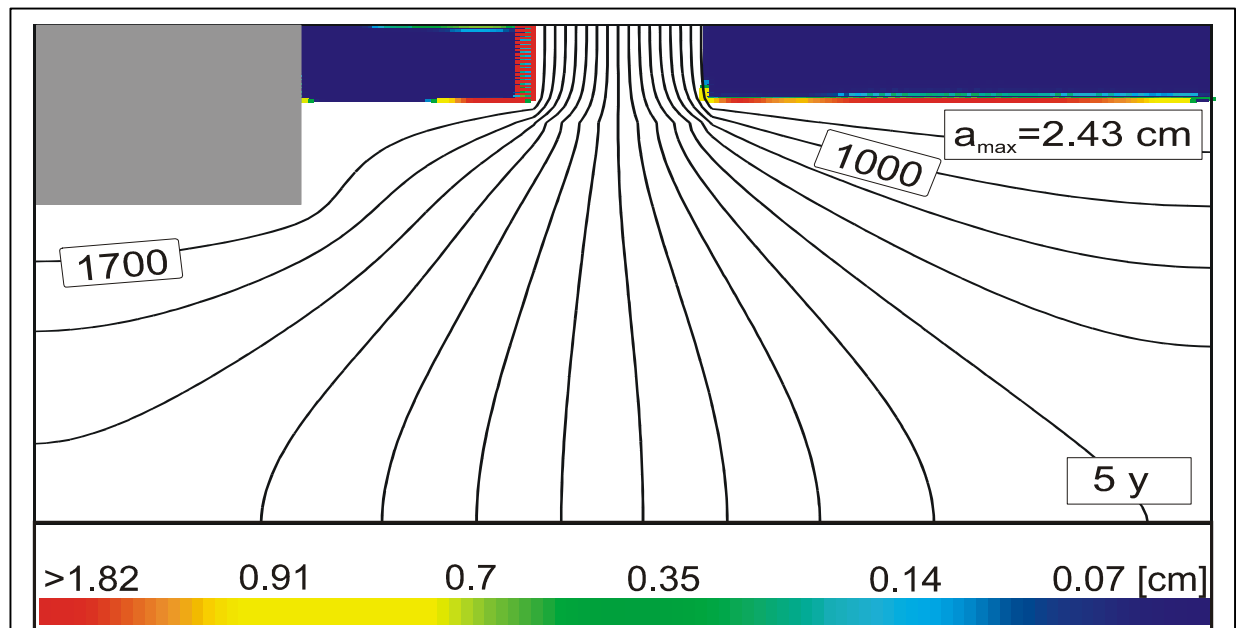


Fig. 3.2.5. Fracture aperture widths and pressure head distribution at 5 years for Scenario 3 (see Table 3.2.1).

The grey zone represents the impounded water.

The color code depicts the fracture aperture widths in centimetres. The maximal aperture width is depicted at the upper right corner. Hydraulic head is depicted in cm by the thick black lines.

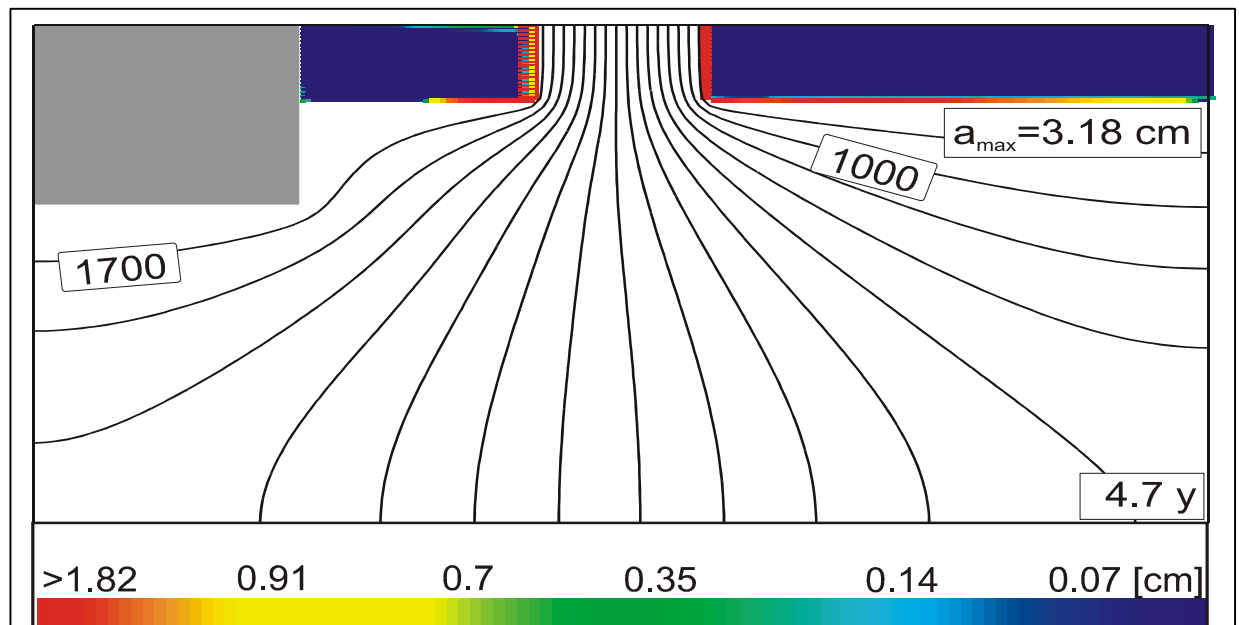


Fig. 3.2.6. Fracture aperture widths and pressure head distribution at 4.7 years for Scenario 4 (see Table 3.2.1).

The grey zone represents the impounded water.

The color code depicts the fracture aperture widths in centimetres. The maximal aperture width is depicted at the upper right corner. Hydraulic head is depicted in cm by the thick black lines.

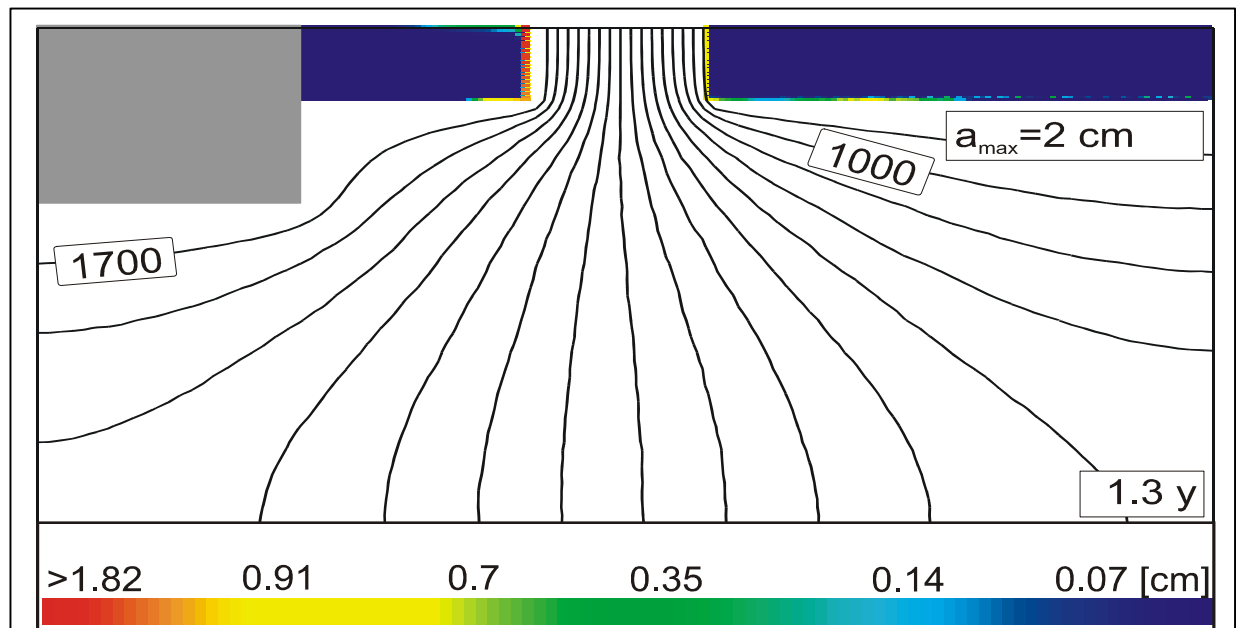


Fig. 3.2.7. Fracture aperture widths and pressure head distribution at 1.3 years for Scenario 5 (see Table 3.2.1).

The grey zone represents the impounded water.

The color code depicts the fracture aperture widths in centimetres. The maximal aperture width is depicted at the upper right corner. Hydraulic head is depicted in by the thick black lines.

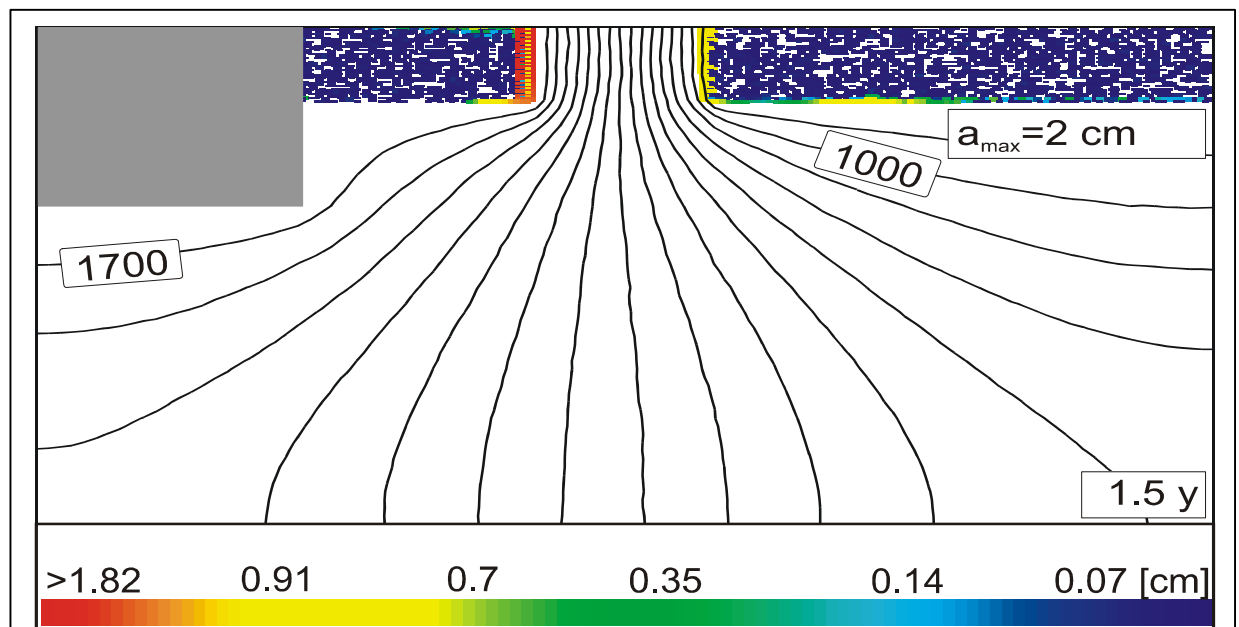


Fig. 3.2.8. Fracture aperture widths and pressure head distribution at 1.5 years for Scenario 6 (see Table 3.2.1).

The grey zone represents the impounded water.

The color code depicts the fracture aperture widths in centimetres. The maximal aperture width is depicted at the upper right corner. Hydraulic head is depicted in cm by the thick black lines

3.2.3. Conclusion

The goal of the presented study was to draw attention to the importance of the karstification processes for the failure of the San Juan reservoir. The presented results show that the quality of the compaction of the clay core, together with the geological settings of the bedrock, are of crucial importance for the safety of the structure. The dam can be considered as safe, if the core is impervious (Scenario 1, Fig. 3.2.3), and the bedrock has a relatively low hydraulic conductivity. On the other hand, if we increase the conductivity of the bedrock by one order of magnitude, and assume that the core is permeable, then the structure of the core can become mechanically unstable. This takes several years for Scenarios 2 and 3, and less than 2 years for scenarios 4, 5, and 6.

The conclusion of the case study performed by Gutierrez et al. (2002) is, that the failure of the San Juan reservoir is caused by several reasons.

- a) Dissolution of gypsum in the pediment deposit;
- b) Piping processes that affect the embankments and the core of the dam.

Our results are in agreement with these conclusions, and show the ability of our model to simulate realistic geological situations.

4. The influence of the chemical boundary conditions on the evolution of karst aquifers

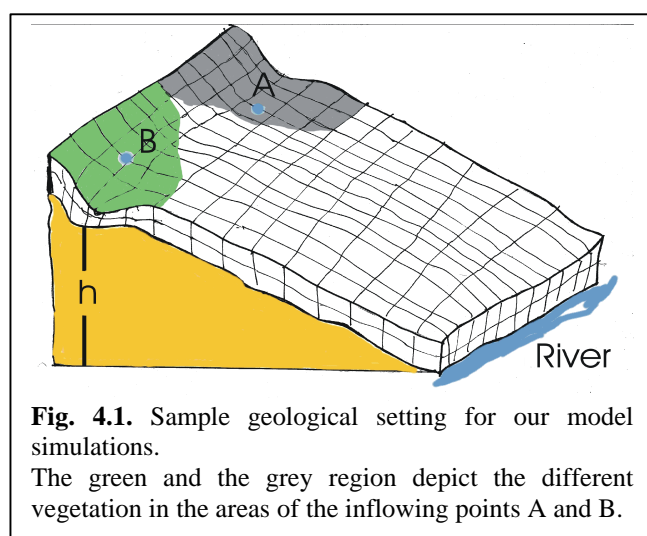
Our goal so far, was to study the influence of the exchange flow on the evolution of a simple karst aquifer. Therefore the interaction between two hydrological systems (wide fracture embedded into a fine fracture network) was studied. Two different types of initial and boundary conditions control the evolution of these systems:

- a) The hydrological ones are for example the values of the initial aperture widths of the fractures, the geometry of the domain, and the hydraulic head on the borders of the aquifer.
- b) The chemical boundary conditions characterize the chemical composition of the solution flowing through the aquifer.

The influence of the hydrological parameters was already discussed in details (see Chapter 2 and 3). Our next step is to investigate the impact of the chemical boundary conditions. Therefore we study the evolution of a model karst aquifer under fixed hydrological and variable chemical boundary conditions.

4.1. Basic settings

The chemical composition of the solution entering at different input points has a significant impact on the evolution. The equilibrium chemistry of the system $\text{H}_2\text{O} - \text{CO}_2 -$



CaCO_3 , and its reaction kinetics determine this evolution from the initial state to the maturity (Dreybrodt, 1988). CO_2 - containing water is driven through the fractures and dissolves CaCO_3 . Complete studies on the influence of these boundaries for the case of a single fracture are presented in the following works: Dreybrodt (1996), Dreybrodt and Gabrovsek (2000), Gabrovsek (2000).

Siemers and Dreybrodt (1998), Siemers (1998) and Dreybrodt and Siemers (2000) discuss this for karst aquifers modeled with 2D percolation networks.

As a base of our model we use the geological setup depicted on Fig. 4.1. It is a simple confined karst aquifer consisting of a limestone bed, with two inputs at constant head and open flow conditions along the entire width at base level. The areas, where the input points are located, have different vegetation. Therefore the chemical compositions of the solutions entering the modeled aquifer are different. If there is a zone where the inflowing solutions mix, an increased aggressivity is observed due to the non-linearity of the Ca – CO₂ equilibrium curve, see Fig. 4.2. This effect is called Mixing Corrosion. For the first time it is described in 1939 by Laptev. In 1964 and 1980 Bögli stresses the importance of mixing corrosion as a cave forming mechanism. Dreybrodt (1981) shows that cave conduits can grow when two solutions

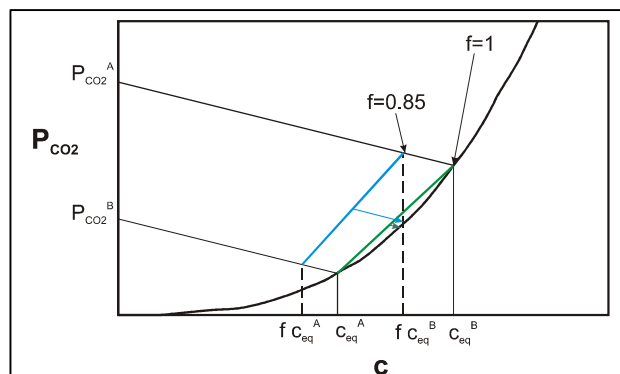


Fig. 4.2. Chemical pathways of the inflowing solutions. – closed system with respect to CO₂. For $f=1$ the input concentrations are saturated with respect to calcite. Where they mix they become undersaturated with respect to calcite and regain dissolutive power – the green line. For $f \neq 1$ the entering solutions are undersaturated, but also regain dissolutive power, when they mix – the cyan curve.

saturated with respect to calcite with different equilibrium concentrations mix along an intersection of fractures. Gabrovsek and Dreybrodt (2000) show that mixing corrosion and non-linear kinetics considerably enhance the process of karstification for a confluence of two fractures injecting water with differing equilibrium concentrations into a third outflow fracture. They apply these results to a 2D percolation network with two input points, with solutions entering at zero calcium concentration but differing P_{CO2}.

Mixing corrosion creates a zone of increased permeability in the region where the solutions mix. In a recent study, Kaufmann (2003) discusses the effect of the mixing corrosion on the evolution of karst aquifers in natural and artificial environments.

The goal of the current study is to investigate the action of the Mixing Corrosion, referred further as MC, more systematically. A refined modeling technique taking into account the statistical distribution of the fracture aperture widths allows better spatial resolution. Furthermore, we systematically investigate the influence of the input calcium concentration. In order to show the impact of the MC on the evolution of the aquifer, we will discuss the following cases:

- a) The input solutions are chemically equal ($c_{eq}^A = c_{eq}^B$). In this case MC is not active. The evolution of the aquifer under constant head boundary condition exhibits breakthrough (BT) behavior. The channels developing from the input

point downstream to the exit of the domain characterize this evolution scenario. The time scale of this process depends on the input hydrological and chemical boundary conditions. As already noted the hydrological boundaries are fixed for all the scenarios discussed in this chapter. Consequently the evolution of the aquifer depends only on chemical boundary conditions at the inputs. If the input Ca concentration is low with respect to c_{eq} then, as already discussed in Chapter 1, a positive feedback mechanism determine the evolution of the aperture widths of the fractures. The dissolution rates at their outputs increase with the increase of the aperture width there (see Eq. 1.15 and Eq. 1.16). In this case, the initial widening and the initial flow through the fractures is low, but they increase steadily until breakthrough. At this moment the flow rate increases by orders of magnitude and the dissolution rate at the output is close to that at the input. We estimate the breakthrough time of a single fracture, using Eq. 1.21 (Gabrovsek, 2000). All scenarios, discussed in the second chapter, depict typical breakthrough behavior. If the input Ca concentration is close to c_{eq} then the positive feedback mechanism is switched off. In this case the permeability of the aquifer increases slowly in time and even in space. The time scale for such type of evolution is in the range of several hundred thousands to millions of years (Dreybrodt and Gabrovsek 2000).

- b) The second case is: The input solutions are chemically different ($c_{eq}^A \neq c_{eq}^B$) but saturated with respect to calcite. In contrast to the BT case, dissolutional widening occurs only in the areas where the input solutions mix. This means that deep inside the domain the solution becomes undersaturated with respect to calcite (see Fig. 4.2), and it is able to widen the fractures there. Consequently a zone of lower permeability is created. The time scale of this evolution depends on the differences in the P_{CO_2} and respectively c_{eq} of the inflowing solutions.
- c) Together with the extreme cases, we study some intermediate scenarios. MC is active, and at the same time the concentration with respect to calcite of the inflowing solution is varied. The parameter f depicts the ratio c_{in}^i/c_{eq}^i at both inputs ($i=A,B$, see Fig. 4.1). The increase of the dissolutional power after mixing of two solutions undersaturated with respect to calcite is depicted on Fig. 4.2 (cyan line and values). In order to investigate the switch between BT

and MC governed evolution, we vary the value of f in the range $0.75 - 1$. For $f < 0.96$ the feedback mechanism is still active. A typical breakthrough type of evolution is expected. For $f > 0.96$ the feedback mechanism is switched off. Time scales for the evolution become longer. MC gains influence and the BT behavior is suppressed.

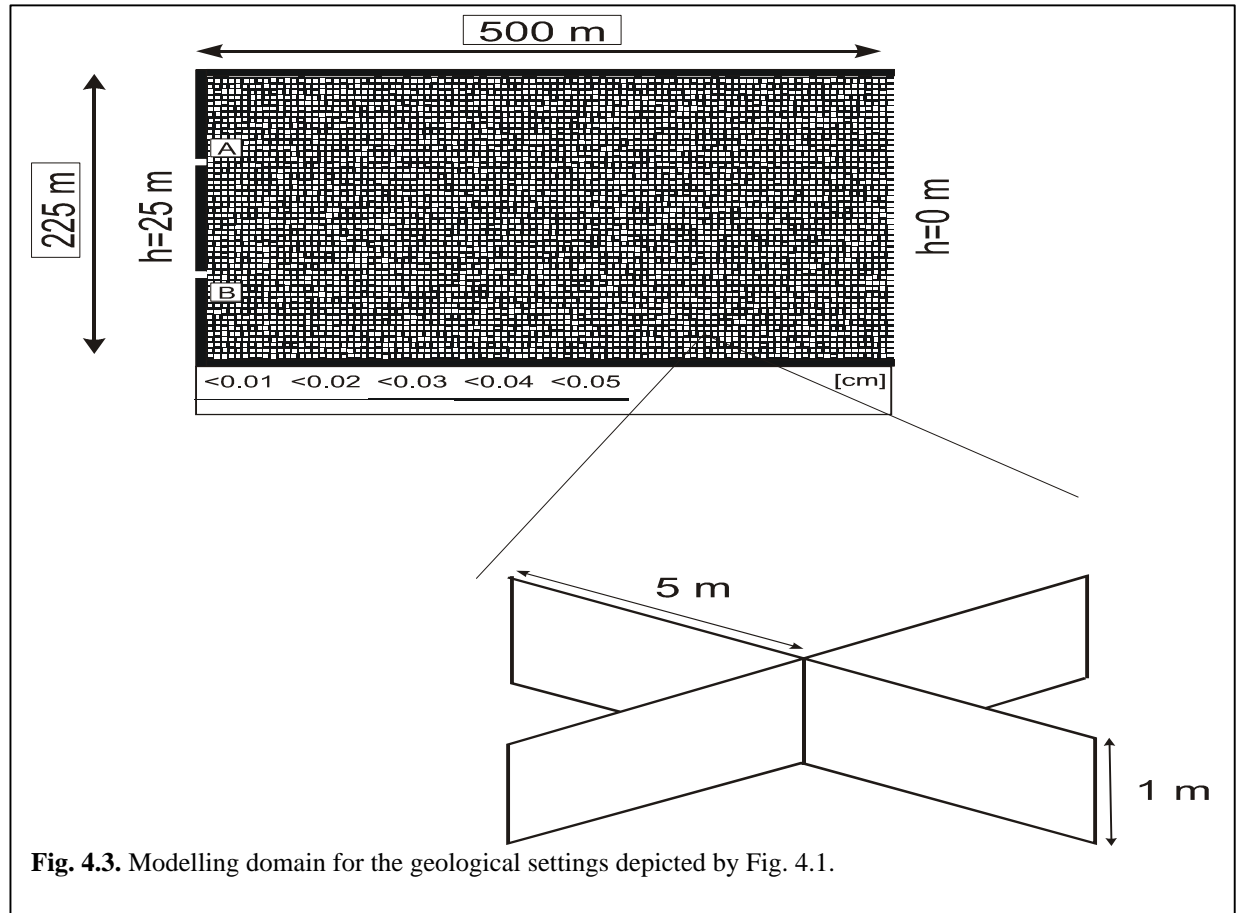


Fig. 4.3. Modelling domain for the geological settings depicted by Fig. 4.1.

Fig. 4.3 depicts the idealized modeling domain (see Fig. 4.1). It consists of a limestone bed 1m in depth, 500 meters long, 255 meters wide. A rectangular fracture network is embedded into the limestone masif. It divides it into blocks of 5m x 5m x 1m. In all scenarios discussed in this chapter we will use only networks with statistical distribution of the initial aperture widths a_0 of their fractures. A lognormal distribution with average at $a_0=0.015$ cm and $s=0.01$ is used. Fig. 4.3 depicts the initial distribution of the aperture widths (see the bar code). There are two input points (A and B) at the impermeable left hand side of the domain. The upper and the lower boundaries are also impermeable, as indicated by the black rim. As already mentioned the hydraulic initial conditions are kept fixed for all the scenarios discussed in this chapter. Therefore the realization of the lognormal distribution is the same for all scenarios. A constant head of $h=25$ meters is applied at the input points A and B. The right hand side of the domain is open to flow at head $h=0$.

4.2. Numerical results

4.2.1. Evolution dominated by BT

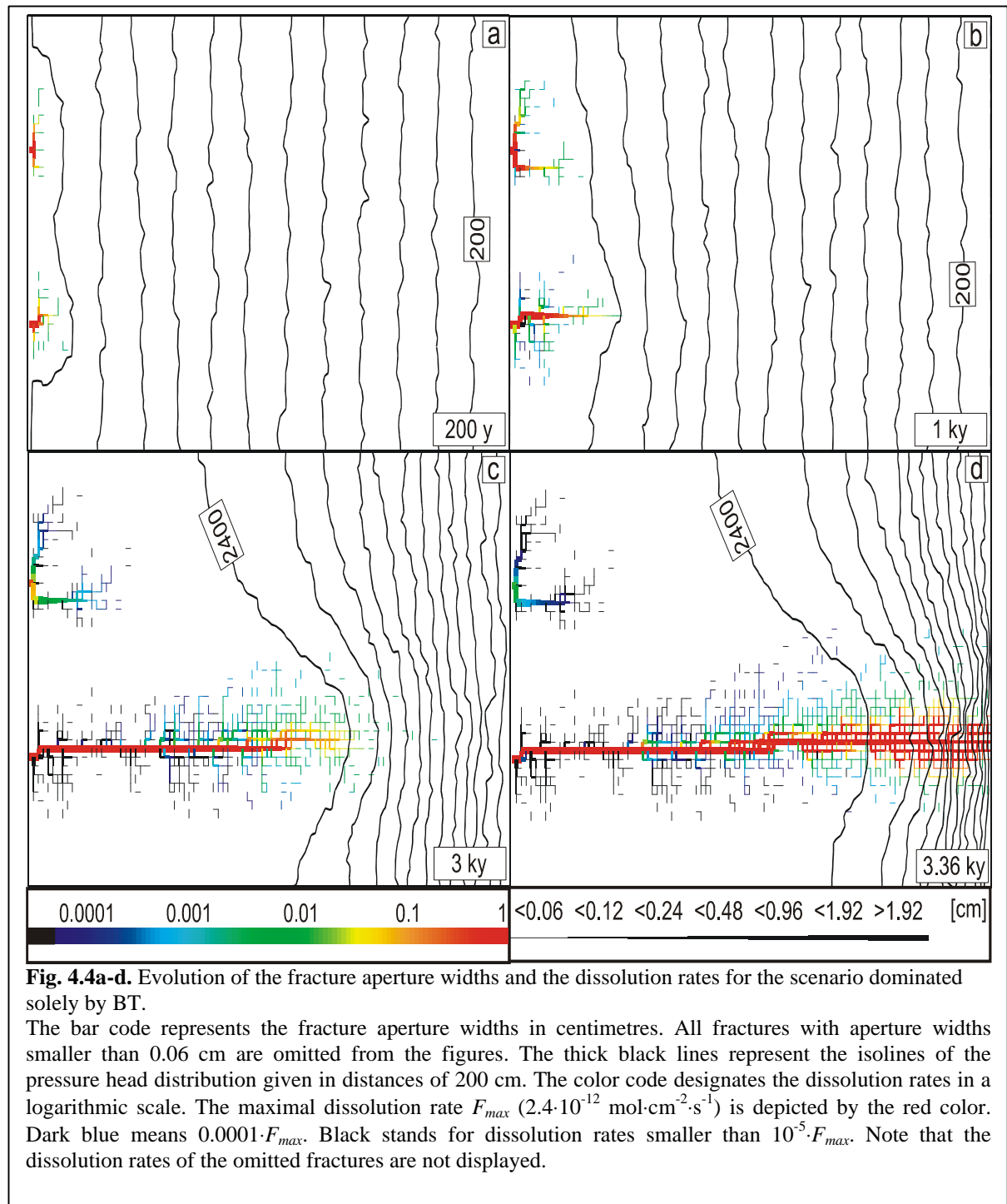
We start the discussion with the two extreme cases. The first one has the following initial chemical parameters:

$$P_{\text{CO}_2}^{\text{A}}=P_{\text{CO}_2}^{\text{B}}=0.05 \text{ atm};$$

$$c_{\text{in}}=0.75c_{\text{eq}} \text{ (f=0.75)};$$

$$c_{\text{eq}}=2.14 \cdot 10^{-6} \text{ mol cm}^{-3}.$$

Its evolution is depicted in Fig. 4.4 a-d. The thick black lines represent the isolines of the pressure head distribution given in distances of 200 cm. All fractures with aperture widths smaller than 0.06 cm are omitted from the pictures. The idea is to show the regions where dissolution has a strong effect. Note that the bar code, representing the fracture aperture widths, is not the same as in Fig. 4.3. The colors designate the dissolution rates in a logarithmic scale. The maximal dissolution rate F_{max} is depicted by the red color. Dark blue means $0.0001 \cdot F_{\text{max}}$. Black stands for dissolution rates smaller than $10^{-5} \cdot F_{\text{max}}$. Note that the dissolution rates of the omitted fractures are not displayed. In other words, the fact that a fracture is omitted does not necessary mean that the dissolution rate along it is low.



Since the inflowing solutions at both input points (A, B) are chemically equal, MC is not active. On the other hand, the input concentration is considerably lower than c_{eq} . Therefore, a typical breakthrough behavior is expected. Fig. 4.4a depicts the situation after 200 years. Flow radiates out from the input points and after several ten meters is distributed evenly downstream towards the output. This is visible from the pressure head distribution. As expected, two channels start to grow from the input points. They propagate downstream until one of them reaches the output. This will be the moment of the breakthrough event. Fig. 4.4b shows that after 1000 years of evolution both channels have continued to grow further in the

direction to the output. These channels do not evolve downstream with the same speed. Some parts of the domain have initially higher permeability, because of the statistical distribution of the fracture aperture widths. Flow is attracted towards these areas and consequently the direction of the channel's growth can be diverted. This is depicted by Fig. 4.4b. Because of the initially wider fractures on its way, the channel at the lower input grows almost horizontally towards the exit. This is not the case for the upper channel. It is visible that the fractures on its way are not wide enough to attract the flow. Therefore the channel is split into two parts growing upwards and downwards parallel to the left hand side boundary. These small details give an advantage to the lower channel, which reaches the output first. This competition is depicted in Fig. 4.4c. It shows the evolution stage at 3000 years. The lower channel has penetrated deeply further, while the upper one has not changed significantly. Its growth is blocked by the redistribution of the pressure head caused by the lower conduit. Only 360 years later the lower channel has reached the output (Fig. 4.4d). This is the moment of breakthrough. After this event the dissolution rates become even along the whole open channel. This, and the clearly visible exit type fan are typical for a BT type evolution, already discussed in the first chapter and by Siemers and Dreybrodt (1998), Gabrovsek (2000), and Dreybrodt and Siemers (2000).

4.2.2. Evolution dominated by MC

Fig. 4.4 e-h depicts the evolution of the second extreme case. The input chemical parameters are:

$$P_{CO_2}^A = 0.05 \text{ atm},$$

$$P_{CO_2}^B = 0.01 \text{ atm},$$

$$c_{in}^O c_{eq} (f=1).$$

$$c_{eq}^A \neq c_{eq}^B.$$

The solution at both entry points is saturated with respect to calcite. It is not aggressive to the rock and cannot widen the fractures. This changes the evolution of the aquifer. Because of the chemically different solutions, MC is active, where they mix. Fig. 4.4e shows the situation after 10000 years. The pressure head distribution is similar to the one depicted in Fig. 4.4a. Two regions are visible.

The first one starts from the left hand side boundary and extends downstream to about 100 meters. The flow coming from both entry points radiates out as can be seen by the head lines. There is a zone where the input solutions mix and activate MC. The dissolution rates are maximal in this region. The red channel, growing downstream horizontally, depicts this zone.

As water flows downhill it loses its dissolutive power. At the same time it enters the second zone of the pressure distribution. The flow there is dispersed downstream toward the

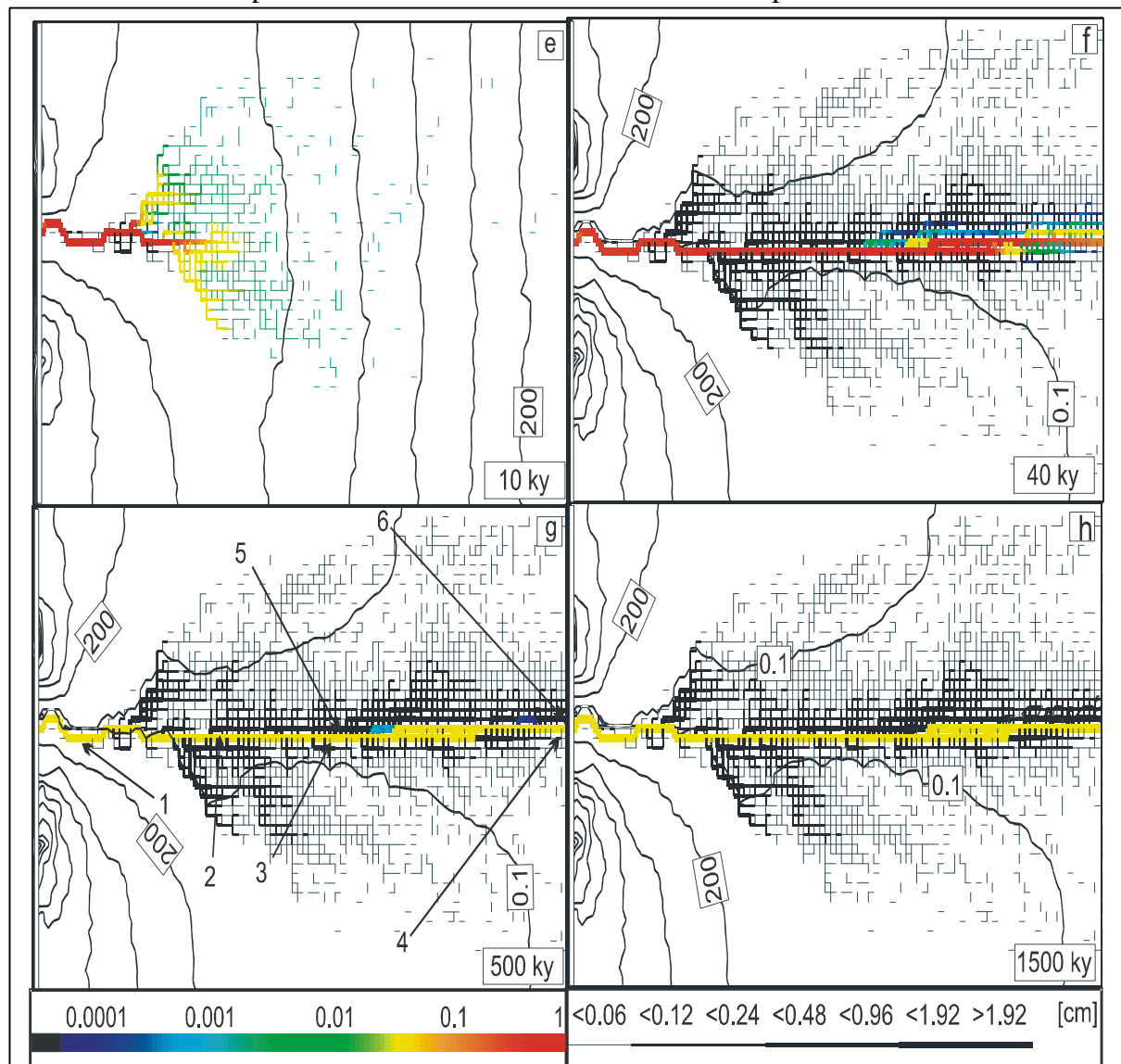


Fig. 4.4e-h. Evolution of the fracture aperture widths and the dissolution rates for the scenario dominated solely by MC.

The bar code represents the fracture aperture widths in centimetres. All fractures with aperture widths smaller than 0.06 cm are omitted from the figures. The thick black lines represent the isolines of the pressure head distribution given in distances of 200 cm. The color code designates the dissolution rates in a logarithmic scale. The maximal dissolution rate F_{max} ($1.39 \cdot 10^{-13} \text{ mol} \cdot \text{cm}^{-2} \cdot \text{s}^{-1}$) is depicted by the red color. Dark blue means $0.0001 \cdot F_{max}$. Black stands for dissolution rates smaller than $10^{-5} \cdot F_{max}$. Note that the dissolution rates of the omitted fractures are not displayed.

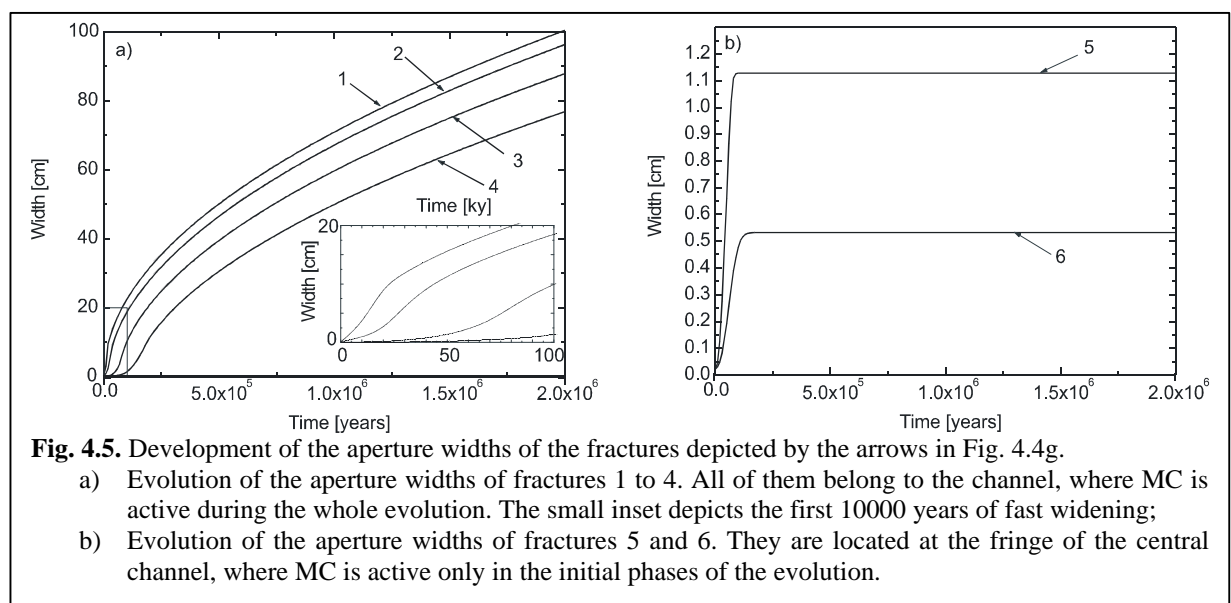
The numbered arrows depict the fractures, whose aperture width evolution is presented in Fig. 4.5 (see text).

output. The wide green-blue zone depicts this region. The dissolution rates there are two to three orders of magnitude lower than in the mixing zone and they decrease downstream.

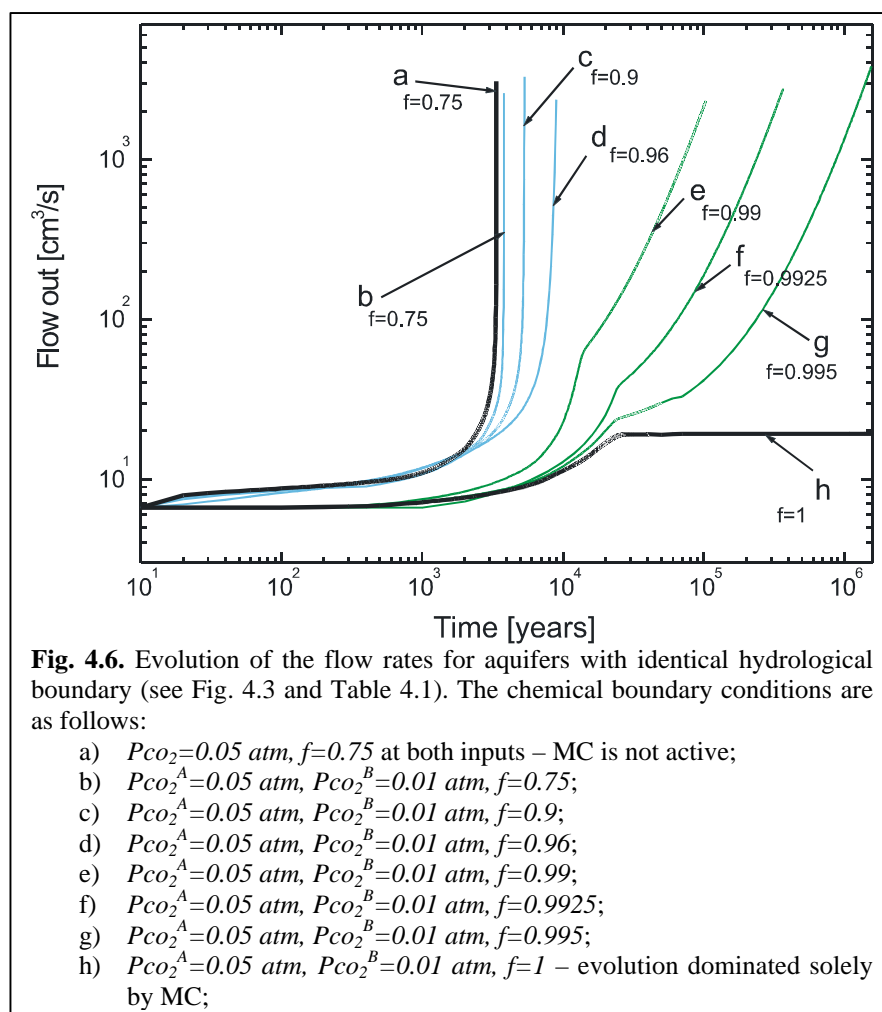
Figure 4.4e depicts the situation after 10000 years, and this is still an early stage of the evolution. The whole evolution of the pure BT case (Fig. 4.4 a-d) took only 4000 years. This means that the time scale in the case governed solely by mixing corrosion is several orders of magnitude longer. Fig. 4.4f depicts the situation after 40000 years. The widened horizontal

channel has reached base level. In the case of pure MC no breakthrough event occurs, but the flow rates increase continuously. The dissolution rates are maximal and even along the channel. Almost the whole amount of flow is directed towards it and is mixed along its entire length. This is depicted also by the pressure head distribution. The $h=0.1$ cm isoline, which is practically the base level, extends along the conduit. When the widened channel has reached the exit widening in the fracture network is reduced by four orders of magnitude. The only zone, which is still active, is the central channel. This is depicted by the black fractures on both sides of the channel. The dissolution rates along them are practically zero. These fractures had active widening only for the time period before the main channel had reached the base level. Afterwards the head is redistributed in the way depicted in the figure (Fig. 4.4f) and dissolutional widening is restricted only along the central conduit. It continues to widen evenly along its length and linear in time. This is visible also in the figures depicting the evolution stage after 500 ky and 1500 ky (Fig. 4.4g, h). There is no other change in the network except the widening of the central pathway. This is another proof that the exit type fan is a feature belonging to the BT type of evolution. It cannot develop in the case of MC governed evolution, because the flow of the aggressive solution is restricted to the central channel. Although the flow field at the entrance part of the domain is favorable for the growth of entry fans, these cannot develop because of the high input calcium concentration. The reason is that the feedback mechanism is switched off if the concentrations are so high. Consequently, none of the fractures on both sides of the central conduit is able to experience a local breakthrough event. Therefore, the fan cannot develop. For details about the mechanisms supporting the growth of entry and exit fans see Chapter 2.

Let us have a closer look at the evolution of the aperture widths of some fractures



belonging to different areas of the domain. The arrows and the numbers on Fig. 4.4g depict their positions. Fractures 1 to 4 belong to the central active pathway. Fig. 4.5a depicts their widening in time. Fracture number 1 starts to grow first, because it is the closest to the entrance. Fractures 2 to 4, located further downstream, start to grow later in the sequence of their locations. In all cases the growth rates are high initially and then after 1 million years become constant. The small inset at the left border of the picture depicts the first 100 000 years of fast widening. After 1 million years the aperture widths are almost 50 cm. They continue to increase linearly in time, with a rate of about 30 centimeters per million years.



a) Fig. 4.5b depicts the evolution of fractures 5 and 6. In the beginning they belong to the mixing zone, or at least to the zone of the outflow from the mixing zone, and are widened quickly. After 40 000 and 80 000

years (40 000 years is close to the moment when the central channel has reached the output) they stop to develop. The pressure head distribution does no longer allow mixing outside of the widened channel. The aperture widths at this moment are about 1 centimeter for fracture 5 and 0.5 cm for fracture 6, respectively. All fractures depicted in black in Fig. 4.5 e-h have a similar evolution.

To compare the evolution of the two extreme scenarios (BT and MC), Fig. 4.6 (curve a and curve h – the black ones) depicts the flow out through the right hand side border of the

aquifer for the two discussed cases. Curve a shows a slow change in the flow during the initial stages of the evolution, and then a sudden increase marking breakthrough. This is a typical BT behavior. The situation for the case governed only by MC behavior is entirely different (curve h). It was already discussed that the dissolution is active only along the zones of mixing. These zones are widened and their permeability increases. They can carry more flow. The widening of these areas is marked by the increasing part of the curve (Fig. 4.6, curve h). As soon as the widened zone has reached the base level, the pressure heads are redistributed, and the dissolution becomes active only along the central channel (see Fig. 4.4e-h). On the other hand the areas around the input points are not widened, because they have never belonged to a mixing zone. This means, that no matter how wide the central channel is, these entrance zones limit the amount of water entering the domain. This is depicted by the flat constant part of curve h, which also marks the moment when the central conduit has reached base level.

In conclusion: There are two entirely different modes of karstification. The first mode is governed by the breakthrough mechanism. It is fast and connects the input point with the output of the domain. The mode governed by the MC is extremely slow and creates channels deep inside the aquifer. There is no widened connection with the entry point. The aperture width of the evolved channel is in the range of a meter after several millions years. Hydrological boundary conditions are the same for both studied cases, but the difference in the hydrochemical boundaries is the reason for the different modes of evolution.

The discussion so far required detailed plots of the discussed figures. Therefore Fig. 4.4 was presented in two parts (Fig. 4.4a-d and Fig. 4.4e-h). The whole figure is presented once again on the next page. By this way, one is able to compare both scenarios directly. We will do the same for Fig. 4.7.

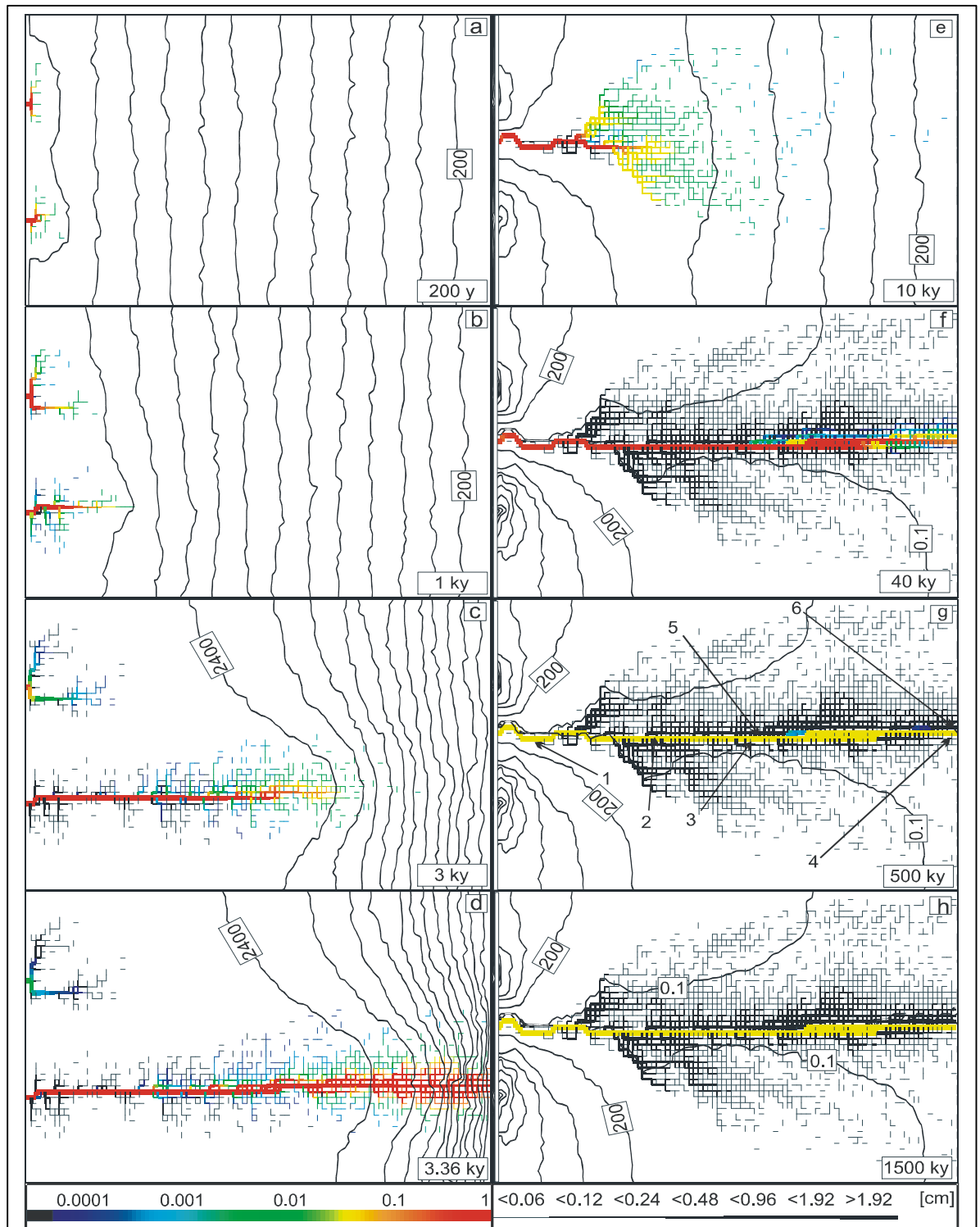


Fig. 4.4. Evolution of the fracture aperture widths and the dissolution rates for both scenarios BT (a-d) and MC (e-h) dominated. To make the direct comparison easier, we present the whole figure once again. The bar code represents the fracture aperture widths in centimetres. All fractures with aperture widths smaller than 0.06 cm are omitted from the figures. The thick black lines represent the isolines of the pressure head distribution given in distances of 200 cm. The color code designates the dissolution rates in a logarithmic scale. The maximal dissolution rate F_{max} ($2.4 \cdot 10^{-12} \text{ mol} \cdot \text{cm}^{-2} \cdot \text{s}^{-1}$ – subfigures a-d; $1.39 \cdot 10^{-13} \text{ mol} \cdot \text{cm}^{-2} \cdot \text{s}^{-1}$ – subfigures e-h) is depicted by the red color. Dark blue means $0.0001 \cdot F_{max}$. Black stands for dissolution rates smaller than $10^{-5} \cdot F_{max}$. Note that the dissolution rates of the omitted fractures are not displayed.

4.2.3. Intermediate cases (both MC and BT are active)

Our next goal is to study the situation between these two extreme cases. Therefore we combine the BT and the MC mode in the following scenario. The chemical properties of the solution at the upper entrance are:

$$P_{\text{CO}_2}^{\text{A}}=0.05 \text{ atm},$$

$$c_{\text{eq}}^{\text{A}}=2.14 \cdot 10^{-6} \text{ mole cm}^{-3},$$

$$c_{\text{in}}=0.75 \cdot c_{\text{eq}} \text{ (f=0.75)}.$$

The composition at the lower one is:

$$P_{\text{CO}_2}^{\text{B}}=0.01 \text{ atm},$$

$$c_{\text{eq}}^{\text{B}}=0.55 \cdot 10^{-6} \text{ mole cm}^{-3}$$

$$c_{\text{in}}=0.75 \cdot c_{\text{eq}} \text{ (f=0.75)}.$$

Fig. 4.7 a-d depicts the evolution of the aquifer. The situation at 400 years is similar to the one of the pure BT governed case. Two conduits start their growth from the entry points downstream towards the exit of the domain. The water from the lower input is less aggressive and, consequently, the channel there is shorter than the upper one. See Fig. 4.7a. The pressure head distribution depicts the region where both inflowing solutions mix. In contrast to the situation discussed for the pure BT case, several fractures have widened along the mixing zone. This zone attracts flow now and changes the evolution of the aquifer. Fig. 4.7b depicts the situation after 1000 years. The upper channel grows in two directions. The first branch evolves in the direction to the exit of the domain. It grows along the same fractures as the upper channel in the pure BT controlled case. On the other hand, the second branch of the upper channel grows towards the area widened by the action of the MC. This branch is more competitive than the upper one because it grows in the zone of fractures already widened by the MC. Consequently, it needs less time to reach the base level. This is depicted on Fig. 4.7 c – 3000 years of evolution. The lower branch has penetrated deeper into the aquifer than the other competitive channels. 800 years later, it reaches the base level. See Fig. 4.7d. There is a clearly visible exit type fan confirming the BT type evolution of the aquifer.

The conclusions from the study of the first intermediate scenario are:

- a) BT is the main mechanism governing the evolution of this aquifer;
- b) MC is capable to change the direction of the growth of the breakthrough channels;

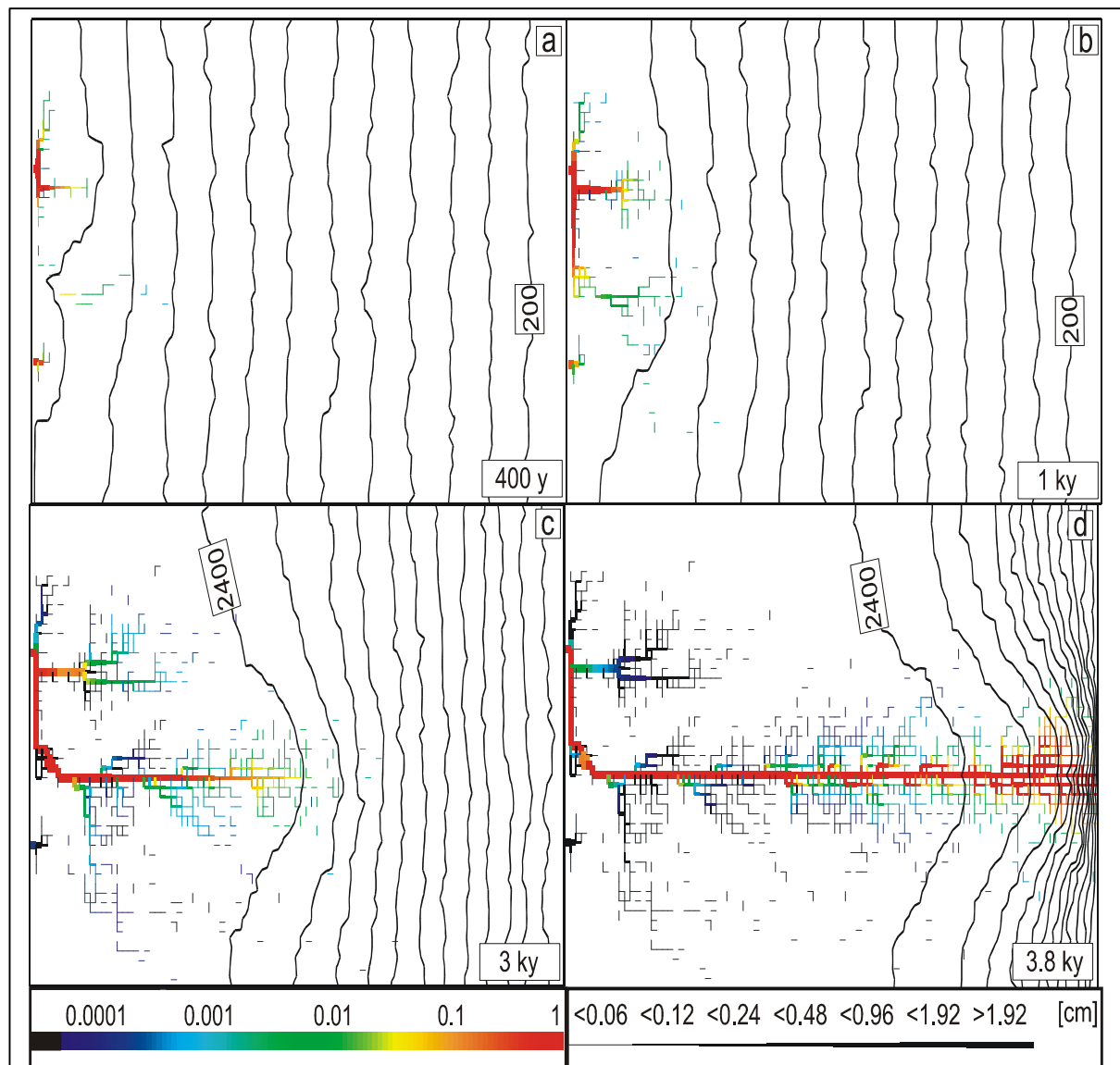


Fig. 4.7a-d. Evolution of the fracture aperture widths and the dissolution rates for a scenario with the following chemical boundary conditions:

$Pco_2^A=0.05\ atm, Pco_2^B=0.01\ atm, f=0.75;$

The bar code represents the fracture aperture widths in centimetres. All fractures with aperture widths smaller than 0.06 cm are omitted from the figures. The thick black lines represent the isolines of the pressure head distribution given in distances of 200 cm. The color code designates the dissolution rates in a logarithmic scale. The maximal dissolution rate F_{max} ($2.4 \cdot 10^{-12}\ mol \cdot cm^{-2} \cdot s^{-1}$) is depicted by the red color. Dark blue means $0.0001 \cdot F_{max}$. Black stands for dissolution rates smaller than $10^{-5} \cdot F_{max}$. Note that the dissolution rates of the omitted fractures are not displayed.

This confirms first investigations by Gabrovsek and Dreybrodt (2000) and Gabrovsek (2000).

As already discussed the influence of the BT mode should decrease with the increasing values of the input concentrations. Several scenarios are studied. The parameter f has the following values: 0.75 (this case was already discussed), 0.9, 0.96, 0.99, 0.9925, and 0.995.

The evolution of the aquifer for the case closest to the pure MC case is depicted in Fig. 4.7 e-h. The input chemical parameters are:

$$P_{CO_2}^A = 0.05 \text{ atm}, c_{in}^A = 0.995 \cdot c_{eq}^A,$$

$$P_{CO_2}^B = 0.01 \text{ atm}, c_{in}^B = 0.995 \cdot c_{eq}^B.$$

$$f = 0.995$$

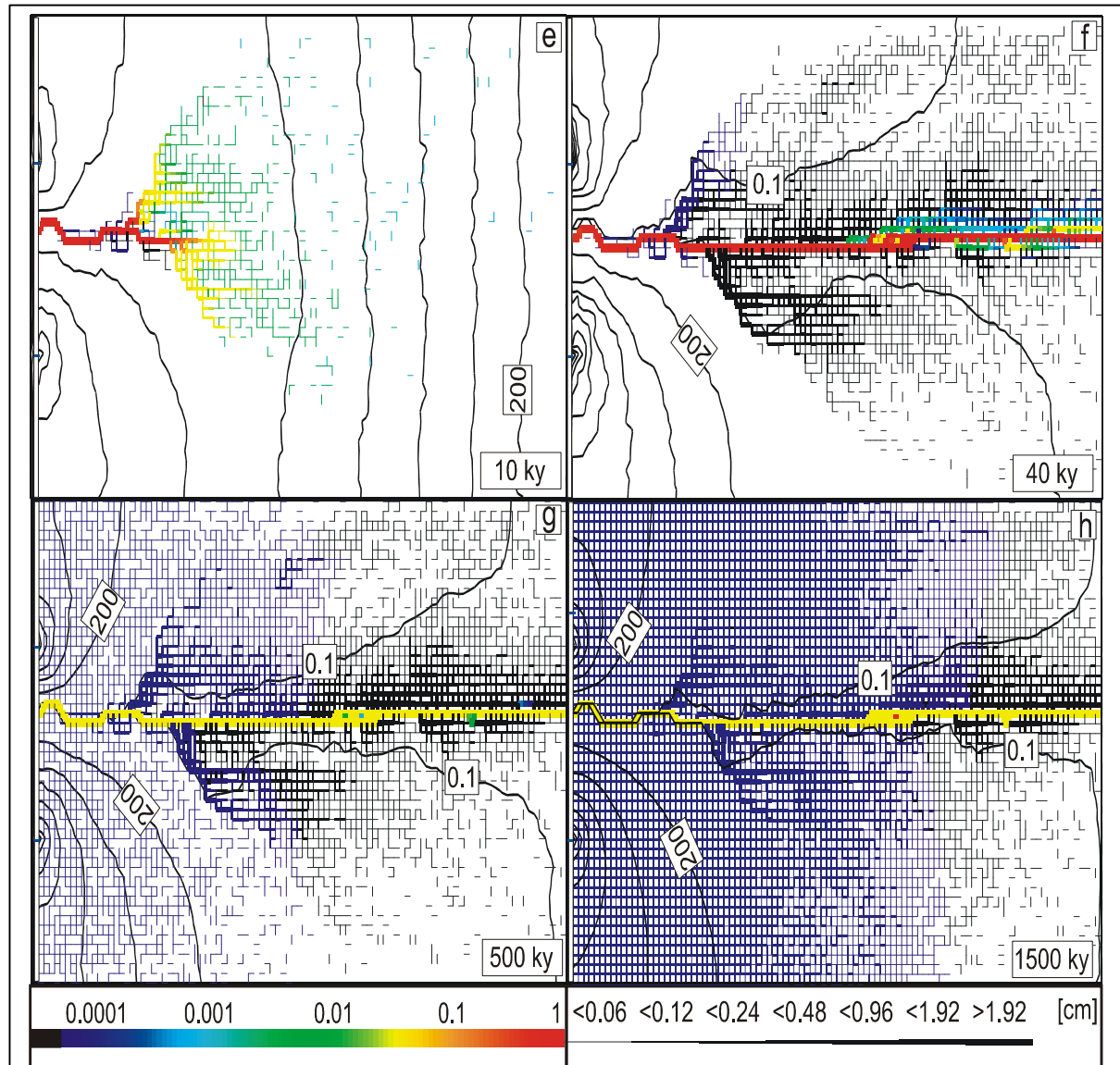


Fig. 4.7 e-h. Evolution of the fracture aperture widths and the dissolution rates for a scenario with the following chemical boundary conditions:

$P_{CO_2}^A = 0.05 \text{ atm}, P_{CO_2}^B = 0.01 \text{ atm}, f = 0.995;$

The bar code represents the fracture aperture widths in centimetres. All fractures with aperture widths smaller than 0.06 cm are omitted from the figures. The thick black lines represent the isolines of the pressure head distribution given in distances of 200 cm. The color code designates the dissolution rates in a logarithmic scale. The maximal dissolution rate F_{max} ($1.39 \cdot 10^{-13} \text{ mol} \cdot \text{cm}^{-2} \cdot \text{s}^{-1}$) is depicted by the red color. Dark blue means $0.0001 \cdot F_{max}$. Black stands for dissolution rates smaller than $10^{-5} \cdot F_{max}$. Note that the dissolution rates of the omitted fractures are not displayed.

Fig. 4.7e depicts the situation at 10000 years. It is similar to the one discussed already for the pure MC case – Fig. 4.4e. A channel develops in the zone of mixing and the dissolution rates are maximal there. But there is one difference, which plays an important role in the later

phases of the evolution. The concentration of the inflowing solution is close to saturation with respect to calcite ($0.995 \cdot c_{eq}$). As a consequence, the dissolution rates along the fractures close to the entry zone of the domain are small, but not zero. This means that all fractures, not belonging to the mixing zone are widened very slowly and linear in time. Actually, the figure is misleading in this case (Fig. 4.7a). It was already discussed that only fractures with aperture widths, considerably changed with respect to the initial ones, are displayed in the figure. The dissolution rates along the fractures belonging to the mixing zone are four orders of magnitude higher than the ones along the entry fractures. Therefore the fractures belonging to the entry zone are widened much slower than the ones belonging to the mixing zone, and are omitted from the figure. But as already discussed the dissolution rates along them are not zero and they would appear blue on the picture in contrast to the pure MC case, where all fractures outside the central channel are black (including the omitted from the figure entry ones) (Fig. 4.4 e). It further should be stressed, that the dissolution rates everywhere in these fractures are even and independent on the location (see eq. 1.15). Due to the high input concentration, saturation lengths are much longer than the dimension of the aquifer.

The situation after 40000 years is still similar to the one of the pure MC case (see Fig. 4.7f and Fig. 4.4f). The influence of the slow widening of the entry fractures is still not visible in the figure. The mixing zone is still the only area with considerable changes in the aperture widths of the fractures. The pattern of this zone is similar to the pure MC scenario (see Fig. 4.7f and Fig. 4.4f). The entry fractures are still not enough widened to be displayed on the picture. But after 500 000 years (Fig. 4.7g) one can clearly see the differences with the pure MC scenario (see Fig. 4.4.g). There is a system of fractures, which extends from the input downstream towards the output. The blue color depicts the extremely low dissolution rates along these fractures. As already discussed they widen slowly and linearly in time. The pressure head distribution is similar to the one of the pure MC case (see Fig. 4.4g). This means that the widening of the entry fractures cannot change the evolution of the central channel. But they change considerably the permeability of the aquifer. After 1.5 millions of years these fractures continue to penetrate deeper in the direction of the exit (see Fig. 4.7h). At the same time the central conduit continues to grow. Therefore, the distribution of the pressure head remains practically unaffected.

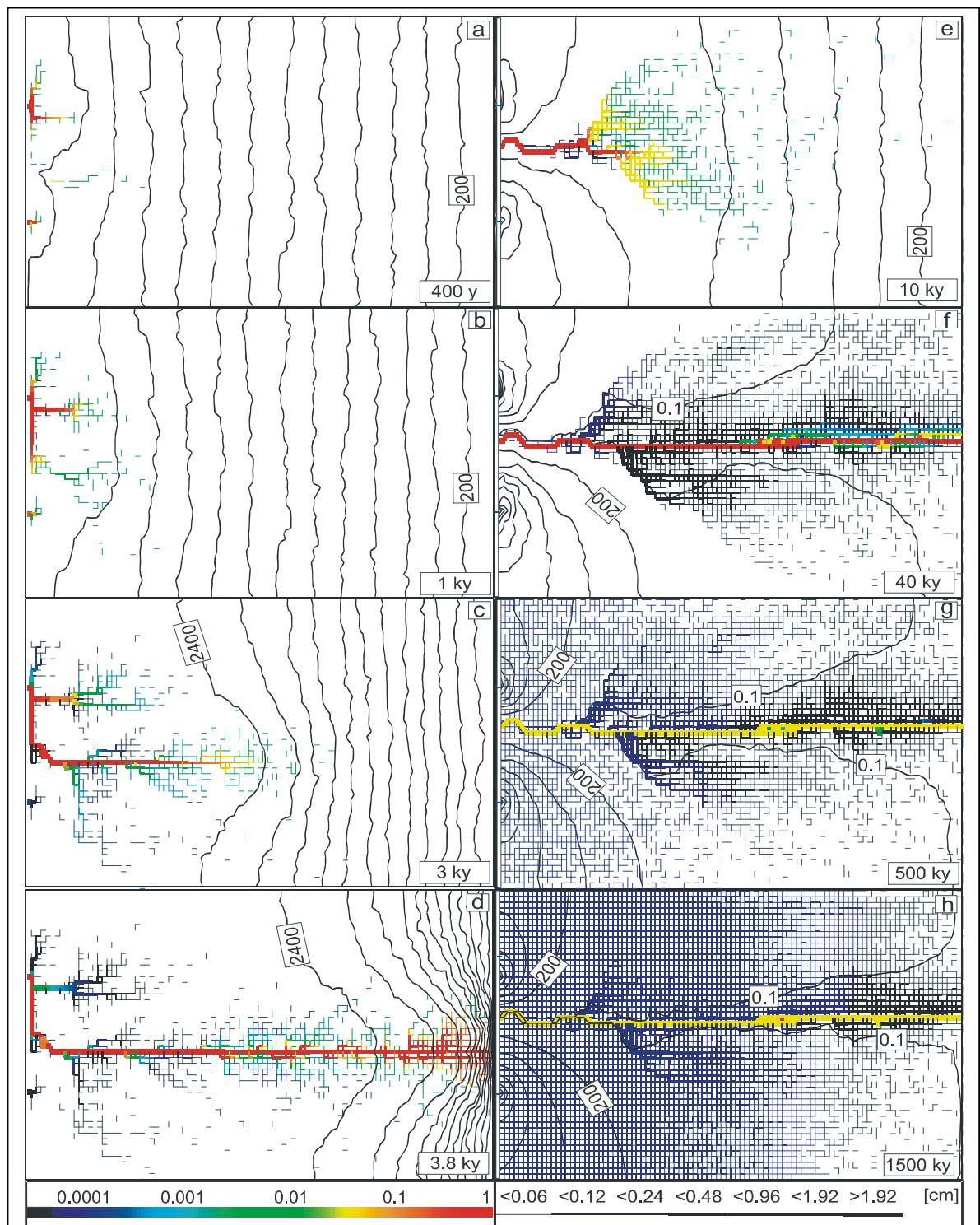
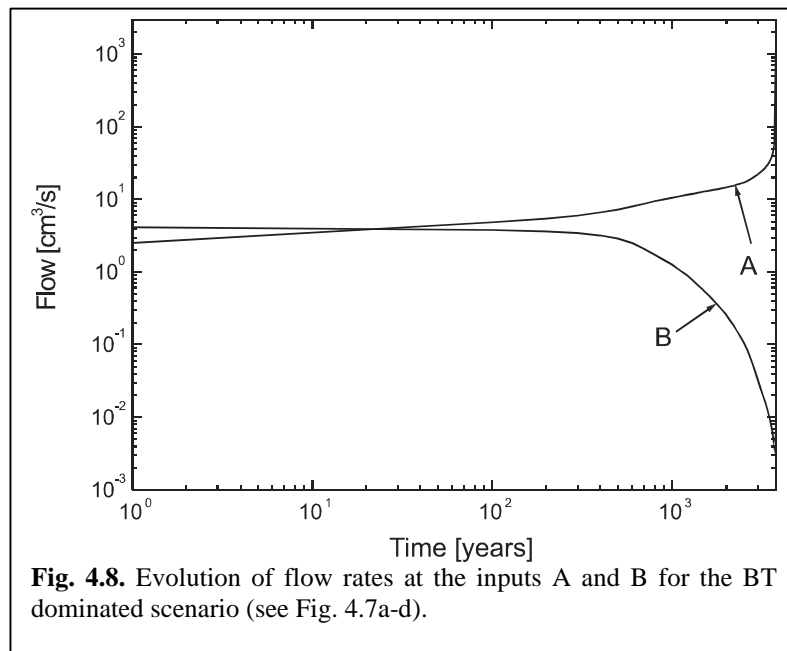


Fig. 4.7. Evolution of the fracture aperture widths and the dissolution rates for the scenarios with the following chemical parameters: $P_{co_2^A}=0.05 \text{ atm}$, $P_{co_2^B}=0.01 \text{ atm}$, $f=0.75$ (a-d), and $P_{co_2^A}=0.05 \text{ atm}$, $P_{co_2^B}=0.01 \text{ atm}$, $f=0.995$ (e-h);

The bar code represents the fracture aperture widths in centimetres. All fractures with aperture widths smaller than 0.06 cm are omitted from the figures. The thick black lines represent the isolines of the pressure head distribution given in distances of 200 cm. The color code designates the dissolution rates in a logarithmic scale. The maximal dissolution rate F_{max} ($2.4 \cdot 10^{-12} \text{ mol} \cdot \text{cm}^{-2} \cdot \text{s}^{-1}$ – subfigures a-d; $1.39 \cdot 10^{-13} \text{ mol} \cdot \text{cm}^{-2} \cdot \text{s}^{-1}$ – subfigures e-h) is depicted by the red color. Dark blue means $0.0001 \cdot F_{max}$. Black stands for dissolution rates smaller than $10^{-5} \cdot F_{max}$. Note that the dissolution rates of the omitted fractures are not displayed.

The results presented so far illustrate the importance of MC for the evolution of a karst aquifer. MC has a significant impact even for the cases with low calcium concentration of the inflowing solutions. Therefore our next goal is to find out whether MC is active during the entire evolution, or only in the initial phases.



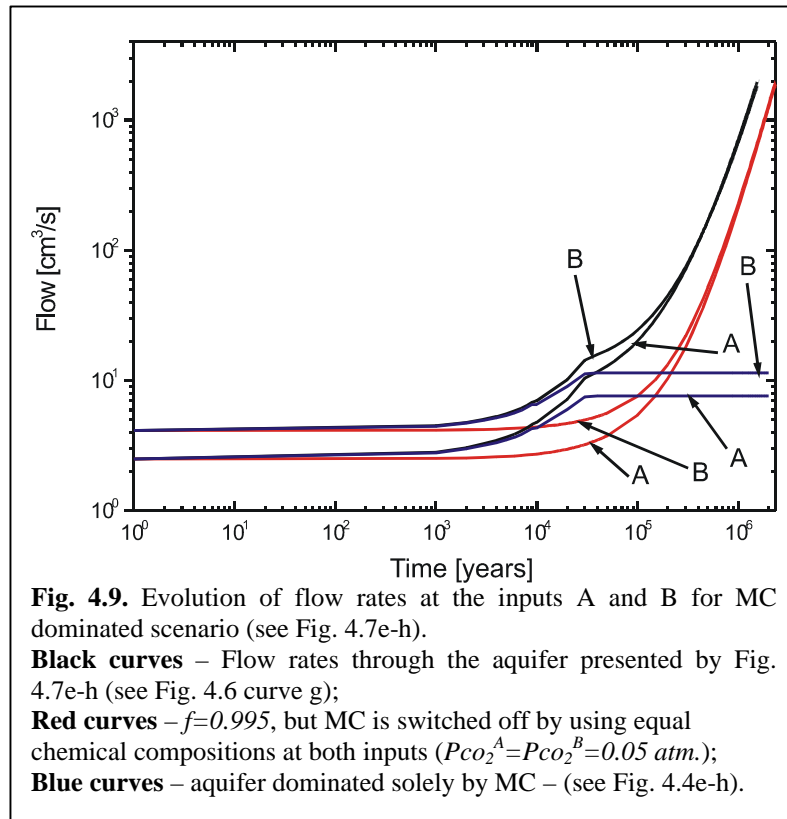
We start with the scenario with $f=0.75$. Fig. 4.8 depicts the flow rates through the upper and the lower entry points. The flow through the upper one is increasing steadily until breakthrough. The flow through the lower one is continuously decreasing. The reason for this is the head redistribution caused by the deeper penetration of the channel starting at the upper

inflow point. The flow rates through the upper and the lower entrances have similar magnitude only during the first 1000 years. Later the inflow through the lower input becomes negligibly small and MC is switched off. From this moment on the evolution of the aquifer is governed solely by the BT behavior.

To illustrate the influence of MC, Fig. 4.9 depicts an interesting comparison between the evolutions of the flow rates through the entry points for the following cases:

- a) The black lines depict the evolution for the aquifer with active MC and input concentration 0.995 of the equilibrium concentration with respect to calcite;
- b) The blue lines depict the evolution of the flow rates for the pure MC controlled aquifer;
- c) The red lines depict the evolution of the inflow for the case of an aquifer with $c_{in}=0.995 \cdot c_{eq}$, but $P_{CO_2}^A=P_{CO_2}^B=0.05$ atm. MC is deactivated in this scenario.

In contrast to the behavior for the case with $f=0.75$ (see Fig. 4.8), all flow rates increase with values of similar magnitude. Therefore MC is maintained over all times (of course only for the cases where it is active initially). We start with the curves depicting the evolution of cases with active MC (the black lines and the blue lines). The initial stage of the evolution is similar for both scenarios. Due to the widening of the network along the mixing zone, the flow



is increasing steeply. After the moment when the widened channel has reached the base level the flow through the net is limited for the case of pure MC, because the fractures in the area of the entrances are unaffected. For the other case the curves show a continuous slow further increase. The reason for this is the small even widening along the net of narrow fractures.

The red lines depict the scenario with disabled MC and $f=0.995$. Because of the

deactivated MC, there is no channel evolving in the mixing area. Therefore the fast increase of the flow rates is missing. The dissolution rates along the fractures are constant in space and linear in time. Consequently the flow rates through them increase by the time cubed (t^3).

4.2.4 Discussion

The evolution of a simple karst aquifer under different chemical boundary conditions was presented. Two basic patterns of flow evolution have been found. Fig. 4.6 depicts them. Curve (“a”) and the cyan curves (“b-d”) show typical BT behavior. The values of f are as follows:

- curve a – $f=0.75$, MC is not active;
- curve b – $f=0.75$, MC is active;
- curve c – $f=0.9$, MC is active;
- curve d – $f=0.96$, MC is active;

BT is dominating when the inflow solutions are highly aggressive, or when the inflowing solutions have the same chemical compositions. The changes of the dissolution rates in the mixing areas are not significant for these scenarios. The BT behavior is characterized by the slow increase of the flow rates in the initial stages of the evolution and the sudden increase

with several orders of magnitude at the breakthrough time. The evolution of the model aquifer dominated by BT is illustrated by Fig. 4.4 a-d and 4.7 a-d.

The green curves (“e-g”), and curve (“h”) depict the evolution of the flow rates for the scenarios dominated by MC. The values of f are as follows:

- curve e – $f=0.99$, MC is active;
- curve f – $f=0.9925$, MC is active;
- curve g – $f=0.995$, MC is active;
- curve h – $f=1$, MC is active.

We have already discussed that for the values of $c_{in} \geq 0.99 \cdot c_{eq}$ the feedback mechanism is switched off. This is depicted by the curves e-g. They exhibit a steady increase of the flow rates until the moment when the widening channel along the mixing zone reaches the output of the domain. After this moment, the flow rates are limited by the aperture widths of the entry fractures. As already discussed, they are widening evenly and linearly in time.

The evolution of curve (“h”) is different. This is the pure MC case. The inflowing solution is not aggressive and there is no change of the fractures belonging to the entry area. The consequence is the increase of the flow rates only until the moment when the central channel has reached base level. The flow rates remain constant afterwards.

Fig. 4.10 a-h depicts the differences in the hydrological properties of the aquifers evolved under BT or MC conditions. The lettering of the figure corresponds to the lettering of the curves from Fig. 4.6.

Fig. 4.10a depicts a typical BT dominated aquifer. MC was switched off for this simulation. There are considerably widened channels, starting from the entry points and progressing to base level. A fringe of fractures surrounds these channels. The reason is the outflow of still aggressive solution from the channels to the surrounding network. At the same time there is almost no change in the areas remote from the widened conduits.

Fig. 4.10b depicts the final pattern of the aquifer, with $f=0.75$, but this time MC is active. As already discussed, its action creates areas with higher conductivity deep inside the aquifer. The growth of the channels is diverted to these areas. This is the reason for the differences with respect to the previous scenario. But the basic behavior is similar.

Fig. 4.10c depicts the consequences of the increase of the input concentration to $0.9 c_{eq}$. In this case the influence of the MC is bigger. The zones of increased conductivities are wider and complicated patterns are created. For the scenario with even higher value of $f = 0.96$, this effect is further increased (see Fig. 4.10d). But the situation at even higher saturation ratios is entirely different.

The dissolution rates along the mixing zones are higher than the ones in the rest of the network. This creates a central channel, which is not directly connected to the entrance points (see Fig. 4.10 e). The time scales for the evolution of these type of aquifers is much longer. The reason is the high hydraulic resistances near the entry points. These fractures open much slower than the ones belonging to the central conduit. The rates are even and linear in time.

A similar patterns are depicted in Fig. 4.10f and 4.10g. The difference is in the time scales and in the rates of widening of the fractures around the entry areas. But the main pattern is the one typical for the MC governed evolution. It is a central channel, and relatively evenly widened network.

Fig. 4.10 h, depicts the final pattern for the pure MC case. The difference with the previous two scenarios is the absence of the evenly widened zone. The reason is the saturated solution coming from the entrances.

The values of the F_{max} are as follows:

- a) $1 \cdot 10^{-11} \text{ mol} \cdot \text{cm}^{-2} \cdot \text{s}^{-1}$;
- b) $4 \cdot 10^{-12} \text{ mol} \cdot \text{cm}^{-2} \cdot \text{s}^{-1}$;
- c) $1.02 \cdot 10^{-13} \text{ mol} \cdot \text{cm}^{-2} \cdot \text{s}^{-1}$;
- d) $1.89 \cdot 10^{-13} \text{ mol} \cdot \text{cm}^{-2} \cdot \text{s}^{-1}$;
- e) $7.41 \cdot 10^{-14} \text{ mol} \cdot \text{cm}^{-2} \cdot \text{s}^{-1}$;
- f) $5.33 \cdot 10^{-14} \text{ mol} \cdot \text{cm}^{-2} \cdot \text{s}^{-1}$;
- g) $1.39 \cdot 10^{-13} \text{ mol} \cdot \text{cm}^{-2} \cdot \text{s}^{-1}$;
- h) $1.23 \cdot 10^{-14} \text{ mol} \cdot \text{cm}^{-2} \cdot \text{s}^{-1}$.

The differences in the patterns of the fracture aperture widths for the scenarios depicted by Fig. 4.10 a-h, show the complicated interplay between the BT and MC. Note that differences are a consequence only of the variation of the chemical boundary conditions. The hydrological parameters are the same in any of the studied cases.

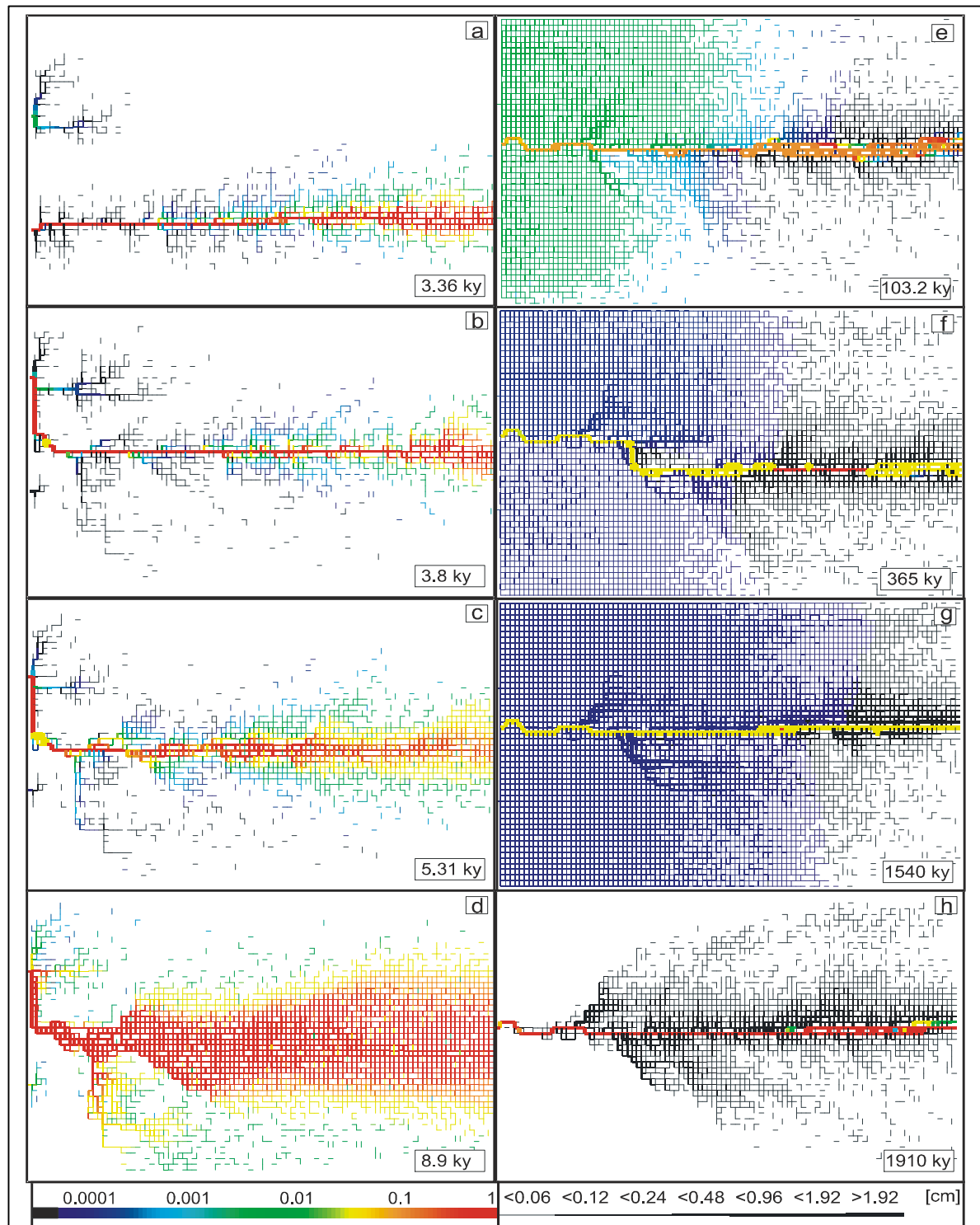


Fig. 4.10. Fracture aperture widths and dissolution rates at the termination of the calculations. The letters in the figures relate to the corresponding curves in Fig. 4.6.

The bar code represents the fracture aperture widths in centimetres. All fractures with aperture widths smaller than 0.06 cm are omitted from the figures. The thick black lines represent the isolines of the pressure head distribution given in distances of 200 cm. The color code designates the dissolution rates in a logarithmic scale. The maximal dissolution rate F_{max} is depicted by the red color. Dark blue means $0.0001 \cdot F_{max}$. Black stands for dissolution rates smaller than $10^{-5} \cdot F_{max}$. Note that the dissolution rates of the omitted fractures are not displayed.

Aquifers a-d exhibit a BT controlled evolution.

Aquifers e-h – MC controlled behaviour.

4.2.5. Conclusion

We have studied the reaction of a simple karst aquifer to variations in the chemical boundary conditions. Two modes of karstification were discussed.

The BT dominated mode is active, when the saturation of the inflowing water with respect to calcite is relatively low and when the chemical compositions of the inflowing waters are equal. The widened channels connecting the entry points and base level characterizes the final pattern of the aquifer. Because of the outflow of aggressive solutions a fringe of widened fractures is created around these channels.

The MC dominated mode exhibits a central channel, which is not directly connected to the entry points. This mode is active in the cases of solutions highly saturated with respect to calcite, and different equilibrium concentrations. The central channel depicts the zone of mixing of the inflowing solutions. In contrast to the BT dominated scenarios, the flow is directed from the network into the central conduit. If the concentration of the entering water is not equal to the equilibrium concentration, a zone of evenly widened fractures is created along the aquifer. The time scale for the evolution in the cases dominated by MC is much longer than for the one dominated by BT.

We have studied the combined action of both modes, changing systematically the chemical initial and boundary conditions. The initial hydrological properties of the modeled karst aquifer were the same for all scenarios. Even so, the final patterns of the modeled aquifers are considerably different.

5. Conclusion

The goal of the presented work is to study the effect of various hydrological and chemical boundary conditions on karst aquifers. We create two-dimensional numerical models of confined aquifers and study their evolution.

Our first topic is the influence of exchange flow. We model a simple geological setting. It is a fractured limestone terrain, with a river supporting constant head at the inflow boundary. The outflow side is open. There is a fracture considerably wider in comparison to the primary fissures, conduit connecting the river with the base level. We discuss the evolution of this aquifer under man made (high hydraulic gradients, and short pathways) and natural boundary conditions. Our goal is to study the effect of the exchange flow solely. Therefore the chemical composition of the inflowing water is constant along the entire entry boundary.

We use a 2D rectangular fracture network to model these geological settings. Two different realizations of the initial aperture widths of the fissures are presented:

- a) Uniform network (all fissures have equal initial aperture widths), which is easier to interpret;
- b) Statistical network (the initial aperture widths of the fissures are log-normally distributed), which is closer to the natural environment.

We vary the value of the hydraulic head at the inflow boundary, and the initial aperture widths of the fissures for the studied scenarios. By this way we are able to study the effect of varying exchange flow on the evolution of the aquifer.

We start with unnaturally high hydraulic head typical for man-made environments, and vary the values of the initial aperture widths of the fissures. The results show that for negligibly small exchange flow (negligibly small initial aperture widths of the fissures) the initially wider central conduit behaves like an isolated channel. With the increase of the effect of the exchange flow, the evolution of the central conduit is accelerated. For relatively small initial aperture widths of the fissures, the change of the breakthrough time is not considerable. But with further increase of exchange flow, the time for the evolution is reduced by almost an order of magnitude. This behavior is observed also for natural environments (low hydraulic gradients).

The evolution of the fissure network also depends on the amount of the exchange water. Entry and exit type fans develop for excessive values of exchange. The permeability of the fine network is considerably increased. On the other hand, if the timescales for the evolution of

both hydraulic systems (fine fissure network and central wider fracture) are significantly different, then the changes in the continuum are negligible.

In order to give a detailed explanation of the obtained results we discuss the influence of exchange flow on the evolution of a simple three fractures system. Similar dependence on the evolution is observed. We find that the influence on the evolution is maximal, when the position of the exchange node is close to the midpoint of the fracture.

We also present an analytical approximation of the breakthrough time for large values of exchange flow.

Our next step is to study the evolution of karst aquifers close to large hydraulic structures, such as dam sites. Our goal is to draw the attention on the influence of the karstification processes on the safety of these structures. We study the evolution of several model dams. We create a numerical model of karst aquifer. Similar to the previous study it is based on two-dimensional fracture network. We use statistical and uniform distribution for the initial aperture widths of the fractures. By this way we are able to take into account the influence of exchange flow, and to extend the results obtained by single fracture models or by models based on percolation networks.

The results show a large zone of increased conductivity below the dam structure. The channels comprising this area are considerably widened with respect to their initial aperture widths. The flow through them is turbulent. The dissolution rates along them are even and close to the maximal in the net. The consequence is fast enlargement of the widened zone, and an increase of the leakage from the dam. On the other hand the mechanical stability of the structure is endangered.

We perform sensitivity analyses in order to study the evolution of the aquifer with respect to the basic geometrical, hydrological, and chemical parameters of the dam sites. These are the hydraulic head at the upstream embankment, the initial aperture widths of the fractures comprising the network, the length of the grouting curtain, the Ca concentration of the inflowing water, and the equilibrium concentration. The obtained results are similar to the ones found by the one-dimensional and percolation network models - $T_B \mu a_0^{-3}$, $T_B \mu H^{-4/3}$, $T_B \mu c_{eq}^{-1.4}$. The influence of the grouting depth is of crucial importance, because T_b increases steeply with the increase of the length of the grouting curtain. We discuss the effect of scaling of the values of the hydraulic head, the sealing apron length and the length of the grout with a common

factor. The results show that small dam structures encounter breakthrough earlier than geometrically similar, but larger dams.

We also present the evolution of a karst aquifer below a dam site, for the case when the soluble rock is gypsum. The results are similar to those for limestone. The main difference is the considerably faster increase of the leakage rates after the breakthrough event. Also the widening below the dam is concentrated to a single pathway.

The karstification below dam sites is studied for several, more complicated geological scenarios. We present also a model of the failure of an earth dam in Spain. The results show that our models can be used to study, more complicated and closer to the reality, scenarios. In this case a detailed knowledge about the geological settings of the modeled aquifers is required.

Our next task is to study the effect of the hydro-chemical boundary conditions on the evolution of karst aquifers. We create a two-dimensional numerical model of the following geological settings. Confined aquifer, consisting of a limestone bed with two inflow points at constant head and open flow along the entire base level. The vegetation around the input points is different, and this is the reason for the differences in the chemical composition of the inflowing water. All scenarios have equal hydrological boundary conditions. We vary only the chemical parameters of the inflowing water. The first scenario has equal chemical composition at both entry points. By this way the effect of mixing corrosion is switched off. The aquifer exhibits a typical breakthrough governed evolution (pathways growing from the entry points to the exits, active feedback mechanism leading to breakthrough event).

Then we change the chemical composition of the water at one of the entrances. In this way, we activate the effect of mixing corrosion. Our goal is to study the influence of this effect and its interplay with the breakthrough type evolution. Therefore, our next scenario has saturated with respect to calcite solution on both entrances, and different equilibrium concentrations. The inflowing solutions become aggressive only in the areas where they mix. By this way the effect of the mixing corrosion solely, is studied. The observed evolution is characterized by a widened pathway starting at the mixing zone and growing towards the base level. There is no widened zone connecting the mixing area with the entrances. There is no breakthrough even at the moment when the widened channel reaches the base level. The outflow from the domain remains constant afterwards.

The next set of scenarios is performed to study the interplay between these two extreme modes of karstification. The results show that for calcium concentrations of the inflowing solutions

below $0.96x_{eq}$, the aquifer exhibits breakthrough type evolution. Mixing corrosion influences the direction of the evolving channels, and creates zones of higher permeability in the regions where it is active.

For calcium concentration of the inflowing solutions higher than $0.99x_{eq}$ the evolution is governed mainly by mixing corrosion. The feedback mechanism is switched off, and the main widening is along the channel evolving in the mixing zone. The inflowing solution is not completely saturated with respect to calcite, and this is the reason for continuous, even in space, slow widening of the whole network. By this way the permeability of the aquifer is constantly increased in time.

The time scale for the breakthrough type evolution is in the range of several thousands to several hundred thousand years. In contrast, the time scale for mixing corrosion type evolution is in the range of several millions of years.

We have performed several simulations on the effect of mixing corrosion on aquifers below large hydraulic structures. Because of the long time scales this effect is not crucial for the evolution of these aquifers.

The goal of this work was to extend further the results of the single conduit and percolation network models. Using a refined modeling technique and statistical distribution of the initial aperture widths of all fractures comprising the modeling 2D networks, we were able to perform a detailed study on the effect of exchange flow and mixing corrosion on the evolution of karst aquifers.

We were also able to get a better view on the effect of the man-made structures on the karstification.

Our results also have practical importance, because they give an idea about the possible pathways of pollutants penetration into the karst aquifers.

We also discuss the parameters, which have high impact on the hydrological safety of man-made structures, such as dam sites.

Our next step, for the future, will be to extend our models to three-dimensional ones and to study the evolution of larger scale and geologically complex karst aquifers.

Bibliography

- Bauer, S., S. Birk, R. Liedl, and M. Sauter (1999). Solutionally enhanced leakage rates of dams in karst regions. *Karst Waters Institute Special publication* 5:158-162.
- Bauer, S., Liedl R., and Sauter M., 2000, Modelling of karst development considering conduit matrix exchange flow. In: *Calibration and reliability in ground water modelling* (Stauffer F., Kinzelbach W., Kovar K., and Hoehn E. Eds.) IAHS publication 265, 10-15
- Bauer, S, 2002, Simulation of the genesis of karst aquifers in carbonate rocks, *Tuebinger geowissenschaftliche arbeiten (TGA)*, C62, 2002.
- Beek, W.J. & Mutzall, K.M.K., 1975. *Transport Phenomena*. Wiley, New York.
- Bear and Verruijt, 1987, *Modeling groundwater flow and pollution*, D. Reidel Publishing company, Dordrecht, Holland.
- Bögli, A., 1964. Mischungskorrosion – ein Beitrag zum Verkarstungsproblem. *Erdkunde* 18:83-92.
- Bögli, A., 1980. *Karst hydrology and physical speleology*, Springer, Berlin, Heidelberg, New York.
- Buhmann, D., Dreybrodt W., 1985a. The kinetics of calcite dissolution and precipitation in geologically relevant situations of karst areas: 1. Open system. *Chem. Geol.*, 48, 189-211.
- Buhmann, D., Dreybrodt W., 1985b. The kinetics of calcite dissolution and precipitation in geologically relevant situations of karst areas: 2. Closed system. *Chem. Geol.*, 53, 109-124.
- Clemens, T., Hückinghaus, D., Sauter, M., Liedl, R., Teutsch, G., 1996. A combined continuum and discrete network reactive transport model for simulation of karst development. In *Calibration and reliability in groundwater modelling – proceedings of the ModelCARE 96 conference held at Golden, Colorado, September 1996*, IAHS Publ. no. 237, pp. 309-318.
- Clemens, T., Hückinghaus, D., Sauter, M., Liedl, R., Teutsch, G., 1997a. Modelling the genesis of karst aquifer systems using a coupled reactive network model. In: *Hard Rock Geosciences*. IAHS Publ., 241, Colorado: 3-10.
- Clemens, T., Hückinghaus, D., Sauter, M., Liedl, R., Teutsch, G., 1997b. Simulation of the evolution of maze caves. In *proceedings of the 12th International congress of speleology*, La Chaux-de-Fonds, Switzerland, Volume 2, pp65-68.
- Cvijic, J. *Geomorfologija I e II*, Beograd, Yugoslavia

- Dreybrodt W., 1981. Kinetics of dissolution of calcite and its applications to karstification. *Chemical Geology* 31:245-269.
- Dreybrodt W., 1988. Processes in karst systems - Physics, Chemistry and Geology. Springer Series in Physical Environments 4, Springer, Berlin, New York, 188p.
- Dreybrodt, W., 1990. The role of dissolution kinetics in the development of karstification in limestone: A model simulation of karst evolution. *Journal of Geology*, 98, 639-655.
- Dreybrodt, W., and Buhmann, D., 1991. A mass transfer model for dissolution and precipitation of calcite from solutions in turbulent motion. *Chem. Geol.*, 90, 107-122.
- Dreybrodt, W., 1992. Dynamics of karstification: A model applied to hydraulic structures in karst terranes. *Appl. Hydrogeol.*, 1, 20-32.
- Dreybrodt, W., 1996. Principles of early development of karst conduits under natural and man-made conditions revealed by mathematical analysis of numerical models: *Water Resources Research*, 32, 2923-2935.
- Dreybrodt, W., Lauckner, J., Zaihua, L., Svensson, U., Buhmann, D., 1996. The kinetics of the reaction $\text{CO}_2 + \text{H}_2\text{O} \rightarrow \text{H}^+ + \text{HCO}_3^-$ as one of the rate limiting steps for the dissolution of calcite in the system $\text{H}_2\text{O} - \text{CO}_2 - \text{CaCO}_3$. *Geochim. Cosmochim. Acta*, 60, 3375-3381.
- Dreybrodt, W., and Eisenlohr, L., 2000, Limestone dissolution rates in karst environments: In: Klimchouk, A., Ford, D.C., Palmer, A.N., and Dreybrodt, W., (Editors), *Speleogenesis: Evolution of karst aquifers*. *Nat. Speleol. Soc., USA*, 136-148.
- Dreybrodt, W., and Gabrovšek F., 2000, Dynamics of the evolution of a single karst conduit: In: Klimchouk, A., Ford, D.C., Palmer, A.N., and Dreybrodt, W., (Editors), *Speleogenesis: Evolution of karst aquifers*. *Nat. Speleol. Soc., USA*, 184-193.
- Dreybrodt, W., and Siemers, J., 2000. Cave evolution on two-dimensional networks of primary fractures in limestone: In: Klimchouk, A., Ford, D.C., Palmer, A.N., and Dreybrodt, W., (Editors), *Speleogenesis: Evolution of karst aquifers*. *Nat. Speleol. Soc., USA*, 201-211.
- Dreybrodt, W., Romanov, D., and Gabrovšek F., 2001. Karstification below dam sites: a model of increasing leakage. In: Beck, B.F., Herring, J. G., (Eds.). *Geotechnical and environmental applications of karst geology and hydrology: Proceedings of the 8th Multidisciplinary Conference on Sinkholes and the Engineering and Environmental Impacts of Karsts*, Louisville, Kentucky, Balkema, p. 131-137.

- Eisenlohr L., Meteva, K., Gabrovšek, F., Dreybrodt, W., 1999. The inhibiting action of intrinsic impurities in natural calcium carbonate minerals to their dissolution kinetics in aqueous H₂O-CO₂ solutions. *Geochimica et Cosmochimica Acta*, 63, 989-1002.
- Ford., D. and R. Ewers. The developmnet of limestone caves in the dimesnions of length and depth. *Can. J. Earth. Sci.*, 15:1783-1798, 1978.
- Ford, D.C. Williams, P.W., 1989. *Karst geomorphology and hydrology*. Unwin Hyman, London
- Gabrovšek, F., 2000. *Evolution of early karst aquifers: From simple principles to complex models: Založba ZRC, Ljubljana, Slovenia, 150p.*
- Gabrovsek, F. and Dreybrodt, W., 2000a. The role of mixing corrosion in calcite aggressive H₂O-CO₂-CaCO₃ solutions in the early evolution of karst aquifers. *Water Resources Research*, 36: 1179-1188.
- Gabrovsek, F. and Dreybrodt, W., 2000b. A model of early evolution of karst conduits affected by subterranean CO₂ sources. *Environmental Geology*, 39:531-543, 2000.
- Gabrovsek, F. and Dreybrodt, W., 2001. A model of the early evolution of karst aquifers in limestone in the dimensions of length and depth. *Journal of Hydrology*, 240: 206-224.
- Groves, C., Howard, A. Early development of karst systems 1. preferential path enlargement under laminar flow. *Water Resources Research*, 30:2837-2846, 1994.
- Gale, J. E., 1987. Comparison of couplet fracture deformation and fluid flow models with direct measurement of fracture pore structure and stress-flow properties. *Proceedings of the 28th U. S. Symposium of Rock Mechanics, Tucson, Arizona, 1987*, p. 1213.
- Gutierrez, F., G. Desir, M. Gutierrez., 2002, Causes of the catastrophic failure of an earth dam built on gypsiferous alluvium and dispersive clays (Altorricón, Huesca Province, NE Spain), 43, 7, 842-851, *Environmental Geology*
- Hamblin, W., 1989, *Earth's dynamic system*, Macmillan Publishing Company, New York.
- Howard, A.D., Groves, C.G., 1995. Early development of karst systems 2. Turbulent flow. *Water Resources Research*, 31, 19-26.
- Incropera, F. P., Dewitt, D. P., 1996. *Fundamentals of heat and mass transfer*: John Wiley & Sons Inc., New York, 889 p.
- James, A.N., 1992. *Soluble Materials in Civil Engineering: Ellis Horwood Series in Civil Engineering*: Ellis Horwood, Chichester, England, 434 p.

- James, A., N., Kirkpatrick, I., M., 1980, Design of foundations of dams containing soluble rock and soils. *Q. J. eng. Geol. London*. 1980, 13, 189-198.
- Jeschke, A.A., Vosbeck, K., and Dreybrodt, W., 2001. Surface controlled dissolution rates in aqueous solutions exhibit nonlinear dissolution kinetics: *Geochimica et Cosmochimica Acta*, 65, 13-20.
- Kaufmann, G., 2003. Numerical models for mixing corrosion in natural and artificial karst environments. Submitted to *Water Resources Research*.
- Kaufmann, G., Braun, J., 1999. Karst aquifer evolution in fractured rocks. *Water Resources Research*, 35: 3223-3238.
- Kaufmann, G., Braun, J., 2000. Karst aquifer evolution in fractured, porous rocks. *Water Resources Research*, 36: 1381-1391.
- Lauritzen, O. N. Modeling the evolution of channel networks in carbonate rocks. In J. Hudson, editor, *ISRM Symposium: Eurock'92*, pages 57-62. Thomas Telford, 1992.
- Laptev, F. F., 1939. Aggressive action of water on carbonate rocks, gypsum, and concrete. *GONTI, Moscow-Leningrad*, 120 p (in Russian)
- Lee, C., Farmer, I., 1993. *Fluid flow in Discontinuous Rocks*. Chapman & Hall, London.
- Liu Z., Dreybrodt W., 1997. Dissolution kinetics of calcium carbonate minerals in H₂O-CO₂ solutions in turbulent flow: The role of the diffusion boundary layer and the slow reaction $\text{H}_2\text{O} + \text{CO}_2 \rightleftharpoons \text{H}^+ + \text{HCO}_3^-$. *Geochimica et cosmochimica acta*, 61, 2879-2889.
- Lowe, D., 2000, Development of Speleogenetic ideas in the 20th century: The early modern approach. In Klimchouk, A., Ford, D.C., Palmer, A.N., W. Dreybrodt (Editors), *Speleogenesis: Evolution of karst aquifers*. Nat. Speleol. Soc., USA.
- Milanovic, P.T., 1981. *Karst hydrogeology*. Water Resources Publication, Littleton, USA.
- Milanovic, P. T., 2000. *Geological Engineering in Karst*. Zebra Publishing, Ltd, Belgrade, Yugoslavia.
- Palmer, A.N., 1988. Solutional enlargement of openings in the vicinity of hydraulic structures in karst regions: In: 2nd Conference on Environmental Problems in Karst Terranes and Their Solutions. Assoc. of Groundwater Scientists and Engineers Proceedings, USA, 3-15.
- Palmer, A. N., 1991. The origin and morphology of limestone caves. *Geol. Soc. of America Bull.*, 103, 1-21.

- Press, W.F., Teukolsky, S.A., Vetterling, W.T., Flannery, B.P., 1992. Numerical recipes in C: The art of scientific computing. Cambridge University Press.
- Rhoades., R. and M. Sinacori. The pattern of ground-water flow and solution. *Journal of Geology*, 49:785-794, 1941.
- Shaw, T. 2000. Views on cave formation before 1900. In Klimchouk, A., Ford, D.C., Palmer, A.N., W. Dreybrodt (Editors), *Speleogenesis: Evolution of karst aquifers*. Nat. Speleol. Soc.,USA.
- Siemers, J. Simulation von Karst-Aquiferen. PhD Thesis, Universitaet Bremen, 1998.
- Siemers, J., Dreybrodt, W., 1998. Early development of karst aquifers on percolation networks of fractures in limestone. *Water Resources Research*, 34, 409-419.
- Steward, D.E., Leyk, Z., 1994. Meschach: The matrix computation in C: Proceedings of the Centre For Mathematics And Its Applications, 32, The Australian National University, Canberra, Australia.
- Svensson, U., Dreybrodt, W., 1992. Dissolution kinetics of natural calcite minerals in CO₂ - water systems approaching calcite equilibrium. *Chem. Geol*, 100, 129-145.
- Swinnerton, A. C., 1932. Origin of limestone caverns. *Bull. Geol. Soc. America* 43:662-693.
- Thraillkill, J., 1968, Chemical and hydrogeological factors in the excavation of limestone caves. *Geol. Soc. Am. Bull* 79:19-46
- Uromeihy, A., 2000. The Kar Dam: An example of infrastructural development in a geologically active karstic region, *Journal of Asian Earth Sciences*, 18,25-31.
- White, W. B., 2000, Development of speleogenetic ideas in the 20th century: The modern period, 1957 to the present. In Klimchouk, A., Ford, D.C., Palmer, A.N., W. Dreybrodt (Editors), *Speleogenesis: Evolution of karst aquifers*. Nat. Speleol. Soc.,USA.

List of publications

1. Dreybrodt, W., Romanov, D., Gabrovsek, F. 2001, Karstification below dam sites: a model of increasing leakage from reservoirs. In *Geotechnical and Environmental Applications of Karst Hydrology*, Beck and Herring (editors), Swets and Zeitinger, Lisse, 2001.
2. Dreybrodt, W., Romanov, D. Gabrovsek, F. 2002, Karstification below dam sites: a model of increasing leakage from reservoirs. *Environmental Geology*, 42, 518-524, Springer Verlag, 2002.
3. Romanov, D., Dreybrodt, W. Gabrovsek, F., 2002, Interaction of fracture and conduit flow in the evolution of karst aquifers. In *Proceedings of the symposium Karst Frontiers: Florida and Related Environments*, Martin, J., Wicks, C., and Sasowsky, D., (editors), Karst Waters Institute, Charles Town, West Virginia, 2002.
4. Romanov, D., Gabrovsek, F., Dreybrodt, W., 2003, Dam sites in soluble rocks: a model of increasing leakage by dissolutional widening of fractures beneath a dam, *Engineering Geology*, in press.
5. Romanov, D. Gabrovsek, F., Dreybrodt, W., 2003, The impact of hydrochemical boundary conditions on the evolution of limestone karst aquifers. *Journal of Hydrology*, in press.

Presentations at scientific meetings:

1. The impact of hydrochemical boundary conditions on the evolution of karst aquifers in limestone terrains. Poster presentation at the symposium "Evolution of Karst: From Prekarst to Cessation", Postojna, Slovenia, 2002.
2. Interaction of fracture and conduit flow in the early evolution of karst aquifers. Poster presentation at the symposium "Evolution of Karst: From Prekarst to Cessation", Postojna, Slovenia, 2002.